# The
# Philosophical Magazine

## FIRST PUBLISHED IN 1798

## A Journal of Theoretical
## Experimental and Applied Physics

ALERE FLAMMAM

# THE PHILOSOPHICAL MAGAZINE

AUTHORS wishing to submit papers for publication in the Journal should send manuscripts directly to the Publishers.

Manuscripts should be typed in *double* spacing on one side of quarto (8 × 10 in.) paper, and authors are urged to aim at absolute clarity of meaning and an attractive presentation of their texts. Each paper should be preceded by a brief abstract in a form suitable for reproduction in abstracting journals.

References should be listed at the end in alphabetical order of authors and should be cited in the text in terms of author's name and date. Diagrams should normally be in Indian ink on white card, with lettering in soft pencil, the captions being typed on a separate sheet.

A leaflet giving detailed instructions to authors on the preparation of papers is available on request from the Publishers.

Authors are entitled to receive 25 offprints of a paper in the Journal free of charge, and additional offprints can be obtained from the Publishers.

The *Philosophical Magazine* and its companion journal, *Advances in Physics*, will accept papers for publication in experimental and theoretical physics. The *Philosophical Magazine* publishes contributions describing new results, letters to the editor and book reviews. *Advances in Physics* publishes articles surveying the present state of knowledge in any branch of the science in which recent progress has been made. The editors welcome contributions from overseas as well as from the United Kingdom, and papers may be published in English, French and German.

# Theory of Linear Facet Growth During Thermal Etching†

By W. W. Mullins

Department of Metallurgy, Carnegie Institute of Technology,
Pittsburgh, Pa., U.S.A.‡

### Abstract

Under certain conditions, a planar metal surface will develop linear facets, or planar strips inclined to the original surface and meeting it along sharp cusp lines (e.g. Ag heated in air). A discussion is given, in terms of the Wulff plot, of the energetic conditions under which linear facts form. A theory is then developed, subject to certain simplifying assumptions, of the progressive widening of the facets under the separate action of evaporation-condensation and of surface diffusion. Order of magnitude calculations are also given for the case of volume diffusion. Facet profiles and their characteristic time laws of growth are calculated. In the case of surface diffusion, the theoretical results depend upon a parameter equal to the ratio of the surface diffusion coefficient on the facet plane to that on the general complex surface. Comparison with experiment should permit determination of this parameter as well as other interesting information.

## § 1. Introduction

The spontaneous alteration of the topography of a planar solid surface at elevated temperatures is generally termed thermal etching. The thermal etching may be produced by crystal imperfections terminating on the surface; two examples of this case are (1) thermally etched dislocation pits (Hendrickson and Machlin 1955) and (2) thermal grooving at grain boundaries (Mullins 1957, Mullins and Shewmon 1959). It may also occur independently of, and on portions of the surface removed from, the loci of terminating imperfections; two causes commonly postulated in this case are (1) the kinetics of atomic migration (Frank 1958, Hirth and Pound 1960) on a crystal surface which is experiencing an unbalanced exchange of material with its environment, and (2) the reduction in surface free energy (Herring 1951 b) accompanying the new orientations introduced during etching.

Thermal etching has been studied experimentally by several investigators, most notably in silver by Chalmers *et al.* (1948), by Moore (1958), and by Moreau and Benard (1959). These investigators find that a suitably oriented planar surface of silver when heated in air will develop facets which, initially at least, take the form of planar strips or linear facets (one of which appears in fig. 1 (*a*)) parallel to each other and inclined to the original surface, thereby forming a serrated topography. The

---

† Communicated by the Author.
‡ Temporary address: Faculté des Sciences, Universitéde Paris, Orsay, France.

surface reverts to a plane when heated in nitrogen indicating that the faceting depends on the presence of oxygen for its occurrence†. (Although bulk silver oxide is not stable under the reported annealing conditions, oxygen may still be appreciably adsorbed on the surfaces.) Moore (1958) found that the facet planes, which he terms simple surfaces, are always (100) or (111) planes, while the connecting strips, which he terms complex surfaces, have no simple crystallographic orientation‡ and are in fact curved as shown in fig. 1. He has observed that a given facet strip grows by lateral extension of its width (and length) as indicated in fig. 1 (*b*).

It is not definitely established whether the faceting studied in the preceding experiments is a kinetic phenomena to be attributed to movements of surface atoms on a crystal gaining or losing material to the vapour, or an equilibrium phenomena to be attributed to the tendency of the surface to reduce its free energy. Although Moore (1958) interpreted his earlier work in Ag on the surface energy hypothesis, experiments he and Hondros have performed more recently (Hondros and Moore 1960) have led them to reject this hypothesis as an explanation of the results. In any case, the present paper will be based on the surface energy point of view, that is, surface energy will be assumed to be the cause of a type of faceting and the theoretical consequences will be developed. The results should afford an improved basis from which the experiments may be interpreted.

Herring (1951 b) has given a precise discussion of the energetic conditions under which faceting will occur. He has also given a discussion (Herring 1952) of the growth on a wire of an energetically induced facet that must move normal to itself as it grows; this kind of growth is essentially different from that of linear facets contemplated here since the latter may grow by lateral extension of their planes without any normal motion. The purpose of the present work is (1) to specialize Herring's energy results to linear facets, and (2) to describe theoretically the lateral growth of linear facets on the assumption that it is energetically induced. The theory is developed quantitatively for two separate cases in which the transport mechanism is assumed to be (1) evaporation-condenstation of a metal in quasi-equilibrium with its own vapour and (2) surface diffusion. A third transport mechanism, volume diffusion, applying either to defect diffusion in the solid or to evaporation-condensation in the presence of an ambient gas, is discussed semi-quantitatively. All of the calculations draw upon a previous treatment (Mullins 1958) of thermal grooving at a moving grain boundary. In fact, the facet system is essentially constructed of two half thermal grooves separated by the facet plane which they intersect at a definite contact angle (see fig. 1). Growth then proceeds by the peeling back on the lower side and the building up on on the upper side of the curved surface where it contacts the facet plane.

---

† Prolonged heating is sometimes required, presumably to remove the dissolved $O_2$ from the Ag.

‡ The evidence on this point is conflicting. Moreau and Benard (1959) claim the complex planes tend to have simple crystallographic orientations.

The calculations will yield the possible shapes of the facet profile, as well as the facet size as a function of time, in terms of the basic physical parameters of the solid. For the case of surface diffusion, the results will depend, in addition to geometrical factors (e.g. the facet slope), on a parameter expressing the relative ease with which surface diffusion occurs on the facet and on the curved surface. Thus by experimental observation of facet profiles, it should be possible to determine the value of this interesting parameter.

Fig. 1



(a)



(b)
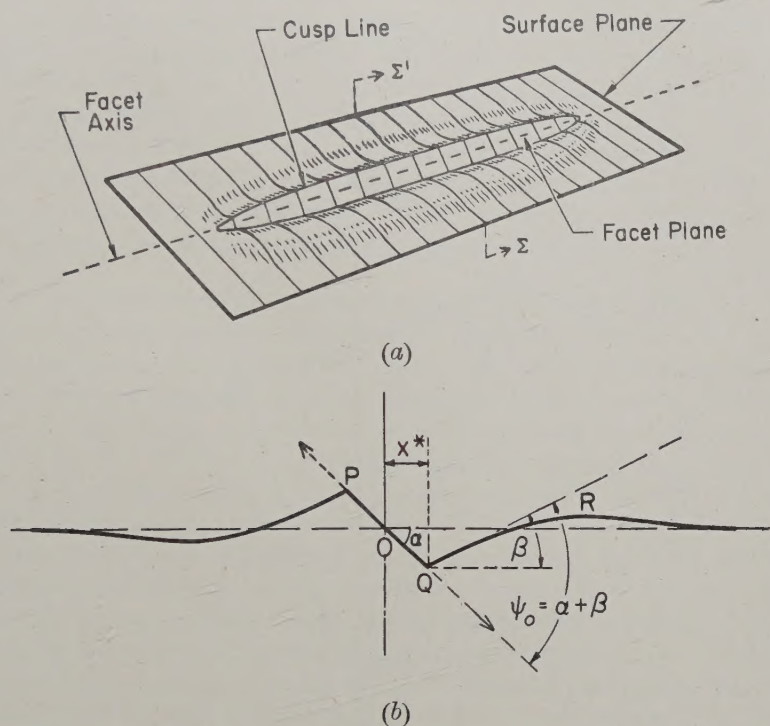
(a) A linear facet.
(b) Section $\Sigma' \Sigma$ of fig. 1 (a). Vertical exaggeration $\sim 3 \times$.

## § 2. Energetic Conditions for the Type of Faceting Described by the Analytic Theory

### 2.1. Conditions under which Linear Faceting occurs

Herring's (1951 b) analysis of faceting gives the conditions, in terms of the Wulff plot, under which the break-up (faceting) of an initially flat surface into a hill and valley structure will be accompanied by a decrease in surface free energy. The general hill and valley structure contemplated in the analysis is composed of three sets of planes whose normals have three distinct non-coplanar orientations. The analysis leads to the important theorem that a flat surface will spontaneously facet if, and

only if, its orientation is not one of those present or degeneratively present†
on the Gibbs–Wulff equilibrium form.

In the present paper we wish to confine attention to the two-dimensional
break-up of a surface into (parallel) linear facets that have a slender shape,
elongated in a direction hereafter referred to as the facet axis. To apply
Herring's theorem to the linear facet system, it is convenient to consider
the section of the Wulff $\gamma$-plot formed by a plane passing through the
origin and normal to the facet axis. The two-dimensional graph formed
on this plane will be termed a $\gamma_2$-plot (see fig. 2), the subscript denoting its

Fig. 2
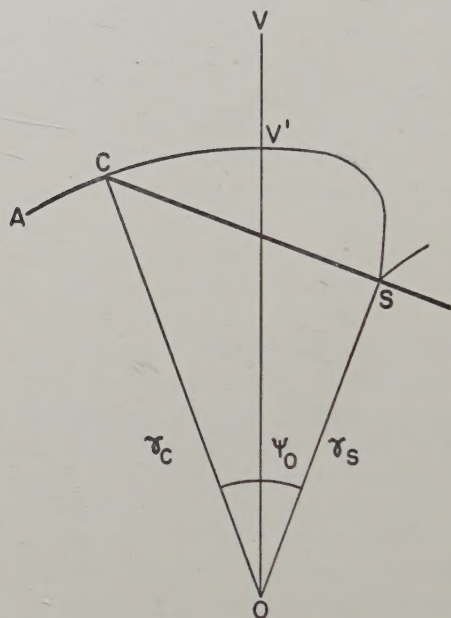


Wulff plot and form corresponding to interfaces in fig. 1 (*b*).

dimensionality and distinguishing it from the ordinary three-dimensional
$\gamma$-plot. The $\gamma_2$-plot is, of course, simply a planar plot of the surface
energy of all planes whose normals are perpendicular to the facet axis.
In addition to the $\gamma_2$-plot, it is convenient to consider the two-dimensional
form obtained by a Wulff construction carried out in the two dimensions

---

† We define an orientation to be degeneratively present if its Wulff plane
touches but is not tangent to the Gibbs–Wulff form (e.g. if the plane touches
a corner or an edge of the form). The $\gamma$-plot must be consulted to determine
whether an orientation is degeneratively present. This case, omitted from the
statement of the theorem by Herring (1951 b), must be included since an orienta-
tion degeneratively present, and therefore not visible on the Gibbs–Wulff
form, will not spontaneously facet.

of the $\gamma_2$-plot, using lines instead of planes in an obvious way. This form, termed the meta-equilibrium form (illustrated, in part, in fig. 2), is generally different from the corresponding section of the true three-dimensional equilibrium force. It is the equilibrium form under the constraint that all surfaces be parallel to the facet axis.

The condition for linear faceting along a particular axis is now easily stated in terms of the meta-equilibrium form and Herring's theorem in a two dimensional version, namely, a surface will decrease its free energy by linearly faceting along a certain axis if, and only if, the orientation of that surface is not present nor degeneratively present on the meta-equilibrium form of the corresponding $\gamma_2$-plot. Two additional points need to be made: (1) a surface which according to the preceding statement will not linearly facet along a certain axis may still facet in another mode, that is, either linearly along a different axis or in a general hill and valley fashion; (2) a surface for which linear faceting along a certain axis is allowed will not necessarily do so to any large extent; nucleation and growth factors may, for example, favour a competing mode of faceting.

### 2.2. *The Type of $\gamma_2$ Plot required by the Analytic Theory*

Figure 2 shows a portion of the $\gamma_2$-plot (light lines plus arc AC) and the associated meta-equilibrium form (heavy line ACS) that corresponds to the facet system depicted in fig. 1†. The line OV is supposed to be normal to the original surface which is clearly not present on the equilibrium form shown in fig. 2. Neither can it be degeneratively present in our case since, as we shall see, the $\gamma_2$-plot must be assumed circular at V' with O as centre in order for the analytic theory to apply. Therefore, according to Herring's theorem, the surface will facet. It may be shown that the maximum reduction in surface free energy (for linear facets whose axes are perpendicular to the paper) occurs when the orientation OV breaks up into a hill and valley structure composed of the two orientations that bracket the missing range, namely, OS and OC. Because of nucleation difficulties, however, faceting will presumably start at isolated places only, leading in each case to a profile with a range of orientations as shown in fig. 1; in this profile, the orientation of the simple surface corresponds to OS in fig. 2 and the orientations present on both complex surfaces correspond to the range from OC to a little beyond OV.

In order for the analytic theory of facet growth to apply, $\gamma$ must be constant over the orientations exposed on the complex surface. It follows that the $\gamma_2$-plot must be a circular arc (with O as the centre) from C to a little beyond V' (the intersection of $\gamma_2$ and OV). Clearly, the $\gamma$-plot whose $\gamma_2$ sections will be most likely to fulfil our requirements will consist of a sphere with spike-like indentations or cusps along a few special

---

† It is assumed that the $\gamma_2$-plot nowhere penetrates the Herring tangent circle (Herring 1951 b) for the points C and S, thereby guaranteeing the presence of the relevant portion of the equilibrium form shown (i.e. OS and the differential element of AC at C).

orientations.   If the cusps are truly sharp, the corresponding facets on the
equilibrium form will be flat as illustrated by CS in fig. 2.   If the cusps
become blunted or rounded, the corresponding facets on the equilibrium
form (e.g. CS) will become curved and will bow slightly outward away
from O.   The plot will still be acceptable and will still lead to a facet
system of the type shown in fig. 1 (b) provided it continues to fulfil all the
other requirements previously mentioned.   The orientation of the facet
plane PQ (in fig. 1 (b)), however, will no longer correspond to OS of fig. 2,
but rather will correspond to the orientation which the bowed surface
assumes at C (on the equilibrium form).

The angle $\psi_0$ of intersection of the complex and simple surfaces, at P
and Q in fig. 1 and at C in fig. 2, is determined by Herring's (1951 a) equation
for interface equilibria.   The equation resolved parallel and perpendicular
to the facet line yields the respective relations

$$\gamma_c \cos \psi_0 = \gamma_s, \qquad \ldots \ldots \ldots \quad (1\,a)$$

$$\gamma_c \sin \psi_0 \leqslant \frac{\partial \gamma_s}{\partial \theta} \qquad \ldots \ldots \ldots \quad (1\,b)$$

where $(1/\gamma_s)(\partial \gamma_s / \partial \theta)$ is the left-hand slope of the cusp at S.   Equation (1 a)
is clearly valid from fig. 2.   It was used by Moore (1958) in his earlier work
to determine the ratio of $\gamma$'s from measurements of $\psi_0$.   Equation (1 b)
expresses the requirement that the torque exerted by the complex surface
on the simple surface be insufficient to twist it out of its low energy orienta-
tion.   In terms of fig. 2, eqn. (1 b) requires the left-hand slope of the cusp
at S to exceed the slope at S of a circle through O and tangent to $\gamma_2$ at C.
If $\gamma_c$ is not quite independent of orientation, or if the cusp at S is blunted
and the line CS (fig. 2) bows outward, there will be additional torque
terms introduced into eqns. (1) that can also be suitably interpreted in
fig. 2.   In any case, the angle $\psi_0$ between the simple and complex surfaces
at the cusp line of the facet system (P and Q of fig. 1) will always be equal
to the angle between the corresponding surfaces on the equilibrium form
(C of fig. 2).   (The driving force per atom available to restore the inter-
section angle to its equilibrium value, from any slight local departure, is
much greater than that responsible for facet growth.)

### 2.3. *Facet Nucleation*

The decomposition of a planar surface of a specified orientation into a
linear combination of two or more distinct orientations is closely analogous
to the decomposition of a homogeneous phase into a linear combination
of two or more distinct phases.   The free energy change that accompanies
either process may be determined by a graphical analysis of the appropriate
free energy plot: in the first case, by the application of the tangent rule to
the graph of free energy vs. composition; and in the second case, by the
application of Herring's (1951 b) constructions to the Wulff plot.   For
either process to occur spontaneously a reduction in free energy must
occur.

Similarly there is a close analogy between facet nucleation and nucleation of a new phase. Orientation corresponds to composition, a line of orientation discontinuity to a sharp phase boundary, and a surface element of large curvature to a region with a large composition gradient. A formal theory of homogeneous facet nucleation may be constructed along the lines of the homogeneous nucleation of phase transformations. Furthermore, imperfections, when present, presumably play a similar role in the two cases in promoting nucleation.

It is possible for an initially plane interface to break up into other orientations without requiring nucleation. For example, it follows from the analysis of Herring (1951 b) that if the tangent sphere through P (i.e. a sphere passing through the origin and tangent to the $\gamma$-plot at P) lies entirely outside of the $\gamma$-plot in a neighbourhood of P, except at P, the surface of orientation OP will spontaneously break up into orientations that may differ from the original one by arbitrarily small amounts†. In other words, arbitrarily small fluctuations in the original orientation will lower the free energy. The situation is closely analogous to the spinodal condition in phase transformations (Cahn and Hillard 1959) for which composition fluctuations occur spontaneously and nucleation is not required.

If, on the other hand, the tangent sphere lies entirely inside of the $\gamma_3$-plot in a neighbourhood of P, except at P, it follows from the same analysis that a finite minimum free energy must be expended in forming a nucleus (i.e. a region of orientations distinct from the original one) which may then grow spontaneously. This situation will presumably hold for our case since in the neighbourhood of V′ = P, the $\gamma_2$-plot is a circular arc with O as the centre, and will therefore lie outside the circle through O and tangent at V′.

§ 3. ADDITIONAL GENERAL ASSUMPTIONS AND APPROXIMATIONS

(i) The facet whose development is to be described is assumed to be isolated from the other facets as shown in fig. 1. Although the curved branches of the surface bordering the facet have orientations that are neither present nor degeneratively present on the meta-equilibrium form, and hence are subject to additional faceting, there is presumably a nucleation barrier as already discussed. In other words, we assume nucleation of facets to be limited and are studying the growth of one facet prior to the time it impinges on others. It will be shown later that the rate at which facets widen and begin to impinge on each other increases rapidly with decreasing $\alpha$. This means that the present assumption should become more easily realized as $\alpha$ approaches $\psi_0$ and should become less suitable as $\alpha$ decreases.

(ii) The facet is assumed to be long and slender so that the profile obtained on a section normal to its axis is a slowly changing function of

---

† The wave length of the fluctuation is assumed large enough so that the dependence of $\gamma$ upon curvature need not be considered.

position along the axis. This permits us to treat the widening of the facet as a two-dimensional problem.

(iii) The maximum slope attained by the complex surface with respect to the initially flat surface will be assumed to be small. In effect this means $|\tan \beta| \ll 1$. This restriction is necessary to permit an analytic treatment as previously shown (Mullins 1957). In the future we shall use the abbreviations $m \equiv \tan \beta$ and $n \equiv -\tan \alpha$ ($n$ will be positive); our condition is then $|m| \ll 1$.

## § 4. Facet Growth by Evaporation-condensation

In this section, facet growth will be analysed under the assumption that the transport mechanism is evaporation-condensation. There are two different cases depending on whether or not the metal vapour diffuses in an ambient gas: in the case considered first, it is assumed that the return flux of metal vapour onto the solid is uniform so that diffusion is not involved. This case typically occurs in a one component system of a metal in contact with its own vapour. It is referred to as case $E_1$, in conformity with previous notation (Mullins 1959). In the second case considered, it is assumed that the metal is surrounded by an ambient gas. The metal vapour concentration adjacent to each surface element is assumed to have the equilibrium value determined by the curvature through the Gibbs–Thompson relation. Transport then occurs by diffusion (potential flow) of the metal vapour through the ambient gas. This case is called $E_2$ and is treated only by an order of magnitude calculation as the exact treatment, even restricted to the foregoing assumptions, is very involved.

### 4.1. *Case $E_1$*

Under the foregoing assumptions for case $E_1$, and under the supposition that the flux of atoms leaving each surface element is the same as it would be if the vapour were locally in equilibrium with that element, the surface profile $y(x, t)$ has been shown (Mullins 1957) to obey the equation

$$\frac{\partial y}{\partial t} = A \frac{\partial^2 y}{\partial x^2} \quad . \quad . \quad . \quad . \quad . \quad . \quad . \quad (2)$$

where

$$A = \frac{p_0 \Omega^2 \gamma_s}{(2\pi M)^{1/2}(kT)^{3/2}}$$

in which $\Omega$ is the atomic volume, $\gamma_s$ is the surface free energy, $p_0$ is the vapour pressure (dynes cm$^{-2}$) in equilibrium with a flat surface, $M$ is the weight of a molecule, and $kT$ has its usual meaning. Because of the symmetry of the facet system, we need only consider the right half in applying eqn. (2). Under the conditions of an initially flat surface, i.e. $y(x, o) = 0$, and a constant slope at $x = 0$, i.e. $(\partial y/\partial x)_{x=0} = m'$, the solution of eqn. (2) has been shown (Mullins 1957) to be

$$y(x, t) = -2m'(At)^{1/2} \, \text{ierfc} \left[ \frac{x}{2(At)^{1/2}} \right] \quad . \quad . \quad . \quad (3)$$

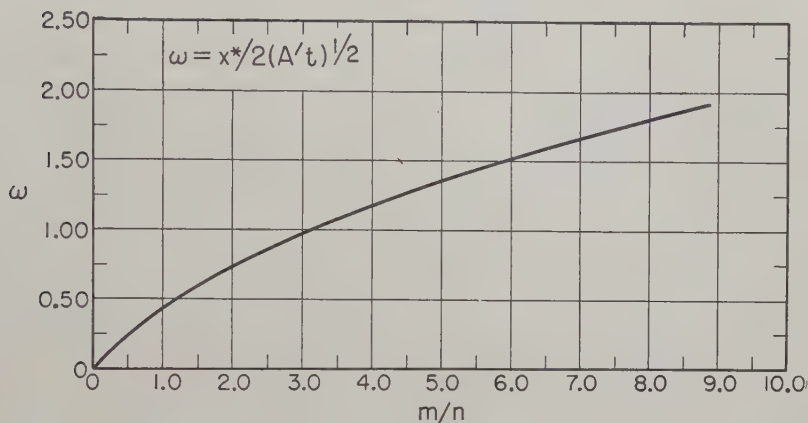where ierfc is the integral error function defined as

$$\text{ierfc}\,(u) = \int_u^\infty \text{erfc}\,(s)\,ds$$

in which

$$\text{erfc}\,(s) = \frac{2}{\sqrt{\pi}} \int_s^\infty \exp\,(-\epsilon^2)\,d\epsilon.$$

Equation (3) clearly represents a profile of constant shape expanding uniformly away from the origin such that the distances from any profile point to the origin is $\sim$ (time)$^{1/2}$.

Fig. 3



Plot of $\omega(m/n)$ for evaporation-condensation, case $E_1$.

Fig. 4
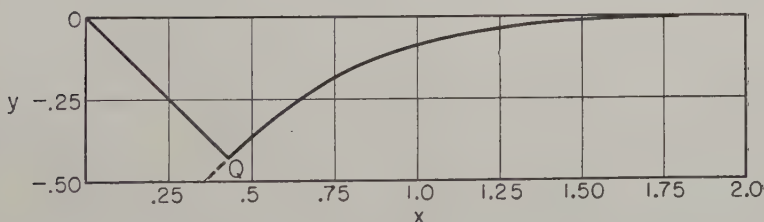


Evaporation-condensation profile (case $E_1$) shown for $m = n = 1$.

The function given by eqn. (3) is easily adapted to solve our faceting problem. Thus for a suitable value of $m'$, the portion of the corresponding curve to the right of the point Q (fig. 4) will be shown to represent the complex surface. Let

$$\left.\begin{array}{l} x^* = \omega 2(At)^{1/2} \\ y^* = -n\omega 2(At)^{1/2} \end{array}\right\} \quad \cdot\ \cdot\ \cdot\ \cdot\ \cdot\ \cdot\ \cdot\ \cdot\ (4)$$

be the coordinates of Q. Then if $\omega$ can be determined, the width of the facet as a function of time will follow from eqn. (4). But this is easily accomplished by combining the relations $y(x^*, t) = y^*$, and $(\partial y/\partial x)_{x=x^*} = m$ with eqns. (3) and (4) to obtain

$$\text{ierfc}\,(\omega) = (n/m')\omega$$

and

$$m = m'\,\text{erfc}\,(\omega), \qquad \cdot \quad \cdot \quad \cdot \quad \cdot \quad \cdot \quad \cdot \quad \cdot \quad (5)$$

or eliminating $m'$

$$\frac{m}{n} = \omega\,\frac{\text{erfc}\,(\omega)}{\text{ierfc}\,(\omega)}. \qquad \cdot \quad \cdot \quad \cdot \quad \cdot \quad \cdot \quad \cdot \quad \cdot \quad (6)$$

Equation (6) implicitly defines $\omega(m/n)$. Figure 3 shows a plot of the result of assigning values to $\omega$, and then computing $m/n$ from eqn. (6) and the tables of Carslaw and Yaeger (1947).

For a given ratio of $m/n$, determined by the geometry of the surfaces, the value of $\omega$ is computed from eqn. (6) (or fig. 3). This value of $\omega$, substituted into eqn. (4) yields the facet width (and depth) as a function of the time. Substituted into eqn. (5), together with $m$, it yields the value of $m'$ that must be used in eqn. (3) to yield a description of the complex surface profile. The case shown in fig. 4 is for the values $m = n = 1$, $\omega = 0 \cdot 43$, $m' = 1 \cdot 78$. Note that multiplication of all ordinates of any solution by the same factor $k$ does not affect the ratio's $m/n$ or $m/m'$ and hence yields a solution that widens at the same rate as the original one and that has a slope at the point Q of km.

Finally, the area $A(t)$ between the profile and the original surface, for $x \geqslant 0$, is given by

$$A(t) = -\int_0^{x^*} nx\,dx + \int_{x^*}^{\infty} y(x, t)\,dx.$$

Using eqns. (3) and (4), and the properties of repeated integrals of the error function, we may easily prove the simple result

$$A(t) = -m\,At.$$

### 4.2. *Case $E_2$*

In the following order of magnitude calculation, the metal surface is assumed to be in contact with an ambient gas so that transport occurs by gaseous diffusion of the metal vapour. From previous work on thermal grooving (Mullins 1960), the profile shape for facet growth under the action of volume diffusion is expected to be quite similar to that developed by surface diffusion, even with regard to the presence of a maximum above the original surface to the right of P (e.g. fig. 1 (*b*)). We can thus estimate the radius of curvature $R$ of the complex surface to be the same as that of the circle which is tangent to the profile at Q and to the original surface. From elementary geometry, we have

$$R \simeq \frac{nx^*}{m^2},$$

With the radius of curvature is associated an excess concentration $\Delta C$ of vapour over that present above a flat surface of an amount $\Delta C = C_0 \Omega \gamma_\mathrm{S}/kTR$. The number of atoms/cm$^2$, $J$, leaving the right branch of the surface has the order of magnitude given by

$$J \simeq \frac{D_g \Delta C}{(x^* + Rm)} = \frac{D_g \Delta C}{x^*(1 + n/m)}$$

where $D_g$ is the diffusion coefficient of metal atoms in the vapour. But for a given surface element $\partial y/\partial t = -\Omega J$. Applying this relation at Q together with the relation

$$\frac{dx^*}{dt} = -\frac{1}{n}\left(\frac{\partial y}{\partial t}\right)_{x=x^*},$$

and combining the preceding equations we have

$$\frac{dx^*}{dt} = \frac{A'}{(n/m)^2(1 - n/m)kTx^{*2}}$$

where

$$A' = \frac{C_0 D_g \gamma_\mathrm{S} \Omega^2}{kT}$$

in conformity with previous notation. Integrating the preceding equation we obtain

$$x^* = \left[\frac{A't}{(n/m)^2(1 + n/m)}\right]^{1/3} \simeq \frac{m}{n}(A't)^{1/3} \qquad \cdots \cdots \quad (7)$$

the last step holding when $m \ll n$. We see that the facet width is proportional to the third root of the time as required from similitude arguments (Herring 1950) for profiles of constant shape. Apart from the value of the fractional root, eqn. (7) is of the same form as eqn. (4) provided we set $2\omega \simeq m/n$ in eqn. (7).

The calculation just presented can be applied to estimate the contribution of self diffusion to facet growth; we need only set the product $C_0 D_g \Omega$, appearing in the parameter $A'$, equal to the coefficient of self diffusion $D$. The resulting parameter $C = D\gamma_\mathrm{S}\Omega/kT$ has been discussed previously (Mullins 1959).

## § 5. Facet Growth by the Mechanism of Surface Diffusion

In this section surface diffusion is assumed to be the process whereby material is transported to form the facet. It has been shown from arguments of similitude (Herring 1950), discussed in § 6.3, that surface diffusion must dominate over other transport processes for geometries whose scale is sufficiently small, e.g. in the initial phases of facet growth. Furthermore, surface diffusion has been shown to account for experimental data on the closely related phenomena of thermal grooving in Cu (Mullins and Shewmon 1959) for groove widths up to several tens of microns. Therefore surface diffusion is expected to dominate most of the observable

process of faceting, at least in the cases for which the metal vapour pressure is not too high (i.e. not exceeding $\sim 10$–$100$ microns as established in § 6.3).

The surface diffusion coefficient of the complex surface, in the direction normal to the facet axis, is assumed to be constant over the range of exposed orientations; it is denoted by $D_c$. The surface diffusion coefficient on the facet (simple) plane may in general differ markedly from $D_c$ and is denoted by $D_s$. It is also assumed that on both surfaces, the chemical potential gradient and the matter current are parallel. If a second component is strongly adsorbed on the surface undergoing faceting (e.g. oxygen adsorption on silver), both $D_s$ and $D_c$ may differ appreciably from the values they would assume on a clean surface.

## 5.1. *Transport on the Complex Surface*

The chemical potential $\mu$ of atoms on the complex curved surface is given by the Gibbs–Thompson relation (Herring 1951) which, under assumptions (ii) and (iii), and the assumption of the constancy of $\gamma_c$, becomes

$$\mu = -\gamma_c \Omega \frac{\partial^2 y}{\partial x^2} \qquad \cdots \cdots \cdots \quad (8)$$

where atoms on the flat complex surface are taken as the reference $\mu = 0$. From this relation it has been shown (Mullins 1957) that (1) the current of atoms $J$ in the complex surface is given by

$$J = -\frac{D_c}{kT} \frac{\partial \mu}{\partial x} \cdot \nu = \frac{D_c \nu \gamma_c \Omega}{kT} \frac{\partial^3 y}{\partial x^3} \qquad \cdots \cdots \quad (9)$$

where $\nu$ is the number of atoms per cm$^2$ that participate in the diffusion†, and (2) that the profile function $y(x, t)$ must satisfy the differential equation requiring the divergence of $J$ to equal the rate of build-up of the profile, namely,

$$\frac{\partial y}{\partial t} + B \frac{\partial^4 y}{\partial x^4} = 0; \qquad \cdots \cdots \quad (10)$$

where

$$B = \frac{D_c \Omega^2 \nu \gamma_c}{kT}$$

## 5.2. *Transport on the Facet Plane*

The current of material $J$ on the facet plane will be given by $J = -(\nu' D_s / kT) \nabla \mu$ where $\nabla \mu$ is the gradient of chemical potential of atoms on the facet surface and $\nu'$ is the number of atoms per cm$^2$ of the facet

---

† Equation (9) may be taken as defining the product $D_c \cdot \nu$, other quantities being in principle measurable ($J$ being in excess matter–current associated with the surface in the Gibbsian sense). If $\nu$ is then assigned a standard value such as $\Omega^{-2/3}$, the corresponding $D_c$ may be regarded as the effective $D_c$ that would explain the observed transport if it all occurred in a layer of depth corresponding to the value of $\nu$.

plane that participate in the diffusion. (The same comment applies to $\nu'$ as made in the footnote concerning the $\nu$ of eqn. (9).) We wish to show that for all cases of interest, $\nabla\mu$ will be constant at all points of the facet at any given moment. The relaxation time $\tau_r$ required to establish steady-state flow across the facet for a given current of atoms entering Q and leaving P will be approximately given by $\tau_r \simeq S^2/D_s$ where $S$ is the length OQ. The time $\tau_c$ required for facet growth to produce a $1\%$ change in the current of atoms entering Q and leaving P can be seen from eqns. (9), (13) and (16), to be given by

$$\tau_c \simeq \frac{10^{-3}S^4 \cos^4\alpha}{\omega^4 B}.$$

For diffusion on the facet to be steady state it is necessary that $\tau_r < \tau_c$ or substituting values $S^2 > 10^3 B\omega^4/D_s \cos^4\alpha$. A typical value of $B$ near the melting point is $10^{-19}\,\mathrm{cm^4\,sec^{-1}}$ whereas $D_s$ should not be less than $10^{-6}\,\mathrm{cm^2\,sec^{-1}}$. Thus $S > 10^{-5}\omega^2/\cos^2\alpha$. This relation, whose right-hand side is probably over-estimated, is satisfied for detectable values of $S$ (at least $10^{-4}\,\mathrm{cm}$) in all cases that fulfil the small slope approximation provided there are none for which $\omega$ becomes too large (i.e. provided that $n \lesssim 3m \ll 1$). Since none of the reported cases fall under the latter exception, we take $\nabla\mu = (\mu_Q - \mu_P)/2S$.

Although no specific model of transport on the simple plane is required, we discuss one briefly for the sake of concreteness. Consider a low index plane with a certain concentration $x_{+1}$ of superior atoms resting on top of the plane, and a certain concentration $x_{-1}$ of layer vacancies in the plane. Statistical considerations require $x_{-1}x_{+1} = \mathrm{const.}\exp(-V/kT)$ where $V$ is the energy of formation of a pair (i.e. a layer vacancy and a superior atom). The situation is analogous to that existing in a semiconductor where superior atoms correspond to electrons in the conduction band, layer vacancies to holes in the valence band, and $V$ to the energy gap for pair creation; other concepts such as carrier lifetime and mobility also apply. At P there would, in general, be a surplus of superior atoms and a deficiency of layer vacancies on the facet plane because of the curvature of the adjacent convex surface. At Q the reverse situation would hold, causing matter to diffuse from P to Q both in the superior level (analogous to electron current) and in the level below (analogous to hole current). The relative strength of the currents would depend on the relative mobilities of the superior atoms and layer vacancies. It would even be possible for the difference in mobilities to change sign with temperature preventing a simple Arrhenius description of the diffusion. This simple model could be modified by invoking more than two levels and would be affected by such things as the presence of adsorbed atoms.

## 5.3. *Description of the Facet System*

Since the theoretical problem is symmetric under the preceding assumptions we consider only the right-half of the facet system. The

procedure is now to solve eqn. (10) for the complex surface QR ∞ subject to the condition of a fixed slope at $x = x^*$ (the $x$ coordinate of Q)

$$\left(\frac{\partial y}{\partial x}\right)_{x=x^*} = \tan \beta \equiv m, \qquad \cdots \quad \cdots \quad (11)$$

and the condition of continuity of current across $x = x^*$

$$-\frac{D_s v' \mu_Q}{kTS} = \frac{D_c v \Omega \gamma_c}{kT}\left(\frac{\partial^3 y}{\partial x^3}\right)_{x=x^*}$$

where $S$ is the length OQ

$$\left(\mu_P = -\mu_Q \quad \text{so that} \quad \frac{\mu_Q - \mu_P}{2S} = \frac{\mu_Q}{S}\right).$$

Assuming $\mu$ to be continuous across the point $x = x^*$, and using Eqn. (8), the preceding equation may be rearranged to give

$$\left(\frac{\partial^3 y}{\partial x^3}\right)_{x=x^*} = \frac{d}{S}\left(\frac{\partial^2 y}{\partial x^2}\right)_{x=x^*} \qquad \cdots \quad \cdots \quad (12)$$

where

$$d = \frac{D_s v'}{D_s v} = \frac{D_s}{D_c}$$

(assigning the standard value $v = v' = \Omega^{-2/3}$).

Fig. 5
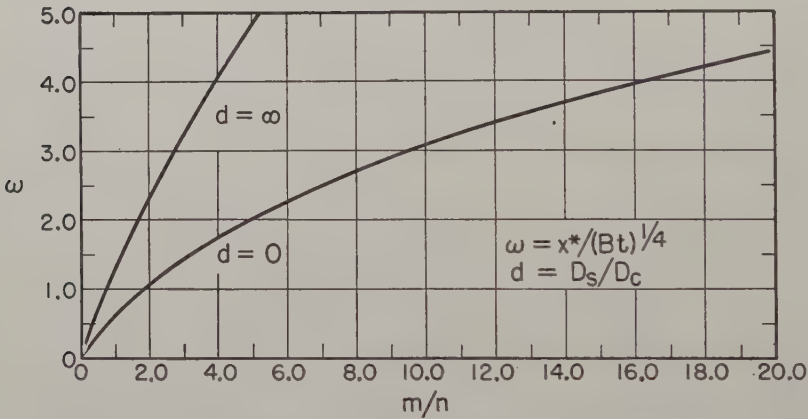


Plot of $\omega(m/n)$ for the two limiting cases of surface diffusion.

We now assert that if the function $y(x, t)$ is written in a form that represents a curve expanding uniformly away from the origin O, such that the distance from any point on the curve to the origin increases as $t^{1/4}$, then it can be adjusted to meet all the conditions required for a description of the complex surface profile (extending from $x^*$ to ∞). This form is suggested by previous work on thermal grooves (Mullins 1957, 1958).

Thus substituting the expression

$$y(x, t) = m(Bt)^{1/4} Z\left[\frac{x}{(Bt)^{1/4}}\right] \quad \cdot \quad \cdot \quad \cdot \quad \cdot \quad \cdot \quad \cdot \quad (13)$$

into eqn. (10) and denoting the variable $x/(Bt)^{1/4}$ by $u$, we obtain

$$Z'''' - (u/4)Z' + \tfrac{1}{4}Z = 0, \quad \cdot \quad \cdot \quad \cdot \quad \cdot \quad \cdot \quad (14)$$

where a prime denotes differentiation of $Z(u)$ with respect to $u$. This ordinary differential equation has four linearly independent solutions which may be written so that two of them, $Z_1$ and $Z_2$, vanish at $u = -\infty$ and the other two, $Z_3$ and $Z_4$, vanish at $u = +\infty$. (The explicit solutions are obtained in the Appendix.) Any linear combination of the latter solutions of the form

$$Z = C_3 Z_3 + C_4 Z_4 \quad \cdot \quad \cdot \quad \cdot \quad \cdot \quad \cdot \quad \cdot \quad (15)$$

satisfies eqn. (14) and behaves properly at $+\infty$. The two constants $C_3$ and $C_4$ are chosen to satisfy eqns. (11) and (12), in the manner discussed below.

As in the previous sections, the boundary conditions, given by eqns. (11) and (12), must be applied at the moving point Q. Since Q will always be on the straight line through the origin that represents the facet, our expanding solution requires its coordinates to be

$$\left. \begin{aligned} x^* &= \omega(Bt)^{1/4} \\ y^* &= -\omega n(Bt)^{1/4} \end{aligned} \right\} \quad \cdot \quad \cdot \quad \cdot \quad \cdot \quad \cdot \quad (16)$$

and

where $\omega$ is independent of time. Substituting eqn. (13) into eqns. (11) and (12) and making the evaluations of $x = x^*$ with the use of eqn. (16) we obtain

$$Z'(\omega) = 1 \quad \cdot \quad \cdot \quad \cdot \quad \cdot \quad \cdot \quad \cdot \quad \cdot \quad (17)$$

and

$$\frac{1}{(Bt)^{1/2}} Z'''(\omega) = \frac{d}{S} \frac{1}{(Bt)^{1/4}} Z''(\omega) = \frac{d \cos \alpha}{x^*(Bt)^{1/4}} Z''(\omega)$$

or

$$\omega Z'''(\omega) = d \cos \alpha Z''(\omega). \quad \cdot \quad \cdot \quad \cdot \quad \cdot \quad (18)$$

In addition to these two boundary conditions that essentially determine $C_3$ and $C_4$ in eqn (15), another relation is required to determine $\omega$. This is easily obtained since we must have $y(x^*, t) = y^*$ or, substituting from eqns. (13) and (16),

$$Z(\omega) = -\omega \, (n/m). \quad \cdot \quad \cdot \quad \cdot \quad \cdot \quad \cdot \quad (19)$$

Substituting eqn. (15) into eqns. (17), (18) and (19) we obtain three equations for the three quantities $C_3$, $C_4$ and $\omega$ in terms of the geometric factors $\alpha$ (or $n$), and $m$, and the diffusion ratio $d$, namely,

$$\left. \begin{aligned} C_3 Z_3(\omega) + C_4 Z_4(\omega) + n/m &= 0, \\ C_3 Z_3'(\omega) + C_4 Z_4'(\omega) - 1 &= 0, \\ C_3(\omega Z_3'''(\omega) - d \cos \alpha Z_3''(\omega)) + C_4(\omega Z_4'''(\omega) - d \cos \alpha Z_4''(\omega)) &= 0. \end{aligned} \right\} \quad \cdot \quad \cdot \quad (20)$$

These equations are linear in the $C$'s so that $\omega$ must assume that value which causes the determinant of the corresponding augmented matrix to vanish for consistency (three equations in two unknowns).

In order to discuss the resulting equation and other equations that follow, it is convenient to introduce the notation

$$D_{nm} = \begin{vmatrix} Z_3^{(n)}(\omega) & Z_4^{(n)}(\omega) \\ Z_3^{(m)}(\omega) & Z_4^{(m)}(\omega) \end{vmatrix}$$

for the $2 \times 2$ determinant in which the superscripts $(m)$ and $(n)$ refer to the order of differentiation. Using this notation, it is easily verified that the augmented determinant of eqn. (20) can be expanded to give the equation

$$\omega = -\frac{m}{n} \frac{d \cos(\alpha) D_{02} - \omega D_{03}}{d \cos(\alpha) D_{12} - \omega D_{13}}. \qquad \cdots \cdots \quad (21)$$

This equation determines $\omega$ and hence from eqn. (16) the width and depth of the facet as a function of time. To calculate the profile shape of the complex surface, $C_3$ and $C_4$ must be determined from eqn. (20). Thus, using the first two equations,

$$\left. \begin{array}{l} C_3 = \dfrac{\begin{vmatrix} \dfrac{-\omega n}{m} & Z_4 \\ 1 & Z_4' \end{vmatrix}}{D_{01}}, \\[3em] C_4 = \dfrac{\begin{vmatrix} Z_3 & \dfrac{-\omega n}{m} \\ Z_3' & 1 \end{vmatrix}}{D_{01}}, \end{array} \right\} \quad \cdots \cdots \cdots \quad (22)$$

where the required value of $\omega$ must be taken from eqn. (21). Substitution into eqn. (15) of the values of $C_3$ and $C_4$ calculated from eqn. (22), and substitution of the resulting expression for $Z$ into eqn. (13) yields a description of the profile of the complex surface, i.e. $y(x, t)$ for $x \geqslant x^*$.

Numerical results will be presented in the remaining discussion for two limiting cases: (1) the case of $d = 0$ in which no material crosses the facet plane and (2) the case of $d = \infty$ in which the facet plane is a very easy path for diffusion. The calculation of results for intermediate values of $d$ is straightforward but tedious. Figure 6 shows the significance of the two limiting cases in terms of the chemical potential $\mu$ (proportional to $-y''$ on the complex surfaces) plotted across a facet. According to eqns. (9) and (10), matter drifts downhill on the $\mu$ curves with an average speed proportional to their slope, and accumulates at a rate proportional to their curvature. For the case $d = 0$, no matter crosses the facet; thus the slope of the $\mu$ curve must vanish at P and Q. Matter then drifts to the right, away from the facet plane on the right and toward it on the left. For the case $d = \infty$, the facet is essentially a short circuit that is unable to support a difference of $\mu$ across itself; thus the $\mu$ curve must vanish at P and Q. The slope imposed on the curve for $d = \infty$ clearly results in a

drift of matter across the facet plane to the left from Q to P, as well as the rightward drift farther from the facet plane.

Fig. 6



$$d = D_s/D_c = 0$$
$$d = \infty$$
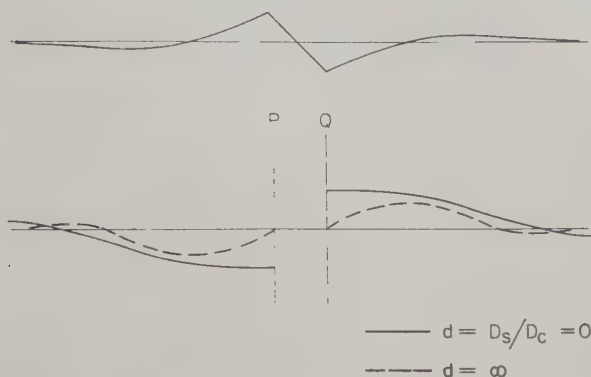
Lower figure shows schematic plot of $\mu = -\gamma_s \Omega y''$ for the two limiting cases of general profile in upper figure.

For the case $d = 0$, eqn. (21) reduces to

$$\omega \frac{D_{13}}{D_{03}} = -\frac{m}{n}, \qquad \cdots \cdots \cdots \quad (23)$$

showing $\omega$ and hence the rate of facet growth to be determined exclusively by the ratio $m/n$. The function $\omega(m/n)$, determined from eqn. (23) is plotted in fig. 5. The graph is represented up to $\omega = 3$ with an accuracy of better than 1% by the formula $[m/n](\omega) = 1\cdot281 + 0\cdot459\omega^2 - 0\cdot002422\omega^3$ (which may be inverted by solving the cubic or, for small values of $\omega$, the quadratic). Facet profiles for the case $d = 0$ are shown in fig. 8 for the

Fig. 7
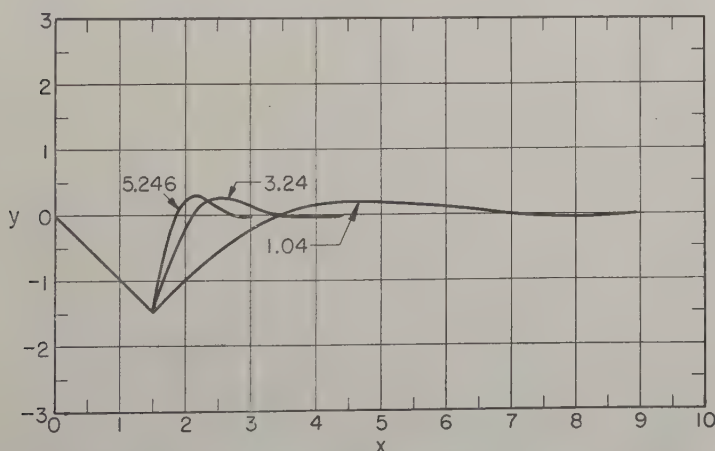


Three standardized profiles for the limiting case $d = \infty$; attached numbers give values of $m/n$.

three selected values of $m/n = 1\cdot04$, $3\cdot24$ and $5\cdot246$. The profiles are arbitrarily adjusted to make their cusps coincide (choice of time), and to make their facet lines assume an angle of $45°$ to the $x$ axis (vertical scale magnification). To obtain profiles corresponding to realistic values of $\psi_0$, all ordinates would have to be multiplied by a fractional vertical scale factor (note this would not change the ratio $m/n$).

For the case $d = \infty$, eqn. (21) reduces to

$$\omega \frac{D_{12}}{D_{02}} = -\frac{m}{n}, \qquad \qquad (24)$$

showing the functional form of $\omega$ again to be $\omega(m/n)$. This function is plotted in fig. 5 and is from two to three times greater for a given $m/n$ than the corresponding curve for $d=0$; thus faceting is two to three times faster for $d = \infty$ than for $d=0$. The graph of $\omega(m/n)$ for $d = \infty$ is represented up to $\omega = 3$ with an accuracy of better than 1% by the formula $[m/n](\omega) = 0\cdot6409 + 0\cdot09745\omega^2 - 0\cdot002422\omega^3$. Facet profiles for the case $d = \infty$ are shown in fig. 7 for the same values of $m/n$ and the same normalization convention used in the $d=0$ case (fig. 8).

Fig. 8
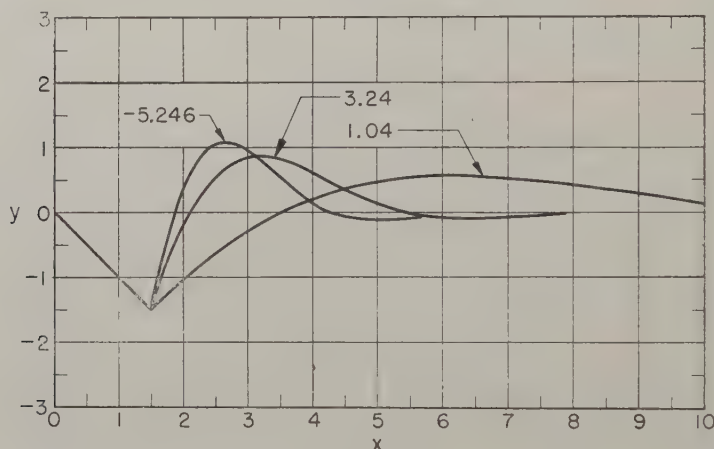


Three standardized profiles for the limiting case $d=0$; attached numbers give values of $m/n$.

The area $A(t)$ between the profile and the original surface for $x \geqslant 0$, is given by

$$A(t) = -\int_0^{x^*} nx\,dx + \int_{x^*}^{\infty} y(x,t)\,dx.$$

By employing eqns. (13) and (16) and by using eqn. (14) to effect an integration by parts, it may be shown that

$$A(t) = 2mZ'''(\omega)(Bt)^{1/2}. \qquad \qquad (25)$$

For the case $d=0$, we have $Z'''(\omega) = 0$ so that the area $A$ is zero at all times. This is expected, of course, since the initial zero area cannot

change unless material crosses the facet plane. For the case $d = \infty$, matter crosses the facet plane from Q to P (fig. 1) so that the integrated area to the right of the origin becomes negative. In fig. 9 a plot of $-Z''' = -A(t)/2m(Bt)^{1/2}$ as a function at $m/n$ is presented. Note that $Z'''(\omega)$ is proportional to the current of matter crossing point Q; eqn. (25) may also be derived by integrating this current with respect to the time.

## § 6. Discussion

### 6.1. *Geometrical Factor*

The results of all the calculations have depended on geometry through the variable $m/n$. In any physical case, however, the variable subject to direct control would be $n = -\tan\alpha$, whereas the quantity $\psi_0 = -\alpha + \beta$ would be fixed by surface energy relations. Figure 10 shows a plot of $m/n$ as a function of $n$, computed from the formula appearing in the figure for three different values of $\psi_0$, namely, $14\cdot0°$, $26\cdot6°$ and $35\cdot0°$. For any of these cases, the dependence of $\omega$ upon $n$ may be found by combining fig. 10 and figs. 3 or 5. It is clear that $\omega$ increases very sharply as $n$ falls below $\tan\psi_0$. The dotted lines on each graph are placed at positions corresponding to the value $\beta = 10°$. The small slope approximation is certainly valid to the right of each dotted line ($\beta \simeq 10°$) and should lead to semi-quantitative results some distance to the left of the dotted line.

### 6.2. *Explanation of Elongated Shape of Facet*

At the ends of a linear facet the two cusp lines are no longer parallel but curve toward each other and meet. Therefore the recession of the cusp line, caused by the transport of material, will have an axial component and the facet will lengthen. Although the complicated geometry near the end of the facet makes the calculation of the local diffusion (or evaporation) difficult, it seems clear that the advancing facet tip will attain a steady-state velocity. Furthermore, this velocity should be very large since the facet is presumably very narrow near the tip causing the recession velocity of the cusp line to be very high. In contrast, the widening of the facet at a fixed position occurs at an ever decreasing rate (eqns. (4), (7) or (16)). Therefore the facets should become elongated and assume the shape we have described as linear. If the tip velocity is in fact constant, the width of the facet at a given point should be proportional to the $n$th root of its distance from the facet tip that originally swept by the point where $n$ is the exponent of the time appearing in the widening laws (eqns. (4), (7) or (16)).

### 6.3. *Comparison of the Transport Processes*

The transport processes may be compared by comparing the speed $dx^*/dt$ of facet growth as a function of $x^*$ calculated from eqns. (4), (7) and (16), for the different mechanisms considered. When this is done, one finds ranges of $x^*$ within each of which one process is dominant. The equations

Fig. 9
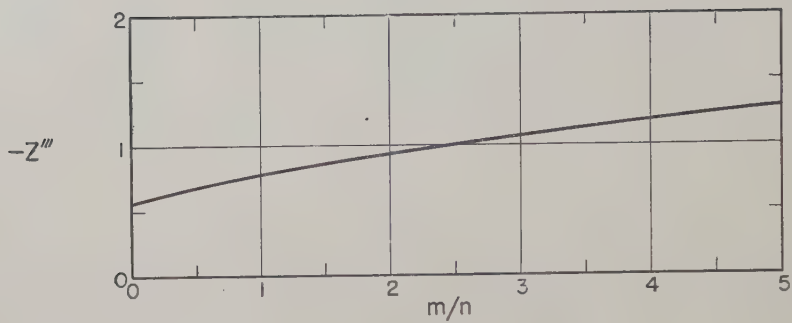


Plot of $-Z''' = -A/2m(Bt)^{1/2}$ for the case of $d = \infty$.

Fig. 10



Tan $14.0° = 0.25$

Tan $26.6° = 0.50$

Tan $35.0° = 0.70$

Dotted lines show 10° confidence limits in $\beta$

$\psi_0 = 14.0°$

$\psi_0 = 26.6°$

$\psi_0 = 35.0°$
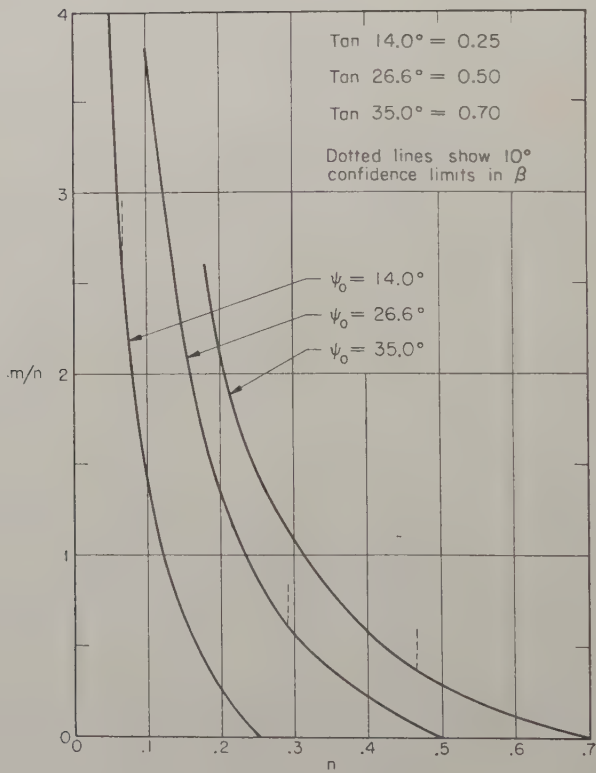
Plot of $[m/n](n)$ for three values of $\psi_0 = -\alpha + \beta$.

$$\frac{m}{n} = \frac{-1 + (\tan \psi_0)/n}{1 + (\tan \psi_0)n}.$$

that determine the ranges are the same as those previously discussed (Mullins 1959) in connection with the processes responsible for the decay to flatness of an undulating isotropic surface. (The correspondence is established by setting $x^* = \lambda/2$ in that discussion.) In the results stated below, the $\omega$'s (not to be confused with those appearing in the reference—Mullins 1959), as well as $m/n$ in case $E_2$, will be set equal to unity. They cannot be much greater than unity for the $\psi_0$'s reported in the literature without violating the small slope requirement (fig. 10); if they are much less than unity in any given case, they may be retained in the comparison and will simply have the effect of multiplying the points of division of the ranges of $x^*$. Values assumed for the other constants are $A \simeq (10^{-13}p_0)$ cm$^2$ sec$^{-1}$, $A' = (10^{-17}p_0)$ cm$^3$ sec$^{-1}$ (assuming $D_g \simeq 1$ cm$^2$ sec$^{-1}$), $B \simeq 10^{-19}$ cm$^4$ sec$^{-1}$ (assuming $D_s \simeq 10^{-4}$ cm$^2$ sec$^{-1}$), and $C \simeq 10^{-15}$ cm$^3$ sec$^{-1}$ (assuming $D_v \simeq 10^{-8}$ cm$^2$ sec$^{-1}$). In the values of $A$ and $A'$, $p_0$ is the equilibrium vapour pressure (in dynes cm$^{-2}$) near the melting point and is left unspecified since it differs widely among different metals. The results are that surface diffusion always dominates for small enough $x^*$. Which process takes over as $x^*$ increases depends on the relative size of the constants and on whether the system leading to case $E_1$ or to case $E_2$ is assumed. Consider system $E_1$ first, so that $A' = 0$. Then, according to our values, volume diffusion will become dominant in the range $x_1^* \leqslant x^* \leqslant x_2^*$, where $x_1^* \simeq 10^{-4}$ cm and $x_2^* \simeq 10^{-2}p_0^{-1}$. For $x^* > x_2^*$ evaporation will dominate. If, however, $p_0$ is so large that $x_2^* < x_1^*$, then volume diffusion will never be important and evaporation will gain dominance directly over surface diffusion when $x^* > x_3^* \simeq 10^{-3}p_0^{-1/2}$.

Consider next system $E_2$ so that $A = 0$. Evaporation or volume diffusion will dominate for large $x^*$, depending on whether $A'$ is greater than or less than $C$, which in turn depends on whether $p_0$ is greater than or less than $\sim 10^2$ dynes cm$^{-2}$. Call $l$ the larger of $A'$ or $C$; the corresponding process becomes dominant over surface diffusion for $x^* > x_4^* = 10^{-19}/l$.

As the temperature falls below the melting point, $x_1^*$, $x_2^*$, $x_3^*$ and $x_4^*$ will all increase, assuming the enthalpies of activation for surface diffusion, volume diffusion, and evaporation obey the inequality $H_s < H_v < H_E$.

Experiments on thermal grooving (Mullins and Shewmon 1959) indicate that the estimate given above of $x_1^*$ is at least an order of magnitude too low, i.e. that surface diffusion remains dominant over volume diffusion up to and above $x_1^* \simeq 10\,\mu$. An error of this magnitude is not surprising in view of the rough nature of the volume diffusion calculation as well as possible deviations in the diffusion coefficients from the 'typical' values assumed.

### 6.4. *Distinction between the* $d=0$ *and* $d=\infty$ *Cases in the Regime of Surface Diffusion*

Assuming one or the other of the two limiting cases describes the faceting, there are two ways by which they may be distinguished: by the rate of

facet growth; and by the shape of the profile. Considering the growth first, we have already noticed (fig. 5) that for any particular values of $m/n$, $\omega$ is about twice as big and correspondingly $x^*$ increases about twice as fast in the case $d = \infty$ as in the case $d = 0$. If the constant $B$ could be determined to within a little better than an order of magnitude (e.g. from grooving experiments) this would suffice to distinguish the cases since from eqn. (16) a factor of 2 in $x^*$ is equivalent to a factor of $2^4 = 16$ in $B$.

When $B$ is unknown, it may still be possible to distinguish the cases using rate data. Thus consider the logarithm of eqn. (16), namely, $\ln x^* = \ln \omega + \ln (Bt)^{1/4}$. Since $\omega$ is a different function of $m/n$ in the two limiting cases, a plot of $\ln x^*$ vs. $m/n$, for varying orientations and fixed annealing times, should distinguish the cases. The method fails if the functions $\omega(m/n)$ for the two limiting cases have a constant ratio for then, using an obvious notation, $\ln \omega_{d=\infty} = \ln \text{const.} + \ln \omega_{d=0}$ and the constant cannot be distinguished from the unknown $\ln (Bt)^{1/4}$. Hence, this method depends upon the rather small departure from constancy of the ratio of the two $\omega$ functions.

Concerning the shape of the profiles, there are several marked differences between the case $d = 0$ and $d = \infty$. First as previously noted, the area from the origin to $+ \infty$ will always be zero in the case $d = 0$ but will be negative in the case $d = \infty$ by an amount depending on $m$ and $n$ (and the time) as shown in fig. 9. Secondly, because of the boundary condition given by eqn. (18), the profile of the complex surface rises parabolically from the facet line in the case $d = 0$ (the third derivation vanishes at $x^*$) and linearly in the case $d = \infty$ (the second derivative vanishes at $x^*$). Thirdly, an examination of figs. 7 and 8 show that although there are maxima in the profiles above the original surface in both cases they are much less pronounced for a given facet depth in the $d = \infty$ case than in the $d = 0$ case. And lastly for a given value of $m/n$ the ratio of the abscissa of the maxima to the abscissa $x^*$ is noticeably less in the case $d = \infty$ than in the case $d = 0$. Of course, for any particular $m/n$, the entire profile may be calculated for the two limiting cases as explained in §5.3, and is then available for comparison with experiment.

It is difficult to decide *a priori* which limiting case, $d = 0$ or $\infty$, is more, likely. Diffusion on low index planes might be expected to be more rapid than on the complex surface. If, however, there is a considerable pre-ferential adsorption of molecules (e.g. $O_2$) on the simple plane, diffusion may be impeded. Moore (1958) has observed secondary facets forming parallel to and on the curved shoulders of a large primary facet. If the surface energy hypothesis is correct, we must conclude that, since these secondary facets do not seem to markedly interrupt the primary profile, either they formed very late in the development of the primary facet, or the diffusing matter associated with the development of the primary facet crossed the secondary facets rather easily. If the latter alternative were true, it would constitute evidence against the case $d = 0$. Of course, it may turn out that neither limiting case applies, but that a finite value of $d$ is required to describe faceting.

## 6.5. *Facet Decay*

As already stated, the facets formed on Ag, heated in the presence of air, are found to disappear upon prolonged heating in $N_2$ (Chalmers *et al.* 1948). We may hypothesize that the change in the chemical environment (presumably the removal of $O_2$) has altered the $\gamma$-plot so that the original surface now belongs to the equilibrium Wulff shape. If this is true, and if in addition the orientations of the faceted surface exposed to $N_2$ have approximately the same $\gamma$, then the flattening process is formally described by an analysis previously given by the writer (Mullins 1959). The surface diffusion coefficient may differ from that which is effective on the complex surfaces during faceting because of the change in chemical environment.

## 6.6. *Additional Remarks*

The assumption of isolation for a facet could be dropped, and parallel facets whose complex shoulders overlap could be treated by applying appropriate boundary conditions. For the case of each transport process, the description would require twice as many mathematical solutions to fulfil the boundary conditions between facets as used in the present treatment, e.g. in the case of surface diffusion solutions $Z_1$ and $Z_2$ of eqn. (14) would be required in addition to $Z_3$ and $Z_4$. The description would be very involved in all but one case, namely that in which the parallel facets are equally spaced. In this case, a Fourier series solution of eqns. (2) or (10) would describe the faceting all the way to completion.

The meandering departure from linearity of some of the observed facets (Moore 1958), and the variability in their spacing, indicates the presence of large-scale undulations in the surface level, probably due to a loss of material by evaporation. The observed topographies, especially for small $\alpha$, suggest the recession of strips of complex surface over the facet planes, at rates depending on their loss of material by evaporation. Evaporation, if it occurs, does not necessarily obviate surface energy as the primary cause of the faceting.

---

# APPENDIX

### Mathematical Representation of $Z_3$ and $Z_4$

We have seen that solution of eqn. (10) of the form

$$y(x, t) = m(Bt)^{1/4} Z\left[\frac{x}{(Bt)^{1/4}}\right] \quad . \quad . \quad . \quad . \quad (A\,1)$$

can be made to satisfy the boundary conditions of the faceting problem provided there are two linearly independent functions $Z_3(u)$ and $Z_4(u)$ that vanish as $u \to \infty$ and that satisfy the ordinary differential equation obtained by substituting eqn. (A 1) into eqn. (10), namely,

$$Z'''' - \frac{uZ'}{4} + \frac{Z}{4} = 0 \quad . \quad . \quad . \quad . \quad . \quad (A\,2)$$

where the prime denotes differentiation with respect to $u$. In this Appendix, we will find expressions for $Z_3$ and $Z_4$.

The assumption of a power series solution

$$Z(u) = \sum_{n=0}^{\infty} a_n u^n \qquad \text{. . . . . . .} \quad \text{(A 3)}$$

of eqn. (A 2) leads in the ordinary way to the recursion relation

$$a_{n+4} = a_n \frac{n-1}{4(n+1)(n+2)(n+3)(n+4)} . \qquad \text{. . . .} \quad \text{(A 4)}$$

The four linearly independent solutions of eqn. (A 2) correspond to the four undetermined coefficients of the power series, $a_0$, $a_1$, $a_2$, $a_3$, eqn. (A 4) determining all succeeding coefficients. As we shall see, however, the requirement that

$$\lim_{u \to \infty} Z(u) = 0$$

imposes two linear relations between the first four $a$'s leaving only two to be independently chosen. To agree with notation previously used, the two corresponding independent solutions, vanishing at $+\infty$, are denoted by $Z_3(u)$ for the choice $a_1 = 1$, $a_3 = 0$, and $Z_4(u)$ for the choice $a_1 = 0$, $a_3 = 1$. In order to determine $a_0$ and $a_2$ so that

$$\lim_{u \to \infty} Z_3 = Z_4 = 0,$$

as well as to obtain integral representation of $Z_3$ and $Z_4$, it is convenient to apply the Laplace transform method directly to eqn. (10). The result is

$$B \frac{d^4 \bar{y}}{dx^4} + p\bar{y} = 0 \qquad \text{. . . . . . .} \quad \text{(A 5)}$$

where

$$\bar{y}(x, p) = \int_0^{\infty} \exp(-pt) y(x, t) \, dt,$$

and the condition $y(x, 0)$ has been used. Of the four linearly independent solutions of eqn. (A 5), i.e. $\exp[\omega(p/B)^{1/4}x]$ where $\omega$ is one of the four fourth roots of $-1$, only two vanish as $x \to \infty$; the other two become infinite and must be discarded. Taking $\omega$ to be the particular root given by $\omega = 1/\sqrt{2} + i/\sqrt{2}$, we may write the allowed solutions in complex notation as

$$\bar{y}(x, p) = J \exp[\omega^2 (p/B)^{1/4}x] + J^* \exp[\omega^3 (p/B)^{1/4}x] \qquad \text{. .} \quad \text{(A 6)}$$

where $J$ and $J^*$ are conjugate (as are $\omega^2$ and $\omega^3$) so that $\bar{y}$ is a real function of $p$, as it must be to yield a real $y(x, t)$.

Now the first four $a$'s of eqn. (A 3) may be related to the $J = J_1 + iJ_2$ of eqn. (A 6) by the following procedure: the quantities $y(0, t)$, $y'(0\ t)$, $y''(0, t)$, and $y'''(0, t)$ (where prime denotes differentiation with respect to $x$) are expressed as functions of the $a$'s and the time by employing eqns. (A 1) and (A 3); these expressions are then transformed to obtain the corresponding set of quantities $\bar{y}(0, p)$, $\bar{y}'(0, p)$, $\bar{y}''(0, p)$ and $\bar{y}'''(0, p)$. But the

latter set of quantities can also be evaluated from eqn. (A 6). Equating the corresponding expressions for each $\bar{y}$, $\bar{y}'$, etc., and simplifying we obtain the relations

$$
\begin{aligned}
a_0 &= \frac{p^{5/4}}{B^{1/4}\Gamma(5/4)m} 2J_1, \\
a_1 &= \frac{-\sqrt{2}p^{5/4}}{B^{1/4}m}(J_1+J_2), \\
a_2 &= \frac{p^{5/4}}{B^{1/4}\Gamma(3/4)m}J_2, \\
a_3 &= \frac{p^{5/4}}{B^{1/4}3\sqrt{2}\Gamma(1/2)m}(J_1-J_2).
\end{aligned}
\qquad \cdots \quad \text{(A 7)}
$$

Eliminating $J_1$ and $J_2$ we obtain the consistency relations between the $a$'s that guarantee

$$
\lim_{u\to\infty} Z(u)=0,
$$

namely,

$$
\begin{aligned}
a_0 &= \frac{-1}{\sqrt{2}\Gamma(5/4)}[a_1-6\Gamma(1/2)a_3], \\
a_2 &= \frac{-1}{2\sqrt{2}\Gamma(3/4)}[a_1+6\Gamma(1/2)a_3].
\end{aligned}
\qquad \cdots \quad \text{(A 8)}
$$

Equations (A 3), (A 4), (A 8) and the definition $a_1=1$, $a_3=0$ and for $Z_3$ and $a_1=0$, $a_3=1$ for $Z_4$ completely define the functions.

Alternatively. $Z_3$ and $Z_4$ may be given integral representations by using eqn. (A 7) to evaluate $J$ for the two cases, substituting these values into eqn. (A 6), applying the Laplace inversion formula (Tranter 1956) given by eqn. (A 9) and then comparing with eqn. (A 1):

$$
y(x, t)=\frac{1}{2\pi i}\int_{\mathcal{N}} \exp(pt)\,\bar{y}(x, p)\,dp. \qquad \cdots \quad \text{(A 9)}
$$

The performance of the inversion is somewhat involved owing to a branch point at the origin in the function $\bar{y}$ and to the necessity of integration by parts and change of variables at several important steps. The contour integration is carried out in much the same way (i.e. with regard to the path $\mathcal{N}$ and the selection of the appropriate branches of the multiple valued function) as that required to invert $F(p)=p^{-5/4}$ into $f(t)=t^{1/4}\Gamma(5/4)$. The details of the evaluation are too many to be given and only the result will be presented, namely,

$$
\begin{aligned}
Z_3(u) &= -\frac{8}{\pi}\int_0^\infty d\epsilon\, \epsilon^2 \exp(-\epsilon^4)+u+\frac{2}{\pi}\int_0^\infty d\epsilon \exp(-\epsilon^4)\frac{\cos(u\epsilon)-1}{\epsilon^2}, \\
Z_4(u) &= \frac{48\Gamma(1/2)}{\pi}\int_0^\infty d\epsilon\, \epsilon^2(-\epsilon^4) \\
&\quad -\frac{12\Gamma(1/2)}{\pi}\cdot\int_0^\infty d\epsilon \exp(-\epsilon^4)\frac{\exp(-\epsilon u)+\sin(\epsilon u)-1}{\epsilon^2},
\end{aligned}
\qquad \text{(A 10)}
$$

That these expressions for $Z_3$ and $Z_4$ do satisfy eqn. (A 2) may be verified by substitution (using integration by parts where necessary). That they vanish at $u = + \infty$ may be shown by first integrating the last integral in each line by parts (taking $dv = d\epsilon/\epsilon^2$) and then applying theorems giving the limits of Dirichlet integrals of the type that occur in the proof of Fourier series formulae (Courant and Hilbert 1953). Finally the connection of the integral representation of eqn. (A 10) to the series representation of eqn. (A 3), and the verification that the coefficients $a_1$ and $a_3$ are

Table 1.    Coefficients as a function of $\omega$ for the two limiting cases

| $\omega$ | $d = 0$ | | $d = \infty$ | |
|---|---|---|---|---|
| | $C_3$ | $C_4$ | $C_3$ | $C_4$ |
| 0·0 | 1·000 | 0·000 | 1·000 | $-9{\cdot}410 \times 10^{-2}$ |
| 0·2 | 1·120 | $-7{\cdot}789 \times 10^{-3}$ | $9{\cdot}875 \times 10^{-1}$ | $-1{\cdot}137 \times 10^{-1}$ |
| 0·4 | 1·249 | $-1{\cdot}852 \times 10^{-2}$ | $9{\cdot}447 \times 10^{-1}$ | $-1{\cdot}359 \times 10^{-1}$ |
| 0·6 | 1·381 | $-3{\cdot}277 \times 10^{-2}$ | $8{\cdot}628 \times 10^{-1}$ | $-1{\cdot}606 \times 10^{-1}$ |
| 0·8 | 1·511 | $-5{\cdot}114 \times 10^{-2}$ | $7{\cdot}319 \times 10^{-1}$ | $-1{\cdot}874 \times 10^{-1}$ |
| 1·0 | 1·631 | $-7{\cdot}422 \times 10^{-2}$ | $5{\cdot}408 \times 10^{-1}$ | $-2{\cdot}161 \times 10^{-1}$ |
| 1·2 | 1·730 | $-1{\cdot}026 \times 10^{-1}$ | $2{\cdot}810 \times 10^{-1}$ | $-2{\cdot}457 \times 10^{-1}$ |
| 1·4 | 1·796 | $-1{\cdot}367 \times 10^{-1}$ | $-6{\cdot}956 \times 10^{-2}$ | $-2{\cdot}754 \times 10^{-1}$ |
| 1·6 | 1·788 | $-1{\cdot}768 \times 10^{-1}$ | $-5{\cdot}131 \times 10^{-1}$ | $-3{\cdot}037 \times 10^{-1}$ |
| 1·8 | 1·760 | $-2{\cdot}229 \times 10^{-1}$ | $-1{\cdot}064$ | $-3{\cdot}285 \times 10^{-1}$ |
| 2·0 | 1·616 | $-2{\cdot}748 \times 10^{-1}$ | $-1{\cdot}731$ | $-3{\cdot}485 \times 10^{-1}$ |
| 2·2 | 1·356 | $-3{\cdot}316 \times 10^{-1}$ | $-2{\cdot}521$ | $-3{\cdot}599 \times 10^{-1}$ |
| 2·4 | $9{\cdot}531 \times 10^{-1}$ | $-3{\cdot}921 \times 10^{-1}$ | $-3{\cdot}434$ | $-3{\cdot}597 \times 10^{-1}$ |
| 2·6 | $3{\cdot}783 \times 10^{-1}$ | $-4{\cdot}541 \times 10^{-1}$ | $-4{\cdot}463$ | $-3{\cdot}442 \times 10^{-1}$ |
| 2·8 | $-3{\cdot}966 \times 10^{-1}$ | $-5{\cdot}148 \times 10^{-1}$ | $-5{\cdot}595$ | $-3{\cdot}090 \times 10^{-1}$ |
| 3·0 | $-1{\cdot}398$ | $-5{\cdot}703 \times 10^{-1}$ | $-6{\cdot}802$ | $-2{\cdot}496 \times 10^{-1}$ |
| 3·2 | $-2{\cdot}647$ | $-6{\cdot}154 \times 10^{-1}$ | $-8{\cdot}044$ | $-1{\cdot}611 \times 10^{-1}$ |
| 3·4 | $-4{\cdot}158$ | $-6{\cdot}440 \times 10^{-1}$ | $-9{\cdot}264$ | $-3{\cdot}894 \times 10^{-2}$ |
| 3·6 | $-5{\cdot}932$ | $-6{\cdot}488 \times 10^{-1}$ | $-1{\cdot}039 \times 10^{1}$ | $1{\cdot}202 \times 10^{-1}$ |
| 3·8 | $-7{\cdot}954$ | $-6{\cdot}211 \times 10^{-1}$ | $-1{\cdot}131 \times 10^{1}$ | $3{\cdot}227 \times 10^{-1}$ |
| 4·0 | $-1{\cdot}019 \times 10^{1}$ | $-5{\cdot}514 \times 10^{-1}$ | $-1{\cdot}193 \times 10^{1}$ | $5{\cdot}675 \times 10^{-1}$ |
| 4·2 | $-1{\cdot}285 \times 10^{1}$ | $-4{\cdot}298 \times 10^{-1}$ | $-1{\cdot}212 \times 10^{1}$ | $8{\cdot}553 \times 10^{-1}$ |
| 4·4 | $-1{\cdot}693 \times 10^{1}$ | $-2{\cdot}462 \times 10^{-1}$ | $-1{\cdot}163 \times 10^{1}$ | $1{\cdot}191$ |
| 4·6 | $-2{\cdot}118 \times 10^{1}$ | $8{\cdot}697 \times 10^{-3}$ | $-1{\cdot}041 \times 10^{1}$ | $1{\cdot}544$ |
| 4·8 | $-2{\cdot}538 \times 10^{1}$ | $3{\cdot}421 \times 10^{-1}$ | $-8{\cdot}206$ | $1{\cdot}926$ |
| 5·0 | $-2{\cdot}920 \times 10^{1}$ | $7{\cdot}590 \times 10^{-1}$ | $-4{\cdot}859$ | $2{\cdot}310$ |

as required for $Z_3$ and $Z_4$, may be established by expanding the functions depending on $u$ in a Taylor series about $u = 0$, and integrating the series term by term. When this procedure is carried out, the result is

$$Z_3 = \sum_{n=0}^{\infty} a_n^{(3)} u^n$$

Table 2.    Values of the functions $Z_3$ and $Z_4$

| $\omega$ | $Z_3(u)$ | $Z_4(u)$ |
|---|---|---|
| 0·0 | $-7{\cdot}801 \times 10^{-1}$ | 8·296 |
| 0·2 | $-5{\cdot}916 \times 10^{-1}$ | 8·182 |
| 0·4 | $-4{\cdot}261 \times 10^{-1}$ | 7·867 |
| 0·6 | $-2{\cdot}829 \times 10^{-1}$ | 7·396 |
| 0·8 | $-1{\cdot}615 \times 10^{-1}$ | 6·809 |
| 1·0 | $-6{\cdot}071 \times 10^{-2}$ | 6·140 |
| 1·2 | $2{\cdot}068 \times 10^{-2}$ | 5·422 |
| 1·4 | $8{\cdot}414 \times 10^{-2}$ | 4·684 |
| 1·6 | $1{\cdot}313 \times 10^{-1}$ | 3·950 |
| 1·8 | $1{\cdot}640 \times 10^{-1}$ | 3·240 |
| 2·0 | $1{\cdot}839 \times 10^{-1}$ | 2·570 |
| 2·2 | $1{\cdot}930 \times 10^{-1}$ | 1·954 |
| 2·4 | $1{\cdot}930 \times 10^{-1}$ | 1·401 |
| 2·6 | $1{\cdot}859 \times 10^{-1}$ | $9{\cdot}169 \times 10^{-1}$ |
| 2·8 | $1{\cdot}732 \times 10^{-1}$ | $5{\cdot}040 \times 10^{-1}$ |
| 3·0 | $1{\cdot}565 \times 10^{-1}$ | $1{\cdot}626 \times 10^{-1}$ |
| 3·2 | $1{\cdot}373 \times 10^{-1}$ | $-1{\cdot}094 \times 10^{-1}$ |
| 3·4 | $1{\cdot}167 \times 10^{-1}$ | $-3{\cdot}162 \times 10^{-1}$ |
| 3·6 | $9{\cdot}591 \times 10^{-2}$ | $-4{\cdot}634 \times 10^{-1}$ |
| 3·8 | $7{\cdot}569 \times 10^{-2}$ | $-5{\cdot}575 \times 10^{-1}$ |
| 4·0 | $5{\cdot}676 \times 10^{-2}$ | $-6{\cdot}060 \times 10^{-1}$ |
| 4·2 | $3{\cdot}962 \times 10^{-2}$ | $-6{\cdot}166 \times 10^{-1}$ |
| 4·4 | $2{\cdot}462 \times 10^{-2}$ | $-5{\cdot}967 \times 10^{-1}$ |
| 4·6 | $1{\cdot}193 \times 10^{-2}$ | $-5{\cdot}539 \times 10^{-1}$ |
| 4·8 | $1{\cdot}615 \times 10^{-3}$ | $-4{\cdot}950 \times 10^{-1}$ |
| 5·0 | $-6{\cdot}377 \times 10^{-3}$ | $-4{\cdot}260 \times 10^{-1}$ |
| 5·2 | $-1{\cdot}219 \times 10^{-2}$ | $-3{\cdot}524 \times 10^{-1}$ |
| 5·4 | $-1{\cdot}603 \times 10^{-2}$ | $-2{\cdot}787 \times 10^{-1}$ |
| 5·6 | $-1{\cdot}816 \times 10^{-2}$ | $-2{\cdot}082 \times 10^{-1}$ |
| 5·8 | $-1{\cdot}886 \times 10^{-2}$ | $-1{\cdot}439 \times 10^{-1}$ |
| 6·0 | $-1{\cdot}840 \times 10^{-2}$ | $-8{\cdot}732 \times 10^{-2}$ |
| 6·2 | $-1{\cdot}709 \times 10^{-2}$ | $-3{\cdot}970 \times 10^{-2}$ |
| 6·4 | $-1{\cdot}517 \times 10^{-2}$ | $-1{\cdot}396 \times 10^{-3}$ |
| 6·6 | $-1{\cdot}289 \times 10^{-2}$ | $2{\cdot}774 \times 10^{-2}$ |
| 6·8 | $-1{\cdot}045 \times 10^{-2}$ | $4{\cdot}827 \times 10^{-2}$ |
| 7·0 | $-8{\cdot}016 \times 10^{-3}$ | $6{\cdot}109 \times 10^{-2}$ |
| 7·2 | $-5{\cdot}723 \times 10^{-3}$ | $6{\cdot}730 \times 10^{-2}$ |
| 7·4 | $-3{\cdot}664 \times 10^{-3}$ | $6{\cdot}810 \times 10^{-2}$ |
| 7·6 | $-1{\cdot}899 \times 10^{-3}$ | $6{\cdot}472 \times 10^{-2}$ |
| 7·8 | $-4{\cdot}591 \times 10^{-4}$ | $5{\cdot}834 \times 10^{-2}$ |
| 8·0 | $6{\cdot}498 \times 10^{-4}$ | $5{\cdot}005 \times 10^{-2}$ |
| 8·2 | $1{\cdot}442 \times 10^{-3}$ | $4{\cdot}080 \times 10^{-2}$ |
| 8·4 | $1{\cdot}946 \times 10^{-3}$ | $3{\cdot}135 \times 10^{-2}$ |
| 8·6 | $2{\cdot}202 \times 10^{-3}$ | $2{\cdot}233 \times 10^{-2}$ |
| 8·8 | $2{\cdot}255 \times 10^{-3}$ | $1{\cdot}419 \times 10^{-2}$ |
| 9·0 | $2{\cdot}150 \times 10^{-3}$ | $7{\cdot}211 \times 10^{-3}$ |
| 9·2 | $1{\cdot}933 \times 10^{-3}$ | $1{\cdot}546 \times 10^{-3}$ |
| 9·4 | $1{\cdot}645 \times 10^{-3}$ | $-2{\cdot}768 \times 10^{-3}$ |
| 9·6 | $1{\cdot}323 \times 10^{-3}$ | $-5{\cdot}790 \times 10^{-3}$ |
| 9·8 | $9{\cdot}956 \times 10^{-4}$ | $-7{\cdot}646 \times 10^{-3}$ |
| 10·0 | $6{\cdot}857 \times 10^{-4}$ | $-8{\cdot}504 \times 10^{-3}$ |

where

$$a_0^{(3)} = -\frac{2\Gamma(3/4)}{\pi},$$

$$a_1^{(3)} = 1,$$

$$\left.\begin{array}{l} a_{2n}^{(3)} = \dfrac{(-1)^n \Gamma((2n-1)/4)}{(2n)!\, 2\pi}, \\[2mm] a_{2n+1}^{(3)} = 0, \end{array}\right\} \quad n \geqslant 1 \qquad \cdots \quad \text{(A 11)}$$

and

$$Z_4 = \sum_{n=0}^{\infty} a_n^{(4)} u^n$$

where

$$a_0^{(4)} = \frac{12\Gamma(1/2)\Gamma(3/4)}{\pi},$$

$$a_1^{(4)} = 0,$$

$$\left.\begin{array}{l} a_{2n}^{(4)} = \dfrac{-3\Gamma(1/2)}{(2n)!\,\pi}\, \Gamma\!\left(\dfrac{2n-1}{4}\right), \\[3mm] a_{2n+1}^{(4)} = [1-(-1)^n]\,\dfrac{3\Gamma(1/2)\Gamma(n/2)}{(2n+1)!\,\pi}, \end{array}\right\} \quad n \geqslant 1. \qquad \text{(A 12)}$$

Thus we have closed expressions for the $n$th coefficient of either series and do not need to rely on eqn. (A 4) to construct the coefficients. The result is the same, or course, whichever procedure is used as may be verified by employing the properties of the $\Gamma$ function (Margenau and Murphy 1943). The determinations of $Z_3$ and $Z_4$, that appear in table 2, were made to four significant figures for selected values of the argument in the interval $0 \leqslant u \leqslant 10$ by employing a Datatron electronic computer to evaluate the series representations of eqns. (A 11) and (A 12). Similarly those $D$'s that were necessary to evaluate the expressions given by eqns. (22), (23) and (24) were calculated by obtaining the series for the required derivatives of the $Z$'s from eqns. (A 11) and (A 12), multiplying these series together as specified by the definitions of the $D$'s, and evaluating the result on the Datatron computer; the values of $C_3$ and $C_4$ needed in eqn. (15) appear in table 1 for a range of values of $\omega$ in the two limiting cases $d = 0$ and $d = \infty$.

REFERENCES

CAHN, J. W., and HILLARD, J. E., 1959, *J. chem. Phys.*, **31,** 688.
CARSLAW, H. S., and JAEGER, J. C., 1947, *Conduction of Heat in Solids* (London: Oxford University Press).
COURANT, R., and HILBERT, D., 1953, *Methods of Mathematical Physics* (New York: Interscience Publishers).
CHALMERS, B., KING, R., and SHUTTLEWORTH, R., 1948, *Proc. roy. Soc.* A, **193,** 465.
FRANK, F. C., 1958, *Growth and Perfection of Crystals*, edited by R. H. Doremus, B. W. Roberts and D. Turnbull (New York: John Wiley & Sons), p. 411.
HENDRICKSON, A. A., and MACHLIN, E. S., 1955, *Acta Met.*, **3,** 64.
HERRING, C., 1950, *J. appl. Phys.*, **21,** 301; 1951 a, *Physics of Powder Metallurgy* edited by W. E. Kingston (New York: McGraw-Hill Book Company); 1951 b, *Phys. Rev.*, **82,** 87; 1952, *Structure and Properties at Solid Surfaces*, edited by R. Comer and C. S. Smith (Chicago: University of Chicago Press).
HIRTH, J. P., and POUND, G. M., 1960, *J. phys. Chem.*, **64,** 619.
HONDROS, E. D., and MOORE, A. J. W., 1960, *Acta Met.*, **8,** 647.
MARGENAU, H., and MURPHY, G. M., 1943, *The Mathematics of Physics and Chemistry* (New York: D. van Nostrand Co.), p. 89.
MOORE, A. J., 1958, *Acta Met.*, **6,** 293.
MOREAU, J., and BENARD, J., 1959, *C.R. Acad. Sci., Paris*, **248,** 1658.
MULLINS, W. W., 1957, *J. appl. Phys.*, **28,** 333; 1958, *Acta Met.*, **6,** 414; 1959, *J. appl. Phys.*, **30,** 77; 1960, *Trans. Amer. Inst. min. (metall.) Engrs*, **218,** 354.
MULLINS, W. W., and SHEWMON, P. G., 1959, *Acta Met.*, **7,** 163.
TRANTER, C. J., 1956, *Integral Transforms in Mathematical Physics* (Methuen).

# An Electron Microscope Examination of Small Cobalt Particles Precipitated in a Gold Matrix

By P. Gaunt

Department of Physics, University of Sheffield, Sheffield, 10

and J. Silcox

Cavendish Laboratory, University of Cambridge†

## Abstract

Transmission electron microscope observations have been made on thin foils of a gold 1·5% cobalt alloy aged at 565°c after quenching from 880°c. The observations suggest that most of the ferromagnetic cobalt precipitate particles are in the form of discs in {100} planes which are arranged in sheets, also on {100} planes. The contribution to the coercivity of the alloy from these particles due to shape anisotropy is small and the high coercivity of the alloy is probably due to some other type of anisotropy.

In a recent paper by one of us (Gaunt 1960), the magnetic properties of cobalt, precipitated from a gold 1·5% cobalt alloy, were discussed. It was suggested that the high coercivity of these alloys (up to 2050 oe), could be explained in terms of the shape anisotropy of small single domain cobalt particles, of rod-like shape, and precipitated in a face-centred cubic form. It was therefore of interest to view the particles directly using the thin film electron microscope technique to determine their shape and size.

Thin foils of the alloy, about 0·2 mm thick were prepared by the cold rolling of specimens which had been used in the magnetic investigation. The foils were annealed in evacuated silica capsules at 880°c, the cobalt being in solid solution at this temperature, and were quenched by breaking the capsules under water. The foils were then annealed for various times at 565°c and thin films, suitable for direct viewing in a Siemens Elmiskop I electron microscope, were prepared by electropolishing in a solution of concentrated HCl. The microscope was operated using an accelerating voltage of 100 kv and a beam current of 30 μA.

Figures 1 and 2‡ show areas in a specimen which was water quenched and aged for 5 min at 565°c. In both areas, the plane of the foil is parallel

---

† Now at Department of Engineering Physics, Cornell University, Ithaca, New York.

‡ All figures are shown as plates.

to the (100) plane of the gold matrix. In fig. 1, rows of elongated holes, A, and certain contrast effects, B, are observed. The rows of holes are parallel to the [010] and [001] directions. None of these effects is observed in unaged water quenched material. It is therefore assumed that the holes, A, arise through the etching out of precipitate particles cutting the foil surface and that the contrast effects, B, are due to precipitate particles still lying within the foil. In fig. 2 an area is shown where the particles along [010] and [001] directions have not been etched out. The rows of particles are marked S.

Areas in which the plane of the foil is (110) and (112) have also been examined. In these cases, the directions of the rows of holes corresponding to etched out precipitates are consistent with the traces of {100} planes. Thus in the (110) orientation, the rows are parallel to [1$\bar{1}$0], corresponding to the plates precipitated on (001) planes at 90° to the foil surface, and to [001], corresponding to plates precipitated on (010) and (100) planes at 45° to the foil surface. In the (112) orientation, the two sets of precipitates on {100} planes at 65° to the foil are etched out whereas the set on {100} planes at 35° to the foil surface remain in the foil.

These observations on foils in the (100), (110) and (112) orientations suggest that the precipitates are arranged in sheets on {100} planes. The perpendicular distance between the sheets (from figs. 1 and 2) appears to be of the order of $\frac{1}{2}\mu$.

The determination of the form of the individual precipitates is complicated by the contrast effects. These may be due to the coherency strains between the precipitate particles and the matrix (there is a disregistry of $\sim 12\%$ between the face-centred cubic Co and Au lattices). Figures 2 and 3 show areas of the foil in the (100) and (110) orientations respectively in which none of the precipitates is etched out. In the (100) foil, black streaks, C, are seen parallel or nearly parallel to [001] and [010] but in the (110) foil, the streaks are parallel only to [1$\bar{1}$0]. This implies that many of the individual precipitates are in the form of discs lying in {100} planes. Thus the streaks C are discs viewed edge on and the other features B are discs in planes close to the foil plane. Certain other features (e.g. at D on fig. 4), however, are not consistent with this interpretation. These features could be due to rod-like precipitates but preliminary estimates suggest that the total volume precipitated in the form of these particles is small (i.e. $\sim 5\%$ of the total).

The conclusions drawn from these observations are that, at this stage of the precipitation at least, the precipitates of cobalt are in the form of disc-shaped particles on {100} planes which are clustered in the form of sheets also on {100} planes. According to the theory of Stoner and Wohlfarth (1948), there will be no contribution to the coercivity of an array of small isolated ferromagnetic particles from those particles which are isotropic and disc-like in shape. Although the rod-like precipitates which may be present can contribute to the coercivity, the total volume of precipitated cobalt in this form is too small to explain the high coercivities

observed in the aged gold cobalt specimens. The micrographs show, however, that the particles are not precipitated at random but are clustered in sheets on {100} planes. There must therefore be a contribution to the coercivity from interaction between the particles. Wohlfarth (1955) has shown that for two weakly interacting isotropic spheres of volume $V$, magnetization $I$ and separation $r$, the 'interaction coercivity' is given by $H_c = 3VI/r^3$. For the non-uniform rotation ('fanning process'), suggested by Jacobs and Bean (1955), this becomes $2VI/r^3$. It is doubtful whether these formulae will be strictly valid for close approach of the spheres since uniform magnetization is assumed, but assuming uniform magnetization and fanning rotation, the maximum interaction coercivity, for two touching spheres, is $\sim I$. It seems unlikely that two interacting discs will greatly exceed this value.

Measurements of remanent magnetization (Gaunt 1960), suggest, however, that in a water-quenched alloy aged for 5 min at 565°C, 25% of the total magnetization is associated with precipitates or groups of precipitates, having intrinsic coercivities greater than $\sim 5I$ (7500 oe). Rod-like particles can have intrinsic coercivities $\sim 6I$ but it is estimated from the photographs that less than 5% of the total precipitate is in this form.

Further work may indicate whether there is any large contribution to the coercivity to be expected from magnetocrystalline or magnetostriction effects.

## ACKNOWLEDGMENTS

*Note added in proof.*—After this paper had been submitted for publication a communication dealing with precipitation from a gold 5% cobalt alloy aged at 450°C was published by Campbell and Muldawer (1961). They reported observations on the precipitate morphology which differ from those reported here for a gold 1·5% cobalt alloy aged at 565°C. Further work has been carried out by the present authors on foils oriented parallel to (014), (114), (123), (125) and (127) planes of the gold matrix which confirms that the precipitate particles are clustered on {100} planes.

## REFERENCES

CAMPBELL, R. B., and MULDAWER, L., 1961, *Phil. Mag.*, **6**, 531.
GAUNT, P., 1960, *Phil. Mag.*, **5**, 1127.
JACOBS, J. S., and BEAN, C. P., 1955, *Phys. Rev.*, **100**, 1060.
STONER, E. C., and WOHLFARTH, E. P., 1948, *Phil. Trans.* A, **240**, 599.
WOHLFARTH, E. P., 1955, *Proc. roy. Soc.* A, **232**, 208.

# The Observation of Dislocations to Accommodate the Misfit between Crystals with Different Lattice Parameters

By J. W. MATTHEWS

Department of Physics, University of the Witwatersrand, Johannesburg

## ABSTRACT

A thin (800 to 1000 Å) foil, composed of a single crystal layer of PbS and a similar layer of PbSe, was prepared by an evaporation technique. The crystals were in parallel orientation and the interface between them was parallel to (001). The foil was examined in a transmission electron microscope and a square grid of dislocations to take up the misfit between the two lattices was observed. The dislocations were of edge type and their Burgers vectors were $\frac{1}{2}a \langle 110 \rangle$.

## § 1. INTRODUCTION

Frank and van der Merwe (1949) have suggested that one crystal grown epitaxially on another strains a little to reduce the misfit between the two lattices and that the remainder of the misfit is accommodated by a grid of dislocations in the interface between the two crystals. One would expect to observe misfit dislocations in electron micrographs of a specimen composed of one single crystal film supported on another if the misfit between the two crystals is less than 5%. When the misfit is larger than 5% the spacing of the misfit dislocations will (if their Burgers vectors are not unusually large) be less than 100 Å and they will be difficult to resolve. This paper describes the misfit dislocations observed between lead selenide (PbSe) and lead sulphide (PbS). The misfit between these lattices, when they are in parallel orientation, is a little over 3%.

## § 2. EXPERIMENTAL DETAILS

PbS was evaporated in vacuum off a tungsten spiral onto the cleavage (i.e. (001)) face of a hot (300°C) rocksalt crystal. The deposition of PbS was immediately followed by the deposition of a similar layer of PbSe. Each layer was approximately 450 Å in thickness. (Under these conditions PbS grows in parallel alignment on rocksalt (Elleman and Wilman 1948) and PbSe grows in parallel alignment on PbS.)

After the specimen had cooled it was lowered, PbSe side upward, into water. The PbSe/PbS foil floated off on the water surface and was caught on a copper specimen grid. It was examined in a transmission electron microscope at magnifications of 40 000 and 80 000 times.

## § 3. Description of the Misfit Dislocations

Misfit dislocations were observed in areas of the specimen near to those that contained moiré fringe patterns formed by interference between the undeviated beam and a beam which had been diffracted once in each of the crystals. This can be seen in figs. 1 and 2†. The areas labelled A contain moiré fringes and the misfit dislocations are visible in the areas labelled B. Two sets of misfit dislocations are visible at B in fig. 1 ; one set is approximately parallel to [110] and the other is approximately parallel to [$\bar{1}$10]. The two sets together form a badly distorted square net. The distortion results from dislocations and small strains in one of the crystals and also from imperfect alignment of one crystal on the other. The misfit to be accommodated by the dislocations is very sensitive to imperfections of this kind.

In some areas of the specimen only one set of dislocations was visible. At B in fig. 2, for example, the dislocations parallel to [$\bar{1}$10] are visible and those parallel to [110] are not. A dislocation with Burgers vector $\mathbf{b}$ is invisible when $\mathbf{g} \cdot \mathbf{b} = 0$ (Hirsch *et al.* 1960) where $\mathbf{g}$ is the reciprocal lattice vector that defines the strongly reflecting plane. The strongly reflecting plane in fig. 2 was (220), so the Burgers vectors of the invisible set of dislocations in this figure lie in the (110) plane. The Burgers vectors also lie in the (001) plane not only because this is the plane of the interface between the crystals but also because it is a slip plane of both PbS and PbSe. The (110) and (001) planes intersect along $\pm[\bar{1}10]$, so the invisible dislocations have Burgers vectors parallel to $\pm[\bar{1}10]$. The Burgers vectors of the invisible set are thus perpendicular to their lines. The visible set of dislocations must, from symmetry considerations, also be of edge type and have Burgers vectors parallel to $\pm[110]$.

The magnitude of the Burgers vectors can be determined from the misfit accommodated by each dislocation. The misfit that each dislocation accommodates can be determined from the spacing of moiré fringes. The fringe pattern at A in fig. 2 was formed by interference between the undeviated beam and a beam which had undergone two reflections of the 220 type. The fringes in this pattern are parallel to the visible dislocations at B in fig. 2 and the spacing of the fringes is half the dislocation spacing. From this it follows that the Burgers vectors of the dislocations are equal to twice the spacing of the (220) planes. The spacing of (220) planes is $\frac{1}{4}a$ [110] so the Burgers vectors of the visible misfit dislocations are $\pm \frac{1}{2}a$ [110]. The Burgers vectors of the invisible ones are $\pm \frac{1}{2}a$ [$\bar{1}$10].

An idea of the proportion of the misfit between the two lattices that is accommodated by the misfit dislocations can be obtained by comparing the observed spacings of the moiré fringes with the calculated ones. (In the calculations of fringe spacings it is common practice to assume

---

† Figures 1 and 2 are shown as plates.

that the lattices do not strain to reduce the misfit between them. One also assumes that atoms do not diffuse from one lattice to the other.) Three essentially different moiré patterns have been examined and the observed and calculated fringe spacings are listed in the table.

| | Reflecting planes in PbSe | Reflecting planes in PbS | Spacing of fringes | |
| --- | --- | --- | --- | --- |
| | | | Observed | Calculated |
| (1) | 200 | $\overline{2}$00 | $100 \cdot 0 \pm 5$ Å | $97 \cdot 4$ Å |
| (2) | 220 | $\overline{2}\overline{2}0$ | $72 \cdot 5 \pm 4$ Å | $68 \cdot 8$ Å |
| (3) | 240 | $\overline{2}\overline{4}0$ | $45 \cdot 2 \pm 2 \cdot 8$ Å | $43 \cdot 6$ Å |

The unit cell dimensions used in the calculations were a $6 \cdot 110$ Å for PbSe (Earley 1950) and $a = 5 \cdot 923$ Å for PbS (Wasserstein 1951). The observed fringe spacings agreed with the calculated ones to within the accuracy of measurement but it is perhaps significant that the observed spacings were all larger than the calculated ones. If the discrepancy between observed and calculated spacings is significant then the lattice parameter of each crystal has changed by $0 \cdot 06\%$ to reduce the misfit. The reduction of misfit is $4\%$ ; the remaining $96\%$ is accommodated by the misfit dislocations.

It is important to notice that the misfit dislocations described here cannot be interpreted as moiré patterns. Moiré patterns with the same orientation and spacing as the misfit dislocations could only be formed by interference between the undeviated beam and a beam which has experienced two reflections of the 110 type. 110 reflections do not occur in crystals with the NaCl structure.

### REFERENCES

EARLEY, J. W., 1950, *Amer. Min.*, **35**, 338.
ELLEMAN, A. J., and WILMAN, H., 1948, *Proc. phys. Soc., Lond.*, **61**, 164.
FRANK, F. C., and VAN DER MERWE, J. H., 1949, *Proc. roy. Soc.* A, **198**, 216.
HIRSCH, P. B., HOWIE, A., and WHELAN, M. J., 1960, *Phil. Trans.* A, **252, 499.**
WASSERSTEIN, B., 1951, *Amer. Min.*, **35, 102.**

# An Experimental Determination of the Electrical Resistivity of Stacking Faults and Lattice Vacancies in Gold

By R. M. J. COTTERILL

Crystallographic Laboratory, Cavendish Laboratory, Cambridge,
England

## ABSTRACT

The change in the electrical resistivity of gold foils due to the introduction of (a) stacking faults, and (b) lattice vacancies, is correlated with concentration counts obtained by transmission electron microscopy. The resistivity of stacking faults is found to be $\rho_{SF} = [1 \cdot 8 \pm 0 \cdot 3] \times 10^{-13} \beta \,\Omega\, cm^2$ for a stacking-fault density equal to $\beta \, cm^{-1}$. A lower limit for the resistivity of vacancies is $\rho_V = [2 \cdot 4 \pm 0 \cdot 4] \times 10^{-6} \,\Omega\, cm/atomic \,\%$ vacancies.

## § 1. INTRODUCTION

CALCULATIONS of stacking-fault resistivity, $\rho_{SF}$, have been reported by Klemens (1953, 1956), Seeger (1956), Blatt *et al.* (1956), Tweedale (reported by Ziman 1956), and more recently by Howie (1960). The predicted values show mutual disagreement by factors as large as $10^3$, and Howie (1960) makes a critical survey of the previous attempts, offering explanations of their discrepancies. He has used Pippard's model of the Fermi surface in copper (Pippard 1957) in a calculation of the scattering of electrons by the faults. This scattering is shown to be due to a phase change in the diffraction by the crystal planes which do not lie parallel to the fault. Using a simple argument, Howie finds that $\rho_{SF} \sim 1 \times 10^{-12} \beta \,\Omega\, cm^2$, where $\beta \, cm^{-1}$ is the total stacking-fault density on all planes, and he confirms the order of magnitude with a more complete wave-matching calculation. The latter yields a value $\rho_{SF} \sim 2 \cdot 5 \times 10^{-13} \beta \,\Omega\, cm^2$. No direct experimental determination of $\rho_{SF}$ has been reported.

The resistivity of lattice vacancies can be calculated by using a phase-shift analysis to obtain the scattering cross section for electron–vacancy collisions. Jongenburger (1953) finds for copper, $\rho_V = 1 \cdot 3 \times 10^{-6} \,\Omega\, cm/at. \,\%$ and for silver and gold $\rho_V = 1 \cdot 5 \times 10^{-6} \,\Omega\, cm/at. \,\%$. Abélès (1953), Blatt (1955), and Overhauser and Gorman (1956) have obtained values very similar to the above. Dexter (1952) has calculated that for copper $\rho_V = 0 \cdot 4 \times 10^{-6} \,\Omega\, cm/at. \,\%$ and later $\rho_V = 0 \cdot 7 \times 10^{-6} \,\Omega\, cm/at. \,\%$ (Dexter 1956). The only direct determination of $\rho_V$ reported is that of Simmons and Balluffi (1960) who find for aluminium $\rho_V = 3 \times 10^{-6} \,\Omega\, cm/at. \,\%$. Simmons and Balluffi have recently completed similar experiments for gold (private communication), and their preliminary analysis of the results yields a value $\rho_V = [1 \cdot 8 \pm 0 \cdot 6] \times 10^{-6} \,\Omega\, cm/at. \,\%$.

If a metal is rapidly cooled from a temperature close to its melting point, a large number of vacancies may be trapped in the lattice and the concentration at room temperature will then be greatly in excess of the equilibrium value. The annealing out of the excess vacancies proceeds at a rate which is dependent on temperature, and on $E_M$, the activation energy for vacancy migration (e.g. Cottrell 1958). The value of $E_M$ for gold is such that the annealing at room temperature takes several hundred hours, and this has been verified by the electrical resistivity experiments of Bauerle and Koehler (1957). These workers have annealed quenched gold wires at various temperatures above 0°C, and for all quenches from above about 850°C find that the resistivity falls asymptotically to about one-tenth of the quenched-in value. The results have been interpreted by Kimura *et al.* (1959), using a model in which those vacancies which are not lost at grain boundaries and dislocations, form clusters, each containing several thousand vacancies. Silcox and Hirsch (1959 a) confirmed the existence of such clusters in gold foils quenched from 960°C and subsequently annealed at 100°C. Observation of the foils, by transmission electron microscopy, revealed defects in the form of tetrahedra of stacking fault. Correlation with diffraction data showed that the faces of the tetrahedra were on {111} slip planes, and Silcox and Hirsch inferred that they were formed by the condensation of vacancies. The tetrahedra were shown to have stair-rod dislocations along the six ⟨110⟩ edges.

Using the results of Silcox and Hirsch in conjunction with the numerical values of Bauerle and Koehler, it is possible to give a rough estimate of the resistive effect of the vacancies at the various stages of annealing. Quenching is thought to produce predominantly single vacancies (Koehler *et al.* 1957), and the resistivity per vacancy is at its maximum when they are thus dispersed in the lattice. Annealing then causes aggregation and the defect tetrahedra are formed. The faces of the tetrahedra become the primary obstacles to the conduction electrons, and the resistivity per vacancy falls to a minimum. Howie (1960) has shown that it is reasonable to expect that the contribution to the resistivity made by the stair-rod dislocations of any one tetrahedron will be small compared with that of the associated stacking faults, because the stair-rod dislocations have the small Burgers vector $\frac{1}{6}\langle 110 \rangle$ and are arranged so that their long-range stress fields cancel.

If resistivity measurements are made on quenched and annealed foils, these can be thinned down and observed by electron microscopy. A direct determination of tetrahedron concentration and size distribution is then possible. From these quantities the stacking-fault density can be found, and the resistivity of stacking faults calculated. Moreover, the concentration of vacancies which produces a given concentration of stacking faults can be calculated. If it is assumed that negligible clustering occurs during quenching, and that only a small fraction of the vacancies is lost during the annealing, this value of the vacancy concentration can be taken in conjunction with the quenched-in resistivity, and the resistivity of

vacancies computed. This paper reports the results of experiments of this nature designed to determine $\rho_{SF}$ and $\rho_V$ from resistivity measurements and electron microscope observations on the same specimens. No direct correlation of this type has been reported previously.

## § 2. EXPERIMENTAL TECHNIQUES

The material used was 99·9995% pure polycrystalline gold foil (principal impurities: Ag 0·0002%, Fe 0·0001%, Si 0·0001%), $7·5 \times 10^{-3}$ cm thick and 0·5 cm wide. The specimen and a dummy, annealed at 500°C for five hours, were mounted in a quenching jig. The specimen was heated by an alternating current of about 50 amp, and the temperature of the gauge length, the central 5 cm of a 15 cm length, was measured with an optical pyrometer. The exponential dependence of vacancy concentration on the temperature made temperature uniformity along the gauge length of great importance, and this was achieved by tapering the specimen over 4·5 cm at each end. Uniformity of $\pm 1\%$ was obtained, and the degree of taper was itself a function of the quenching temperature. The quenching jig was pivoted at one end and suspended above a tank of iced brine, the latter being placed inside a draught-proof box fitted with a viewing window for the temperature measurement. The specimen was held at the quenching temperature for five minutes, and quenched by remote control. It entered the liquid with its axis parallel to the surface to ensure simultaneous quenching over the entire gauge length, and edge on to minimize mechanical shock. The heating current was switched off within two seconds after entry.

The quenching speed was determined by using a cathode-ray oscilloscope to measure the rate of change of specimen resistance. A quench from 1000°C took 0·02 sec, and in general it was found that the temperature decreased according to the relation $T = T_q - \alpha t$ where $\alpha \simeq 5 \times 10^4$ °C sec$^{-1}$.

The resistance measurements were made at 78°K, at which temperature the residual resistivity was a conveniently large fraction of the total resistivity. A series potentiometer circuit was used and the specimen was compared with the dummy in order to correct for long-term variations in the temperature of the liquid nitrogen bath. Short-period temperature fluctuations were found to cause instability by acting differentially on the specimen and dummy, and they were eliminated by suspending the jig in a can filled with argon at a pressure of about 20 cm Hg. This thermal damping device is illustrated in fig. 1†. Difficulties arising from short-period temperature fluctuations were not reported by Bauerle and Koehler (1957), who worked with wires. It is believed that foils are more susceptible to temperature fluctuation owing to their high ratio of surface area to resistance. This was confirmed by a control experiment in which the resistance fluctuations of a foil and a wire were compared directly. The measuring current of about 1 amp was obtained from a 400 amp-hour

---

† Figures 2, 4 and 6 are shown as plates.

capacity accumulator, and was steady to 1 in $10^5$. It was standardized by the inclusion of a standard $10^{-3}$ ohm resistance in the potentiometer circuit. All potential differences were measured with a Cambridge Instruments Company precision vernier potentiometer which could detect $5 \times 10^{-8}$ volts.

Fig. 1
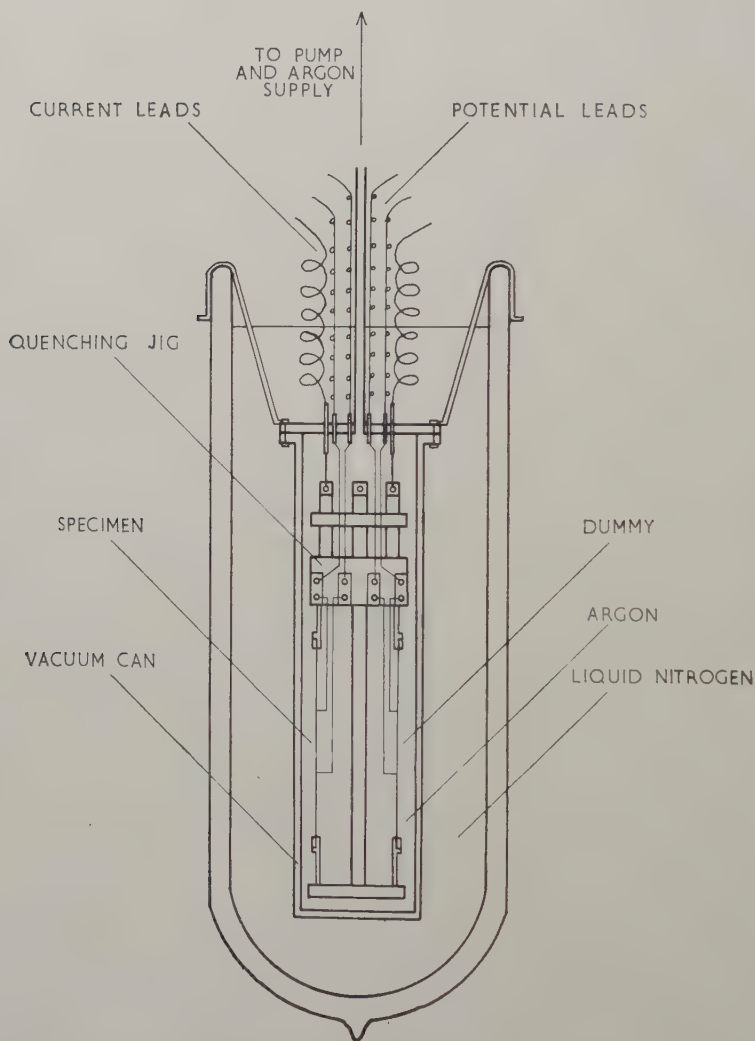


Low-temperature bath and thermal damping device.

Each specimen was first annealed at the quenching temperature until its resistance became constant. The time taken for this was about two hours for the range of quenching temperatures used (850°c–1000°c). The

specimen was then quenched and the resistivity change determined. The specimen was at room temperature for less than 15 min. A water bath was used to anneal the specimen at 100°C until its net resistivity change had fallen to the asymptotic value. The time taken for the latter process varied with quenching temperature, being about 15 min for $T_q = 1000$°C and about 90 min for $T_q = 850$°C. The dummy remained in the jig throughout, and its resistivity was unchanged by the various processes because at no time did its temperature approach that at which it had been annealed.

The specimen was removed from the jig and electropolished in a cyanide bath at 60°C. Small pieces were cut from it and examined in a Siemens Elmiskop I electron microscope operating at 100 kv. In all cases, uniform concentrations of defect tetrahedra were observed (see table). Those areas showing slip traces left by moving dislocations were photographed (see fig. 2). The slip traces allow the foil thickness to be determined, if it is assumed that the slip is on {111}, and if the orientation of the foil normal is determined by selected area diffraction (Whelan 1957). Mean tetrahedron concentrations and sizes were found from photographic enlargements, and the concentrations of stacking faults were calculated.

## § 3. Experimental Results

The values of quenched-in resistivity, $\Delta\rho_q$, and the resistivity remaining after fully annealing at 100°C, $\Delta\rho_a$, are given in the table. Also given are the concentration of tetrahedra, $C_T$, and the root mean square tetrahedron size, $L_{\text{r.m.s.}}$ (where $L_{\text{r.m.s.}}$ is the length of each of the $\langle 110 \rangle$ edges), the corresponding density of stacking faults, $\beta$ (where $\beta = \sqrt{3L^2_{\text{r.m.s.}}C_T}$), and the concentration of vacancies, $C_V$ (where $C_V = \beta\alpha/4\sqrt{3}$, and $\alpha$ is the lattice parameter). In the final two columns the resistivity of stacking faults, $\rho_{\text{SF}}$ ($=\Delta\rho_a/\beta$), and the resistivity of vacancies, $\rho_V$ ($=\Delta\rho_q/C_V$), are given. In all cases the indicated errors are standard deviations. The weighted mean values were:

$$\rho_{\text{SF}} = [1 \cdot 8 \pm 0 \cdot 3] \times 10^{-13} \beta \ \Omega \ \text{cm}^2,$$

$$\rho_V = [2 \cdot 4 \pm 0 \cdot 4] \times 10^{-6} \ \Omega \ \text{cm per } 1\% \text{ atomic concentration of vacancies.}$$

As the specimens were polycrystalline, $\rho_{\text{SF}}$ is an average value over all orientations. The variation of $C_T$ and $L_{\text{r.m.s.}}$ with quenching temperature is indicated in fig. 3. It may be noted that although increasing the quenching temperature produces a higher concentration of smaller tetrahedra, the value of $\rho_{\text{SF}}$ remains constant within the experimental limits. Because the resistivity due to the stair-rod dislocations is proportional to $L_{\text{r.m.s.}}$ whereas that due to the stacking faults is proportional to $L^2_{\text{r.m.s.}}$, this result suggests that the contribution of the stair-rods can be ignored for the range of tetrahedron sizes observed.

Five quenching temperatures in the range 850°C–1000°C were used. The lower limit of this range was set by the following considerations. Bauerle and Koehler (1957) have found that for quenched gold, 800°C

| $T_a$ °C | $\Delta\rho_q$ $\times 10^{-8}$ Ω cm | $\Delta\rho_a$ $\times 10^{-9}$ Ω cm | $C_T$ $\times 10^{15}$ cm$^{-3}$ | $L_{\mathrm{r.m.s.}}$ Å | $\beta$ $\times 10^4$ cm$^{-1}$ | $C_V$ $\times 10^{-4}$ | $\rho_{\mathrm{SF}}$ $\times 10^{-13}\beta$ Ω cm$^2$ | $\rho_V$ $\times 10^{-6}$ Ω cm/At. % |
|---|---|---|---|---|---|---|---|---|
| 855 | 2·25 | 2·46±0·30 | 0·29±0·09 | 525±77 | 1·4±0·5 | 0·8±0·3 | 1·8±0·7 | 2·9±0·9 |
| 890 | 2·57 | 3·35±0·35 | 0·63±0·20 | 440±33 | 2·1±0·7 | 1·2±0·4 | 1·6±0·6 | 2·1±0·7 |
| 920 | 2·43 | 3·01±0·30 | 0·86±0·28 | 348±29 | 1·8±0·6 | 1·1±0·4 | 1·7±0·6 | 2·2±0·7 |
| 960 | 3·01 | 4·69±0·40 | 0·82±0·34 | 439±55 | 2·7±1·2 | 1·6±0·7 | 1·7±0·8 | 1·9±0·9 |
| 1000 | 3·53 | 5·75±0·45 | 1·49±0·68 | 271±29 | 1·9±0·9 | 1·1±0·5 | 3·0±1·4 | 3·3±1·6 |

is a critical temperature.  Below this temperature the annealing kinetics are changed.  In the present experiment, for temperatures below 800°C, quenching and subsequent annealing at 100°C produced no tetrahedra.

Fig. 3
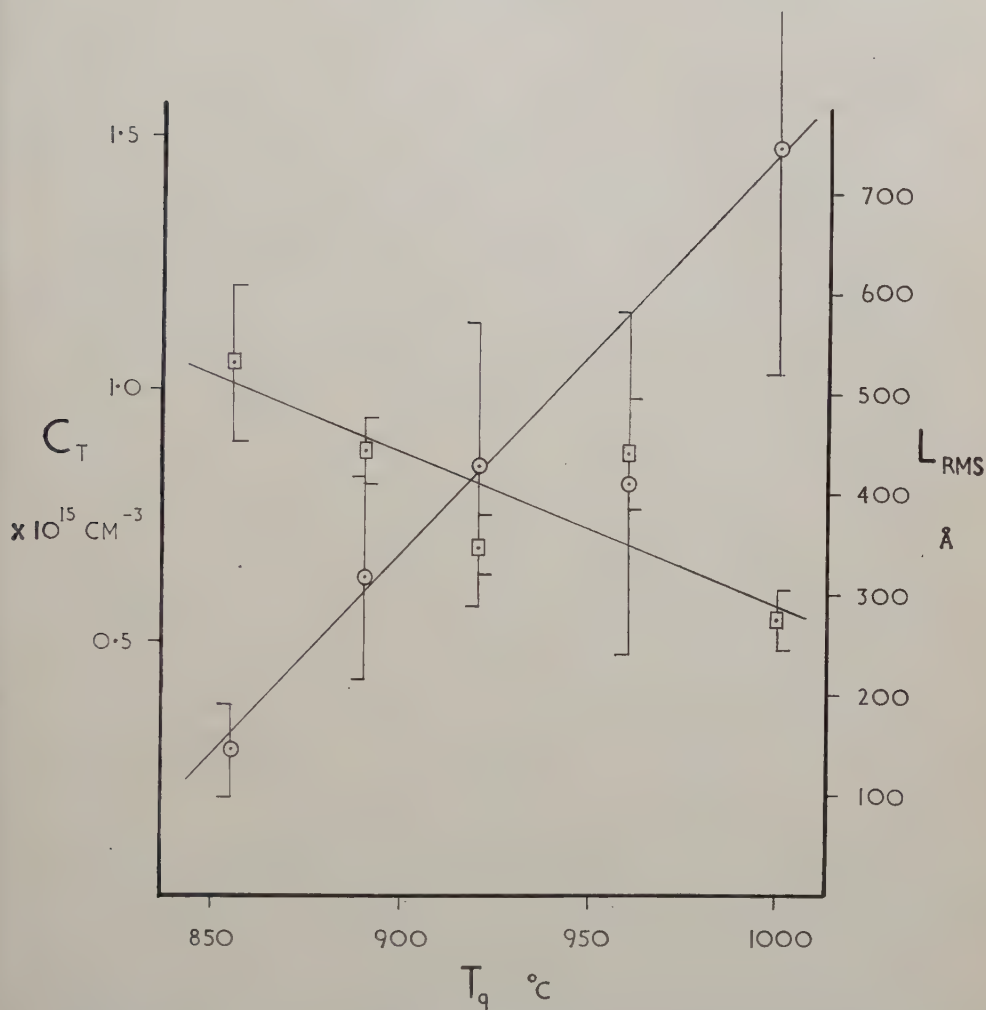


Variation of $C_T$(⊙) and $L_{\text{r.m.s.}}$(⊡) with quenching temperature, $T_q$.

Instead high concentrations ($\sim 10^{16}\,\text{cm}^{-3}$) of black spots were observed (see fig. 4 (a)).  These spots, which had an average diameter of about 25 Å, are similar to those observed in irradiated metals (Silcox and Hirsch 1959 b, Barnes and Mazey 1960).  The resistivity due to the black spots was determined in a separate experiment (reported briefly in § 4.2 of this paper).  A knowledge of this value is useful in making certain corrections

to $\rho_V$, as described in § 4.2. A specimen quenched from 800°C and annealed at 100°C gave a mixture of tetrahedra and black spots (see fig. 4 (*b*)), a result which supports the view that there is a transition around this temperature. Figure 4 (*c*) is included for comparison with figs. 4 (*a*) and (*b*). It shows a typical area of a specimen quenched from above 800°C and annealed at 100°C.

## § 4. DISCUSSION

### 4.1. *The Resistivity of Stacking Faults*

The value obtained for the stacking-fault resistivity is not subject to any error arising from vacancy loss during quenching or annealing. The resistivity measurements were made after completion of annealing, when all vacancies were assumed either to have joined the clusters in forming the defect tetrahedra, or to have been lost at grain boundaries, at dislocations and at the surface of the specimen. It is reasonable to assume that none of the tetrahedra disappears in the interval between the

Fig. 5
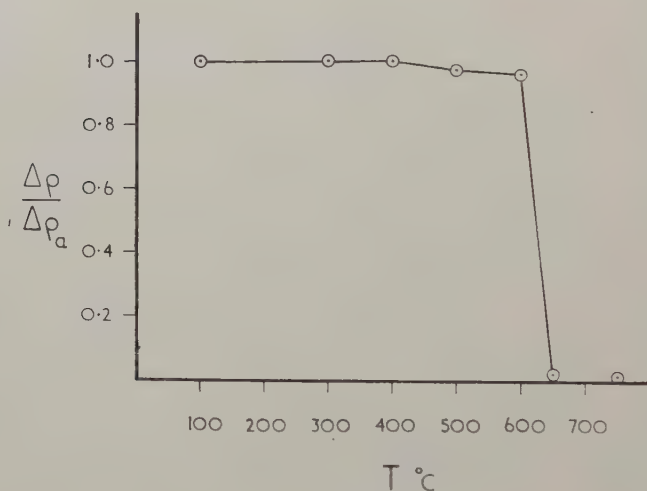


The temperature dependence of residual resistivity in a specimen quenched from 1000°C, fully annealed at 100°C, and then annealed for one hour at the temperatures indicated.

resistivity measurements and examination in the electron microscope, because these defects are extremely stable. In fact, a subsidiary isochronal annealing experiment (see fig. 5) showed that the resistivity due to the tetrahedra does not anneal out until a temperature of between 600°C and 650°C is reached (i.e. a temperature about 500°C above the maximum temperature of the specimen during the measurements). This result is

in agreement with that of Silcox (1961) who has carried out an electron microscope examination of the annealing out of the tetrahedra. The absence of any appreciable resistivity drop below 600°c also shows that the measured resistivity is due either entirely to the defect tetrahedra, or to the tetrahedra and other defects which are not observed with the electron microscope and which anneal out at the same temperature. The annealing curve shown in fig. 5 is quite different from that obtained by Meshii and Kauffman (1960) for gold wires quenched from the same temperature at a slightly lower quenching speed. Discussion of this discrepancy is left to a later paper.

The method used for taking samples of the specimen for concentration counts might appear open to question. The greater part of each specimen is lost during electropolishing, only a small fraction being available for inspection in the electron microscope. Such a process would introduce large errors if the defect size and concentration were not uniform. As is indicated by the relevant standard deviations shown in the table, however, these quantities did not show excessive variations. It must be noted, however, that all quenched specimens must contain the intrinsic non-uniformity that arises from denudation at grain boundaries, dislocations and the specimen surface. Most of the vacancies lying within a certain distance of these three types of sink will be lost during the quenching. No correction is required for denudation around dislocations, because the observed dislocation density was negligibly small. The denuded zone at a grain boundary is about $5 \times 10^{-5}$ cm wide, and since the mean grain size was about $10^{-2}$ cm (measured optically) the correction due to this factor was also negligible. Finally, it is noted that the correction for denudation due to loss of vacancies at the specimen surface is quite small for the specimen thickness employed in the experiments (see Cottrell 1958). The experimental value of $\rho_{SF}$ ($0.18 \times 10^{-12} \beta \, \Omega \, cm^2$) supports the theoretical value of Howie ($[0.2 - 1.0] \times 10^{-12} \beta \, \Omega \, cm^2$).

## 4.2. *The Resistivity of Vacancies*

The calculation of the resistivity of vacancies is valid only if the mechanism of quenching and annealing is as described in § 1. According to this mechanism quenching produces predominantly single vacancies and possibly some vacancy clusters. The defect tetrahedra are formed only during the subsequent annealing. A critical test of this mechanism would be afforded by an experiment in which a quenched specimen is thinned and observed in the electron microscope without appreciable annealing at or above room temperature. Such an experiment is not possible if the cyanide polishing bath is used, since this operates at 60°c. For this reason an alternative bath was developed. Concentrated hydrochloric acid was found to give a reasonable polish at $-15°c$ using a stainless-steel cathode and an open circuit voltage of $14 \pm 2$ volts d.c. across the cell.

A specimen was annealed for four hours at 930°c and quenched from that temperature into brine at 0°c. It was removed from the quenching

jig, cut into two pieces and placed in liquid nitrogen within 30 sec. Immediately prior to polishing, one-half of the specimen was removed from the nitrogen and transferred to the polishing cell within a further 30 sec. The specimen, which therefore underwent less than one minute annealing at room temperature, was thinned by electropolishing and examined in the electron microscope. A concentration of about $5 \times 10^{14}$ cm$^{-3}$ of the black spot defects was observed, but no tetrahedra were seen (see fig. 6 $(a)$). The defects appeared to have the same shape and size as those observed in the specimens quenched from 750 °C (see fig. 4 $(a)$), but the concentration was lower by a factor of about 20. The other half of the specimen was annealed for one hour at 100 °C, thinned and examined. It was found to contain a concentration of tetrahedra which was approximately equal to the concentration of black spots in the unannealed half (see fig. 6 $(b)$). A slowly cooled specimen showed neither tetrahedra nor black spot defects.

This experiment shows that quenching does not produce tetrahedra. These are formed only during the subsequent annealing. It also shows that the black spot defects are formed either during quenching or during the first minute of annealing at room temperature. The approximate equality of the concentration of black spot defects in the unannealed specimen and tetrahedra in the annealed specimen would be consistent with an annealing process in which the former are an intermediate stage in the clustering, but this may be fortuitous.

Finally it must be noted that the results of the above experiment suggest that the black spot defects were probably present during the measurement of $\Delta\rho_q$, and that their presence could affect the value of $\rho_V$. To obtain an estimate of the resistivity due to the black spot defects, we note that the resistance measurements and electron microscope observations on foils quenched from 750 °C and annealed at 100 °C (see fig. 4 $(a)$) showed that a concentration of about $10^{16}$ cm$^{-3}$ of defects of similar appearance produces a residual resistivity of about $6 \times 10^{-9} \,\Omega$ cm. Assuming the defects to be the same in both cases, the lower concentration of the spots ($\sim 5 \times 10^{14}$ cm$^{-3}$) present in the specimens during the determination of $\Delta\rho_q$ would therefore have contributed $\sim 3 \times 10^{-10} \,\Omega$ cm to the resistivity. This is only about 1% of the value of $\Delta\rho_q$ given in the table for quenching from 1000 °C. The resistivity due to the black spot defects therefore appears to be very small. The question remains whether an appreciable fraction of the quenched-in vacancies reside in the black spot defects during the measurement of $\Delta\rho_q$. The physical nature of the defects is at present obscure. The spots have a diameter $\sim 25$ Å. It is difficult to imagine that the defects contain more vacancies than a spherical cavity of about this size, i.e. more than $\sim 400$ vacancies. Since the density of the spots is about the same as that of the defect tetrahedra formed on subsequent annealing, and since each tetrahedron contains between 4000 and 8000 vacancies (depending on $T_q$), it is thought that not more than between 5% and 10% of the vacancies reside in the spot defects during the measurement

of $\Delta\rho_q$. The resulting error would cause the value of $\rho_V$ to be low by not more than 10%. Because any other non-observable clusters will in general lower $\Delta\rho_q$, the experimental value of $\rho_V$ ($[2 \cdot 4 \pm 0 \cdot 4] \times 10^{-6}\,\Omega\,\text{cm/at. }\%$) is a lower limit. It is however consistent with that of Simmons and Balluffi ($[1 \cdot 8 \pm 0 \cdot 6] \times 10^{-6}\,\Omega\,\text{cm/at. }\%$). It is about 60% higher than the theoretical estimates of Jongenburger, Abélès, Blatt, and Overhauser and Gorman, listed in § 1.

## § 5. Conclusion

The electrical resistivity of stacking faults in gold can be obtained by correlation of resistance measurements and electron microscope observations made on the same specimen. Experiments of this type yield a value $\rho_{\text{SF}} = [1 \cdot 8 \pm 0 \cdot 3] \times 10^{-13}\,\beta\,\Omega\,\text{cm}^2$, for a stacking-fault density $\beta\,\text{cm}^{-1}$. The possible corrections to this value are quite small and the determination appears to be absolute. Similar determinations should be possible for all metals in which it is possible to produce high and uniform concentrations of defect tetrahedra.

The electrical resistivity of lattice vacancies can be found from the experiments but the result is subject to errors due to uncertainty in knowledge of the mechanism of annealing. The experimental value $\rho_V = [2 \cdot 4 \pm 0 \cdot 4] \times 10^{-6}\,\Omega\,\text{cm/at. }\%$ is a lower limit.

## References

Abélès, F., 1953, *C.R. Acad. Sci., Paris*, **237**, 796.
Barnes, R. S., and Mazey, D. J., 1960, *Phil. Mag.*, **5**, 1247.
Bauerle, J. E., and Koehler, J. S., 1957, *Phys. Rev.*, **107**, 1493.
Blatt, F. J., 1955, *Phys. Rev.*, **99**, 1708.
Blatt, F. J., Ham, F. S., and Koehler, J. S., 1956, *Bull. Amer. phys. Soc.*, **1**, 114.
Cottrell, A. H., 1958, *Inst. Met.*, Monograph No. 23, p. 10.
Dexter, D. L., 1952, *Phys. Rev.*, **87**, 768; 1956, *Ibid.*, **103**, 107.
Howie, A., 1960, *Phil. Mag.*, **5**, 251.
Jongenburger, P., 1953, *Appl. sci. Res., Hague*, B, **3**, 237.

KIMURA, H., MADDIN, R., and KUHLMANN-WILSDORF, D., 1959, *Acta Met.*, **7,** 145.

KLEMENS, P. G., 1953, *Aust. J. Phys.*, **6,** 122;  1956, *Canad. J. Phys.*, **34,** 1212.

KOEHLER, J. S., SEITZ, F., and BAUERLE, J. E., 1957, *Phys. Rev.*, **107,** 1499.

MESHII, M., and KAUFFMAN, J. W., 1960, *Phil. Mag.*, **5,** 687.

OVERHAUSER, A. W., and GORMAN, R. L., 1956, *Phys. Rev.*, **102,** 676.

PIPPARD, A. B., 1957, *Phil. Trans.* A, **250,** 325.

SEEGER, A., 1956, *Canad. J. Phys.*, **34,** 1219.

SILCOX, J., and HIRSCH, P. B., 1959 a, *Phil. Mag.*, **4,** 72;  1959 b, *Ibid.*, **4,** 1356.

SILCOX, J., 1961, Ph.D. Dissertation, University of Cambridge.

SIMMONS, R. O., and BALLUFFI, R. W., 1960, *Phys. Rev.*, **119,** 600.

WHELAN, M. J., 1957, Ph.D. Dissertation, University of Cambridge.

ZIMAN, J. M., 1956, *Canad. J. Phys.*, **34,** Discussion following paper of Seeger 1219.

# The Growth of Snow Crystals at Low Supersaturations

By T. Kobayashi†

Department of Cloud Physics, Imperial College, London

## Abstract

The result of experiments in which ice crystals are grown from the vapour at supersaturations of only a few per cent show that the $c/a$ ratio tends towards limiting values of 1·4 for prisms and 0·8 for plates. Thus the habit of snow crystals is now clearly delineated with respect to both temperature and supersaturation or flux of vapour. The basic habit, as determined by the relative growth rates along the $c$ and $a$ axes, is controlled by the temperature but the secondary features of growth are governed by supersaturation as follows; in the plate regime, increasing supersaturation causes transitions from very thick plate→thick plate→sector plate→dendrite and, in the prism regime, the development is from short solid prism →longer hollow prism→ needle. There now appears to be no basis for believing that the basic crystal habit is modified by changing the diffusivity of water vapour into the inert carrier gas.

## § 1. Introduction

EXPERIMENTS carried out by several different workers, for example, Nakaya (1954), Shaw and Mason (1955), Kobayashi (1957), Hallett and Mason (1958) have all demonstrated that the *basic* habit of snow crystals growing from the vapour in air supersaturated with respect to liquid water is determined by the temperature of the air, and not by the supersaturation or excess vapour density as proposed by Marshall and Langleben (1954). Thus the crystals grow either by preferential growth along the $c$ axis as prismatic columns or as hexagonal plates (preferential growth along the $a$ axis) in the sharply defined temperature ranges shown in fig. 6, a change of only 1°C being sufficient to induce a change from prism to plate-like development. On the other hand, secondary growth features, such as dendritic and sector extensions of hexagonal plates and needle-like extensions of prisms, develop only if the air is supersaturated relative to liquid water.

If the basic habit were determined by the flux of water vapour towards the growing crystal, that is by $D\Delta\rho$, where $D$ is the diffusion coefficient of water vapour and $\Delta\rho$ the excess of the ambient vapour density over that in equilibrium with the crystal surface, it might be expected to change if the crystals were grown in other gases, or in air at reduced pressure. And indeed, Isono *et al.* (1957) and Isono (1958) reported that, when the crystals were grown in hydrogen and in air at low pressure, they observed

† On leave from Institute of Low Temperature Science, Hokkaido University, Sapporo, Japan.

nearly isometric growth ($c/a \approx 1$) throughout the temperature range $-7°$C to $-16°$C, a region in which plates are formed in air at normal pressure. These authors claim that the environment was kept saturated relative to liquid water, (in view of the present writer's experience with a similar apparatus this seems doubtful), and attribute the observed habit changes to the more rapid diffusion of vapour in the hydrogen and low-pressure atmospheres. On the other hand, van den Heuvel and Mason (1959) found that variation of habit with temperature, involving plates, needles, hollow prisms and dendrites, was unaffected by reducing the air pressure to 20 mm Hg or by replacing the air by carbon dioxide, hydrogen or helium ; only the *growth rate* of the crystals was affected as was to be anticipated because of differences in the diffusion coefficients and thermal conductivities of the various gases.

The present author (Kobayashi 1958) has also investigated the effect of lowering the air pressure on the growth habit. At pressures above 300 mm Hg, the normal variation of crystal habit with temperature was observed ; at pressures between 300 and 70 mm Hg hollow prisms were observed in the temperature range $-10°$C to $-22°$C but, below 70 mm Hg, these gave way to solid prisms. These latter crystals grew very slowly suggesting that the increased value of $D$ was more than offset by a reduction in $\Delta\rho$. Kobayashi concluded that his experimental arrangement was such that a large reduction in the air pressure caused the supply of water vapour to the crystals to be much reduced—something which did not occur in the experiments of van den Heuvel and Mason. It therefore seems likely that the latter were correct in stating that the basic crystal habit is not modified by the nature of pressure of the carrier gas *per se*, but some modification may occur if the crystals grow slowly under very low supersaturations of only a few per cent relative to ice.

Production and measurement of such small supersaturations could not be achieved in the above-mentioned experiments. Such an attempt was made by Kobayashi (1960) using a convective mixing chamber of the Nakaya type, the supersaturation being measured by sucking a known volume (about 2 litres) of air from the chamber through dried methanol and determining the total water content by titration with Karl Fischer reagent.

Although under small supersaturations short solid columns and very thick plates occurred at temperatures between $-8°$C and $-23°$C, the measurements were not sufficiently accurate to allow of the crystal habit being clearly delineated with respect to temperature and supersaturation. A new and more successful attempt will now be described.

## § 2. Experimental Technique

The apparatus is shown in fig. 1†. The working principle is to mix two air streams of different temperatures, each saturated with respect to

---

† Figure 2 is shown as a plate.

ice, to produce a supersaturated mixture at an intermediate temperature. The ice crystals are grown on fine fibres suspended in the mixing air currents, the temperature of which is measured by a thermistor and the humidity by a dew-point hygrometer.

Fig. 1
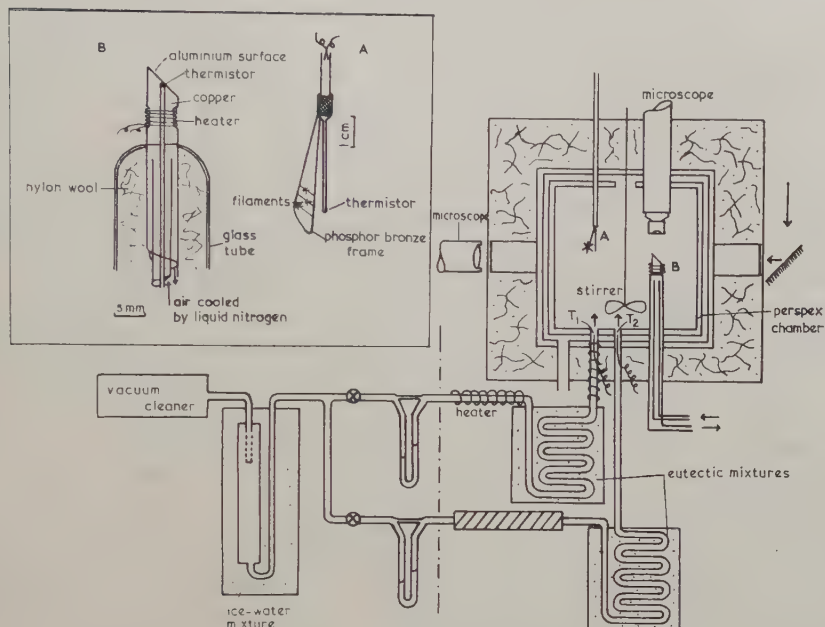


The experimental chamber, 3 litres in capacity with well-insulated double walls made of ' Perspex ', is enclosed in a refrigerator whose temperature can be controlled down to $-25°$c. The air supply is sucked by a vacuum cleaner through a heat exchanger at $0°$c which removes both heat and moisture, divides into two separate streams, which then pass through cooling coils immersed in eutectic mixtures of ice and salt or in kerosene chilled with dry ice, where they attain the required temperatures. Additional temperature control is provided by an electrical heater wound on one of these cooling coils. The temperatures of the two ice-saturated air streams, the flow of which may be independently controlled up to rates of 6 litres/min, are measured as they enter the experimental chamber by the thermocouples $T_1$ and $T_2$. They are now intimately mixed by a fan and the temperature of the mixture measured by a fine thermistor placed about 3 mm from the crystals which grow on fibres stretched across a light phosphor-bronze frame.

The mirror-like dew-forming surface of the hygrometer, produced by evaporating aluminium *in vacuo* onto a small copper thimble, is cooled by pumping air chilled by liquid nitrogen through the hollow supporting tube. The temperature of the dew-forming surface is controlled by varying the pumping rate and the current through a small heating coil wound

onto the thimble and is measured by a fine thermistor attached immediately beneath the surface.  To measure the dew point the rate of supply of cold air to the thimble is adjusted until a dew deposit, viewed by oblique illumination through a microscope, just begins to form. The accuracy of the hygrometer was checked from time to time by noting its reading when ice crystals on the fibre underwent a transition between growth and evaporation.  The hygrometer worked satisfactorily at temperatures down to $-20°c$, the error in the measurement of relative humidity not exceeding 3%.  But, at lower temperatures, it was more difficult to use because some ice crystals usually appeared before supercooled water droplets on the thimble surface.

Working at supersaturations of only a few per cent, it was necessary to continue the experiment for several hours in order to grow crystals large enough for accurate measurement.  It proved very difficult to keep conditions in the chamber constant for such long periods for two reasons. Because the refrigerator had to be stopped for short periods at regular intervals in order to take photographs without vibration, the air in the chamber usually warmed up by 1° or 2°c during a run of several hours. And, if frost formed on the walls of the chamber (and it was not easy to prevent this entirely), transport of vapour to the frost-covered walls caused the supersaturation to decrease very slowly during the course of an experiment.

Crystals were grown on rabbit hairs, filaments of ' Durofix ' and quartz fibres. Although nucleation occurred most readily on rabbit hairs and was very difficult on quartz fibres, especially at low supersaturations, the subsequent growth of the crystals did not appear to be influenced by the nature of the support.  At temperatures above $-10°c$ crystals were reluctant to form on any of the filaments although occasional ice germs originating from the cooling coils or from the frost-covered chamber walls were caught by the fibres.  Below $-10°c$, nucleation could be facilitated by increasing the flow rate of the warmer air stream, and therefore the supersaturation, for about half a minute, and above $-10°c$, by exposing the filament to a smoke of silver iodide.

The growing crystals were observed and photographed through a microscope and camera placed inside the refrigerator and directed at a small window in the experimental chamber.  Photographs were taken at regular intervals ranging from 1 to 10 min according to the growth rate, changes in the linear dimensions of the crystals being determined from measurements on successive negatives greatly enlarged.

## § 3. Experimental Results

In the temperature range $-10°c$ to $-20°c$ it is fairly easy to control the experimental conditions and to obtain an appropriate density of crystals on the filaments.  If the air was supersaturated relative to liquid water the crystals grew as dendrites as shown in fig. 2 (*a*) but as the

supersaturation decreased these developed into sector plates and became progressively thicker as shown in fig. 2 $(a)$–$(e)$.  If new germs appeared

Fig. 3
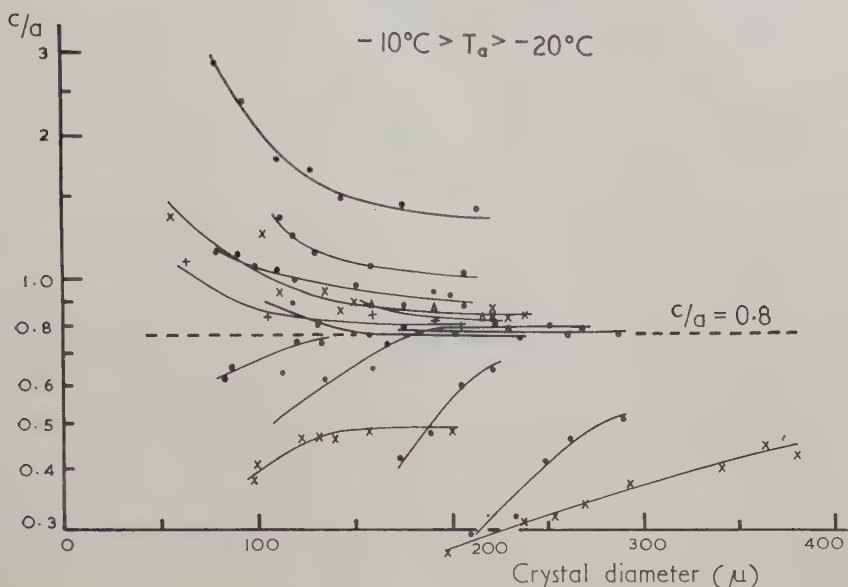


Fig. 4
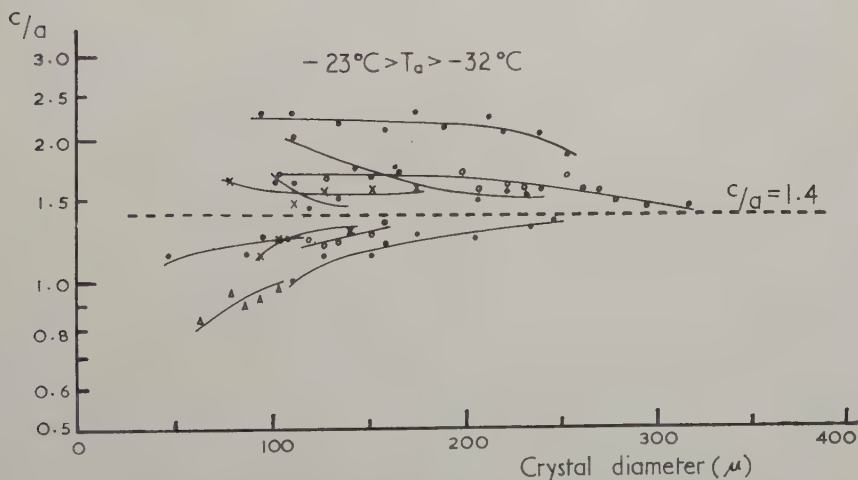


on the filaments when the air approached ice saturation, these grew as small compact prisms (see fig. 2$(c)$–$(e)$) similar to those observed in the low-pressure air experiment described in the Introduction.  Careful measurement of these crystals, growing at ice-supersaturations of less
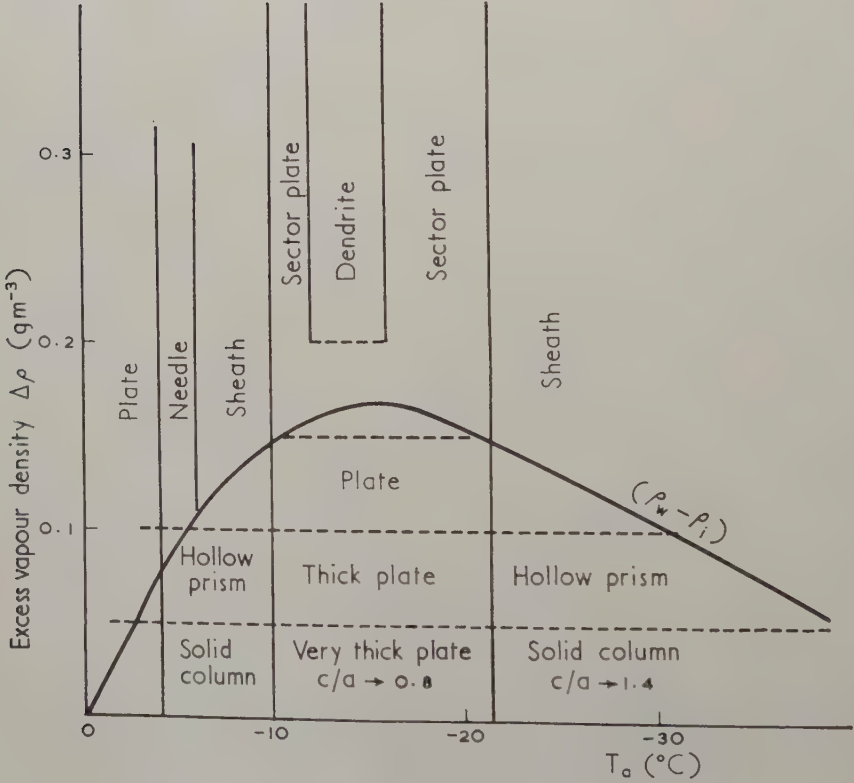
Fig. 5
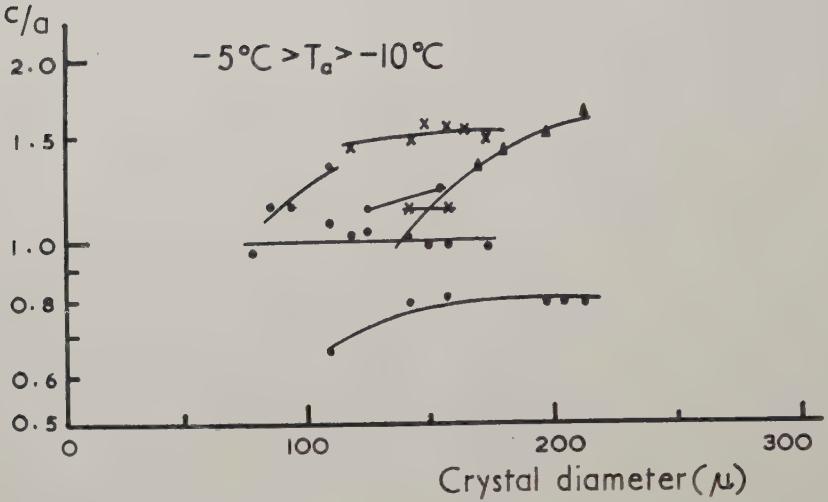


Fig. 6

than 3%, revealed that they grew more plate-like with time approaching a limiting $c/a$ ratio of about 0·8, as shown in fig. 3. It was also observed that whether small crystals alighting on the filaments were originally plate-like ($c/a < 1$) or originally prism-like ($c/a > 1$) their subsequent growth tended towards this limiting form of a very thick plate although with the larger crystals this became apparent only after several hours of growth.

Fig. 7
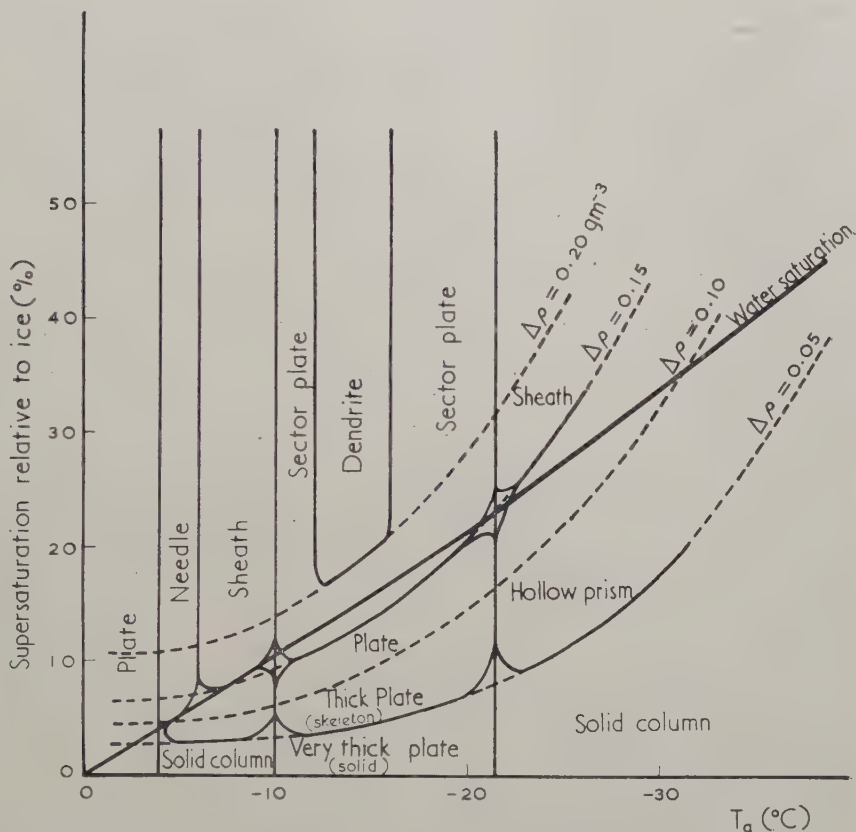


At temperatures between $-23°$c and $-32°$c (the lowest reached in these experiments) the crystals grew more prism-like and showed a tendency to approach a limiting $c/a$ ratio of about 1·4 as shown in fig. 4. At lower temperatures the transition from solid to hollow prisms occurred at higher supersaturations. At $-24°$c solid prisms were observed at supersaturations of up to 118% relative to ice but, at higher values, hollow prisms appeared as in the diffusion chamber experiments.

There was considerable difficulty in nucleating crystals at temperatures above $-10°$c but a few were grown at temperatures between $-10°$c and $-5°$c and their growth is plotted in fig. 5. These crystals, which tended to develop into hoppers when they exceeded about $150\,\mu$ in length, were

definitely prism-like but showed no marked trend towards a limiting habit
as was the case at lower temperatures.

## § 4. Discussion

Consolidating the present results with those of Nakaya (1954), Shaw
and Mason (1955), Hallett and Mason (1958) and Kobayashi (1957, 1958,
1960) the variation of snow-crystal habit with temperature and super-
saturation or excess vapour density may be represented by figs. 6 and 7.

It is clear that the principal factor controlling the basic habit, as
determined by the relative growth rates along the $c$ and $a$ axes, is the
temperature.

But, as figs. 6 and 7 show equally clearly, the secondary growth features
are determined by the supersaturation or flux of vapour. Increasing
supersaturation causes transition from very thick plate→thick plate→
sector plate→dendrite, or from solid prism→hollow prism→needle.

The present experiments strongly suggest that, at very low super-
saturations, there is a marked tendency towards a solid isometric habit at
all temperatures (although it was not possible to obtain measurements
above $-5°$c), the factor responsible for the striking temperature variation
of habit at higher supersaturations having less and less influence as the
supersaturation is reduced.

## References

Hallett, J., and Mason, B. J., 1958, *Proc. roy. Soc.* A, **247**, 440.
Isono, K., Komabayashi, M., and Ono, A., *J. met. Soc. Japan*, **35**, 327.
Isono, K., 1958, *Nature, Lond.*, **182**, 1221.
Kobayashi, T., 1957, *J. met. Soc. Japan*, 75th Ann. Vol. 38 ; 1958, *Ibid.*, **36**, 193 ; 1960, *Ibid.*, **38**, 231.
Marshall, J. S., and Langleben, M. P., 1954, *J. Meteor.*, **11**, 104.
Nakaya, U., 1954, *Snow Crystals* (Harvard : University Press).
Shaw, D., and Mason, B. J., 1955, *Phil. Mag.*, **46**, 249.
Van den Heuvel, A. P., and Mason, B. J., 1959, *Nature, Lond.*, **184**, 519.

# The Analysis of (d, p) Stripping Reactions by the Distorted Wave Born Approximation

By B. Buck† and P. E. Hodgson
Clarendon Laboratory, Oxford

## Abstract

The formulae giving the differential cross section for a (d, p) stripping reaction, the polarization of the outgoing proton and the angular correlation between it and the gamma ray from the residual nucleus are summarized for the distorted wave Born approximation. Methods of programming this calculation for an electronic computer are described, and the results of some check calculations are given.

## § 1. Introduction

MANY authors (Butler 1950, 1951, Daitch and French 1952, Friedman and Tobocman 1953, Horowitz and Messiah 1953, 1954, Newns 1953) have considered the quantum-mechanical theory of the deuteron stripping process, in which a deuteron brushes past a nucleus and loses its neutron, the proton going on alone. The outgoing proton is usually polarized. The neutron is captured into a discrete quantum state of the residual nucleus and, if this is not the ground state, gamma rays may be subsequently emitted from the excited nucleus.

The conservation of angular momentum imposes the relations

$$\mathbf{J}_i + \mathbf{l}_n + \tfrac{1}{2} = \mathbf{J}_f, \quad \pi_i \pi_f = (-1)^l \qquad \ldots \quad (1)$$

on the angular momentum $\mathbf{l} \equiv \mathbf{l}_n$ of the captured neutron, and $\mathbf{J}_i$, $\pi_i$ and $\mathbf{J}_f$, $\pi_f$ the spins and parities of the initial and final nuclei respectively. The angular distribution of the emitted proton is frequently characteristic of the value of $\mathbf{l}_n$, and if $\mathbf{J}_i$ is known this allows close limits to be set on $\mathbf{J}_f$.

It is not yet possible to make an exact quantum mechanical analysis of the stripping process, but if certain assumptions are made a useful quantitative account can be given of most features of the interaction.

The simplest theory, due to Butler, uses the Born approximation to obtain the reaction amplitude in the form

$$I_l(\mathbf{k}_p, \mathbf{k}_d) \propto \int_{R_0}^{\infty} j_l(qr) \, h_l^{(1)}(ikr) \, r^2 \, dr. \qquad \ldots \quad (2)$$

The differential cross section for the stripping process when one $l$-value contributes then becomes

$$\frac{d\sigma(\theta)}{d\Omega} \propto \left| \frac{W_l(q,k)}{(qR)^2 + (kR)^2} \right|^2 \qquad \ldots \ldots \quad (3)$$

where
$$W_l(q,k) = R\left[ \frac{dj_l(qR)}{dR} - \frac{j_l(qR)}{h_l^{(1)}(ikR)} \cdot \frac{dh_l^{(1)}(ikR)}{dR} \right] \qquad \ldots \quad (4)$$

---

† Now at Oak Ridge National Laboratory, Tennessee, U.S.A.

and $\theta$ is the scattering angle in the centre-of-mass system,

$$\mathbf{l} \equiv \mathbf{l}_n = 0, 1, 2, 3, \ldots, \quad \mathbf{q} = \mathbf{k}_d \hbar - \mathbf{k}_p' \hbar$$

is the momentum transfer, $R_0$ is the cut-off radius, $j_l(qR)$ is a spherical Bessel function and $h_l^{(1)}(ikR)$ a spherical Hankel function of the first kind with imaginary argument.

The wave numbers are given by

$$k_d = \frac{(2M_d^* E_d^*)^{1/2}}{\hbar}; \quad k_p' = \frac{M_T}{M_R} \cdot \frac{[2M_p^*(E_d^* + Q)]^{1/2}}{\hbar}; \; k = \frac{[2M_n^*(Q + 2 \cdot 226)]^{1/2}}{\hbar}$$

$$\cdots \quad (5)$$

and the reduced quantities are

$$M_d^* = \frac{M_d M_T}{M_d + M_T}; \quad M_p^* = \frac{M_p M_R}{M_p + M_R}; \; M_n^* = \frac{M_n M_T}{M_n + M_T}: E_d^* = \frac{M_d^* E_d}{M_d}.$$

$$\cdots \quad (6)$$

$E_d$ is the incident deuteron energy in the laboratory system and $M_n$, $M_p$, $M_d$, $M_T$ and $M_R$ the masses of the neutron, proton, deuteron, target nucleus and residual nucleus respectively. Explicit values of $W_l(q, k)$ for $\mathbf{l} = 0, 1, 2, 3$ are given in Appendix I. Tables of Butler stripping cross sections have been prepared by Lubitz (1957).

This formula contains the adjustable cut-off radius $R_0$ and an overall normalization parameter. It usually gives a surprisingly good fit to the differential cross section in the forward direction, but greatly underestimates the backward cross section. It is, however, unable to give the polarization of the emitted proton or the reduced width of the reaction, which depends on the overall normalization.

A more accurate theory can be developed by taking into account the distortions of the incoming deuteron wave and the outgoing proton wave in the Coulomb and nuclear fields of the target and residual nuclei. This theory, known as the distorted wave Born approximation, has been developed by many authors (Thomas 1955, Tobocman and Kalos 1955, Newns and Refai 1958, Tobocman 1959, Huby *et al.* 1959). They have given detailed derivations of the formulae used to calculate the observable quantities. In this paper the aim is not to repeat this work, but to present the formulae in a form especially suitable for electronic computation. This is done in §2, and in §3 some of the numerical techniques used to evaluate them are described. In the last section some comparisons with other work and with the Butler theory are made. Full details and discussion of the derivations of the formulae quoted here have been given by Buck (1960).

## § 2. The Distorted Wave Born Approximation

It may be shown from the general S-matrix theory of nuclear reactions that the reaction amplitude for the (d, p) stripping interaction may be written approximately as

$$I(M_T \mu_d; M_R \mu_p : \mathbf{k}_d, \mathbf{k}_p) = -\left\{ \frac{M_d^* M_p^*}{(2\pi\hbar^2)^2} \cdot \frac{k_p}{k_d} \right\}^{1/2} \int f_{k_p}^{(-)*}(\mathbf{r}_p') \chi_S^{\mu*}(p)$$

$$\psi_J^{M*}(R : \xi, \mathbf{r}_n, \mathbf{s}_n) V f_{k_d}^{(+)}(\mathbf{r}_n, \mathbf{r}_p) \chi_S^{\mu}(d) \psi_J^{M}(T : \xi) d\mathbf{r}_n \, d\mathbf{r}_p \, d\xi \quad \cdots \quad (7)$$

where $\psi_J{}^M$ (T) and $\psi_J{}^M$(R) are respectively the wave functions of the target and residual nuclei $f_{k_d}{}^{(+)}(\mathbf{r_n},\ \mathbf{r_p})$ and $f_{k_p}{}^{(-)}(\mathbf{r_p}')$ are the spatial wave functions of the deuteron and proton; $\chi_S{}^\mu(\mathrm{p})$ is the proton spin function and $\chi_S{}^\mu(\mathrm{d})$ the triplet deuteron spin function; $\xi$ represents the internal coordinates of the target nucleus; $\mathbf{r_n}$ and $\mathbf{r_p}$ are the position coordinates of the proton and neutron relative to the centre-of-mass of the residual nucleus and

$$\mathbf{r_p}' = \mathbf{r_p} - \{M_n/M_R\}\mathbf{r_n};$$

and $V$ is the interaction in the final state between the proton and residual nucleus.

The interaction $V$ may be expressed in the form

$$V = V_{pn} + \{V_{pT} - \bar{V}_{pT}\} \quad . \quad . \quad . \quad . \quad . \quad . \quad (8)$$

where $V_{pn}$ is the proton–neutron interaction responsible for the binding of the deuteron, $V_{pT}$ is the interaction of the proton with the target nucleus and $\bar{V}_{pT}$ is the average proton-target interaction that has already been taken into account in the construction of the distorted proton waves.

In order to evaluate the integral for the reaction amplitude the following approximations are made:

(1) The distorting potentials are spin-independent. This is likely to be a good approximation for the differential cross section, but not for the polarization of the emitted proton.

(2) The contribution of $(V_{pT} - \bar{V}_{pT})$ is small. The elastic effects of $V_{pT}$ are essentially included also in $\bar{V}_{pT}$ while the inelastic effects should be small since they involve excitation of the target nucleus by the outgoing proton as well as the capture of the neutron.

(3) Exchange contributions resulting from antisymmetrization of the wave functions are negligible.

(4) $V_{np}$ is a triplet state central potential so that the internal deuteron wave function separates into space and spin factors $\phi_d(\mathbf{r_n} - \mathbf{r_p})$ and $\chi_S{}^\mu(\mathrm{d})$. Spin-flipping effects due to the dependence of $V_{np}$ on spin orientations are thereby neglected. Tensor effects arising from the small D-state component of the deuteron wave function and the spin dependent part of the $V_{np}$ interaction are expected to be small. In order to make the evaluation of the integral practicable we take the $V_{np}$ interaction to be of zero range.

(5) All nuclei and distorting potentials are assumed spherical.

It is most convenient to evaluate the above expression for the reaction amplitude in the coordinate system with the $z$-axis along $\mathbf{k_d}$ (the axis of quantization), and the $y$-axis along the normal to the reaction plane $\mathbf{n} = \mathbf{k_d} \times \mathbf{k_p}$, where $\mathbf{k_p}$ is the relative momentum of the proton and the final nucleus.

In this coordinate system, and making use of the above approximations, the integral for the reaction amplitude can be evaluated to give the

following expressions for the differential cross section, polarization of the emitted proton along the direction **n** :

$$\frac{d\sigma}{d\Omega} = \frac{4AM_d^*M_p^*}{M_n^2} \cdot \frac{(2J_r+1)}{(2J_t+1)} \cdot \frac{k_p}{k_d} \sum_{jl} \theta_{jl}^2 \sum_\lambda |B_{l\lambda}(\theta_p)|^2 \quad . \quad . \quad (9)$$

$$P = \frac{2}{3} \cdot \frac{\sum_{jl} \theta_{jl}^2 \dfrac{(-)^{j-l-1/2}}{2j+1} \sum_\lambda \{(l-\lambda+1)(l+\lambda)\}^{1/2} \operatorname{Im}\{B_{l\lambda}^* B_{l\lambda-1}\}}{\sum_{jl} \theta_{jl}^2 \sum_\lambda |B_{l\lambda}|^2} \quad (10)$$

where

$$B_{l\lambda}(\theta_p) = \sum_{l_d l_p} \Gamma_{l_d l_p}^{l\lambda} \exp\left[i(\omega_{l_d} + \omega_{l_p})\right] I(l_d l_p l) P_{l_p}^\lambda (\cos \theta_p), \quad (11)$$

$$\Gamma_{l_d l_p}^{l\lambda} = i^{l_d - l_p - l} (2l_p+1) \left[\frac{(l_p-\lambda)!}{(l_p+\lambda)!}\right]^{1/2} C_{0-\lambda\lambda}^{l_d l_p l} C_{000}^{l_d l_p l} , \quad . \quad . \quad (12)$$

$$I(l_d l_p l) = \int_{R_0}^{\infty} \psi_{l_d}(r) \psi_{l_p}(r) R_l(r) r^2 dr ; \quad . \quad . \quad (13)$$

$\omega_l = \sigma_l - \sigma_0$, the $\sigma_l$'s being Coulomb phase shifts.

$A^{-1} = (\hbar/M_n B)^{1/2} \sim 4 \cdot 4 \times 10^{-13}$ cm is the 'radius' of the deuteron, $B$ being its binding energy. The $\theta_{jl}^2$ are reduced widths or generalized parentage coefficients defined by

$$\int \psi_J^{M*}(R:\mathbf{r}_n, \xi)\psi_J^M(T:\xi)\,d\xi = \sum_{jl}\theta_{jl} C_{M_r M_t m}^{J_r J_t j} C_{m\lambda\mu}^{jls} R_l(r_n)\{i^l Y_l^m(\mathbf{r}_n)\}^* \chi_s^{\mu*}.$$

$$. \quad . \quad . \quad (14)$$

In the coordinate frame defined above the $B_{l\lambda}$ obey the symmetry relation

$$B_{l\lambda}(\theta_p) = (-1)^\lambda B_{l-\lambda}(\theta_p) . \quad . \quad . \quad . \quad . \quad . \quad (15)$$

The deuteron and proton wave functions

$$\psi_{l_d}(r) = u_{l_d}(r)/kr \quad \text{and} \quad \psi_{l_p}(r) = u_{l_p}(r)kr$$

are calculated by numerical integration of the appropriate wave equation of the form

$$\frac{d^2 u_l}{d\rho^2} + \left[1 - \frac{V(\rho)}{E} - \frac{l(l+1)}{\rho^2} - \frac{C(\rho)}{E}\right] u_l = 0 \quad . \quad . \quad . \quad (16)$$

where $\rho = kr$ and the nuclear potential has the form

$$V(\rho) = \frac{V}{1+\exp\{(\rho-\rho_0)/\alpha_1\}} + \frac{iW}{1+\exp\{(\rho-\rho_0)/\alpha_2\}} \quad . \quad . \quad (17)$$

where $V$ and $W$ are the real and imaginary potential depths, $\rho_0 = kR$, where $R = r_0 A_T^{1/3}$ is the nuclear radius and $\alpha = ka$, where $a$ is the diffuseness of the nuclear surface. The Coulomb potential $C(\rho)$ is that due to a uniformly charged sphere of radius $R_c$. Beyond the nuclear field the solutions have the asymptotic forms

$$\psi_{l_d}(r) \sim \frac{F_{l_d}(k_d r) - \alpha_{l_d} H_{l_d}(k_d r)}{k_d r}, \quad . \quad . \quad . \quad (18)$$

$$\psi_{l_p}(r) \sim \frac{F_{l_p}(k_p'r) - \beta_{l_p} H_{l_p}(k_p'r)}{k_p'r} \quad . \quad . \quad . \quad . \quad (19)$$

where the $H$'s are defined by

$$H_l(\rho) = F_l(\rho) - iG_l(\rho), \quad . \quad . \quad . \quad . \quad . \quad (20)$$

the $F_l(\rho)$ and $G_l(\rho)$ being the regular and irregular Coulomb wave functions that are solutions of the wave equation:

$$\frac{d^2 u_l}{d\rho^2} - \left[1 - \frac{2\gamma}{\rho} - \frac{l(l+1)}{\rho^2}\right] u_l = 0 \qquad \ldots \ . \ (21)$$

and have the asymptotic forms

$$F_l(\rho) \sim \sin\left(\rho - \gamma \ln 2\rho - \tfrac{1}{2}l\pi + \sigma_l\right), \qquad \ldots \ . \ . \ (22)$$

$$G_l(\rho) \sim \cos\left(\rho - \gamma \ln 2\rho - \tfrac{1}{2}l\pi + \sigma_l\right) \qquad \ldots \ . \ . \ . \ (23)$$

where $\gamma = \mu Z_I Z_T e^2/k\hbar^2$, $Z_I$ and $Z_T$ being the charges on the incident and target nuclei.

The internal and external solutions of (16) are matched beyond the nuclear field and this fixes the normalization of the internal wave functions and also the complex scattering parameters that describe the scattering process:

$$\alpha_{l_d} = \tfrac{1}{2}(1 - S_{l_d}), \quad \beta_{l_p} = \tfrac{1}{2}(1 - S_{l_p}). \qquad \ldots \ . \ . \ (24)$$

The complete deuteron and proton wave functions $\psi_{l_d}(\rho)$ and $\psi_{l_p}(\rho)$ are calculated in this way from nuclear potentials of the form (17) with parameters that give the experimentally observed elastic scattering. Further details of this calculation are given by Buck *et al.* 1960 (see Appendix II for corrections to this paper).

The neutron bound state wave function $R_l(r) = u_l(kr)/r$ has often been obtained by matching an harmonic oscillator wave function for the internal region to the Hankel function that is the accurate asymptotic form and depends only on the neutron binding energy. The matching is done at an arbitrary radius in the vicinity of the nuclear surface and the parameters of the harmonic oscillator potential have to be varied until the internal and external functions join smoothly. This is unsatisfactory as it gives rise to an unphysical shape for the effective nuclear binding potential. It is more realistic to use the wave function corresponding to a particle of known binding energy in a Saxon–Woods potential of appropriate depth. This may be found by a calculation similar to that for the free state scattering problem except that now the nuclear potential, and hence the wave function, is real, and has a completely known asymptotic form at large distances. This condition, together with the quantum state of the neutron, fixes the wavefunction and the depth $V_n$ of a potential of given radial form. It is therefore not possible to calculate $u_l(\rho)$ directly, since the appropriate $V_n$ is not known. Instead, an approximate value of $V_n$ is chosen and used to calculate the wave function inside the nuclear potential. In general this does not join smoothly with the known external wave function, but application of the variational principle to the mismatch in the region of the nuclear surface enables a better value of $V_n$ to be found. A few iterations suffice to determine $V_n$ to the accuracy required (see Appendix III).

The gamma-ray correlation function is given by

$$W(\theta_p : \theta', \phi') = \sum_k g_k \{d_{k0} P_k (\cos \theta')$$

$$+ 2 \sum_{q>0} (-1)^q \left[\frac{(k-q)!}{(k+q)!}\right]^{1/2} P_k{}^q (\cos \theta') \, |d_{kq}| \cos q \, (\phi' - \alpha_{kq})\} \qquad \ldots \ . \ . \ (25)$$

where $k$ is even and restricted by $k \leqslant 2J_r$ or $l+l'$ or $j+j'$ whichever is the smaller. The coefficients $g_k$ depend on the nuclear spins and the gamma-ray decay multipole mixing constants. The $d_{kq}$ and $\alpha_{kq}$ depend only on the $B_{l\lambda}(\theta_p)$ but as the formulae are complicated they will not be reproduced here. Full details of the calculation of these coefficients are given by Satchler and Tobocman (1960), and in the papers quoted by them.

Some explicit expressions for the observable quantities in the cases $I = 1$ and $I = 2$ are given in Appendix IV.

## § 3. Numerical Calculations

The whole calculation was programmed for the Oxford Mercury electronic computer using the Autocode facility. The numerical methods used to solve the sets of differential equations and extract the elements $S_L$ of the scattering matrix are essentially those described previously (Buck *et al.* 1960). The Runge–Kutta sub-routine was initially used for the numerical integrations for ease of programming, but conversion to the faster Fox–Goodwin method is now being carried out (Halton 1960, private communication). Three separate programmes were written for angular momentum transfers $I = 0$, 1 and 2. This enables the angular momentum factors $\Gamma_{l_d l_p}^{l\lambda}$ to be evaluated explicitly in each case, as the appropriate Clebsch–Gordan coefficients then have simple numerical values.

The proton, deuteron and neutron wave functions were calculated from the numerical integration of the appropriate wave equations as described in the last section, and then multiplied together step by step to give the numerical values of the integrals $I(l_d l_p l)$. The lower limit of this integration may be selected at will, and the upper limit is chosen to be sufficiently large for the product of the wave functions to be negligible. The integrals $I(l_d l_p l)$ were calculated for all values of $l_d$ and $l_p$ that contribute significantly to the interaction. The summation of the $I(l_d l_p l)$ to give the $B_{l\lambda}$ and hence the differential cross sections, polarizations and gamma-ray correlations is straightforward.

The input parameters for a full calculation are the incident deuteron energy $E_d$, the $Q$-value of the reaction, the mass $A_T$ charge $Z_T$ and spin $J_T$ of the target nucleus, the spin $J_R$ of the residual nucleus, the reduced widths $\theta^2_{l\pm1/2}$ for the two possible spin orientations (if $I = 0$ there is only one reduced width), the cut-off radius $R_0$, the principal quantum number of the bound neutron, the estimated depth $V_n$ and form factor parameters $r_{0n}$ and $a_n$ for the neutron potential, the parameters $V_d$, $W_d$, $r_{0d}$, $r_{cd}$, $a_{1d}$, $a_{2d}$ of the deuteron nuclear potential and the corresponding parameters for the proton nuclear potential. A facility was incorporated that allows the imaginary parts of the deuteron and proton potential to have a gaussian instead of a Saxon–Woods radial form, and corresponding switches are included in the input parameters. The upper limit of the integrals in (13) is the radial distance at which the neutron bound state wave function $R(r_n)$ is effectively negligible, i.e. has less than about $10^{-3}$ of its value at the nuclear surface. The time taken for a complete calculation varies roughly

as the square of the nuclear radius, and for the case of $^{24}$Mg (d, p)$^{25}$Mg* is about 15 min for $l=0$, 25 for $l=1$ and 35 for $l=2$. These times can be substantially reduced by using the Fox–Goodwin method of numerical integration and by integrating all the partial waves simultaneously.

### §4. COMPARISONS AND CHECKS

A number of calculations were made to study the effects of the Coulomb and nuclear distorting potentials, and to check the calculation against other work. Figure 1 shows a comparison between the angular distributions for

Fig. 1



$O^{16}$(d,p)$O^{17}$ (ground state)
(1d) capture.

Distortion Effects = 3 MEV.

1. No distortions (Plane Waves).
2. Coulomb distortions only.
3. Nuclear distortions only.
4. Both distortions present

Cut-off R = 5f.
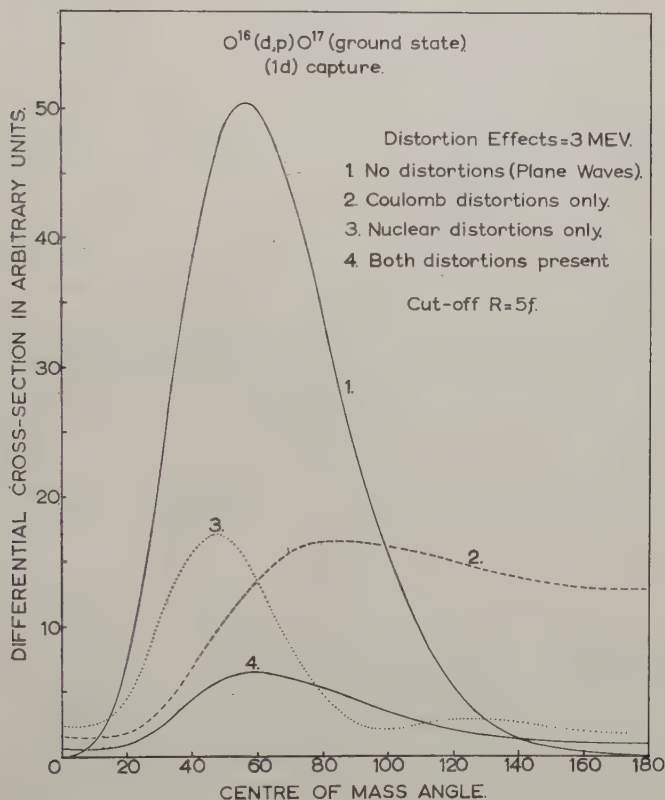
Comparison between the angular distribution of the protons from the reaction $^{16}$O(d, p$_0$)$^{17}$O calculated according to the Butler theory and the corresponding distributions calculated with the distorted wave Born approximation with the Coulomb and nuclear distorting potentials acting alone and then together.

the reaction $^{16}$O(d, p$_0$)$^{17}$O calculated on ($a$) the Butler plane-wave theory, ($b$) DWBA with Coulomb distortion only, and ($c$) DWBA with nuclear distortions only, and ($d$) full DWBA with both Coulomb and nuclear

Fig. 2
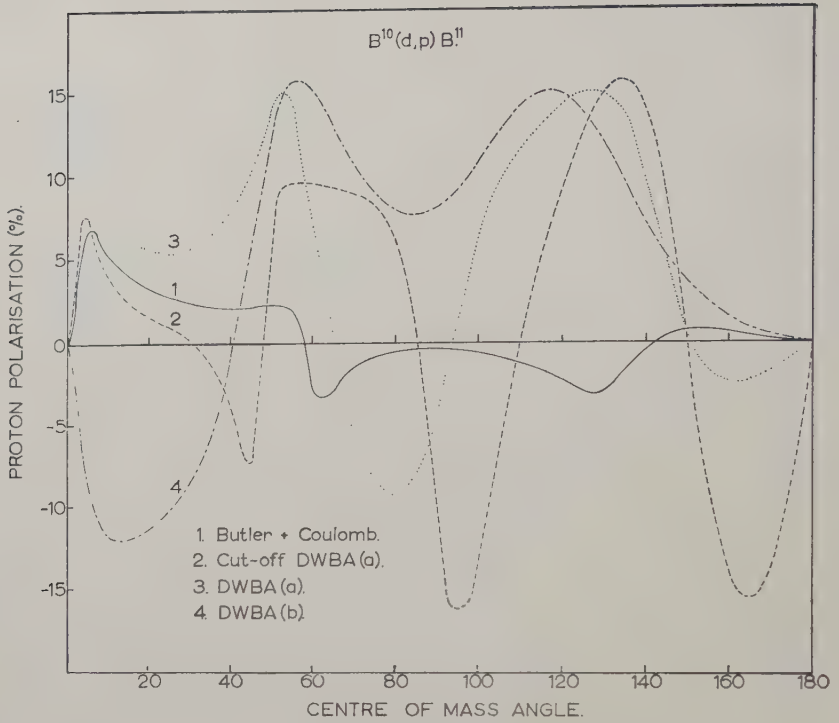


Calculated polarizations of protons from the reaction $^{10}$B(d, p)$^{11}$B for different approximations and using the same parameters as Tobocman (1959). These curves may be compared with those in fig. 3 of his paper.

Fig. 3
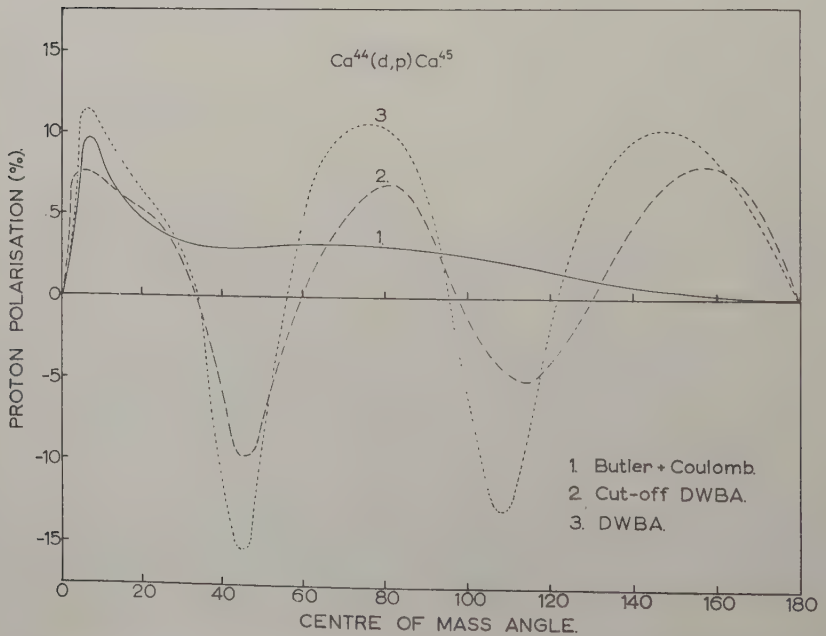


Calculated polarizations of protons from the reaction $^{44}$Ca(d, p)$^{45}$Ca for different approximations using the same parameters as Tobocman (1959). These curves may be compared with those in fig. 7 of his paper.

distortions. It is found that individually the two types of distortions produce an angular distribution markedly different from the Butler distribution, but that together they tend to have opposite effects and give a final distribution very similar to the Butler, but with only about one-tenth of the absolute magnitude. This illustrates how, perhaps fortuitously, the plane-wave theory can give the angular distribution correctly, and yet still be unreliable for the reduced widths.

Fig. 4
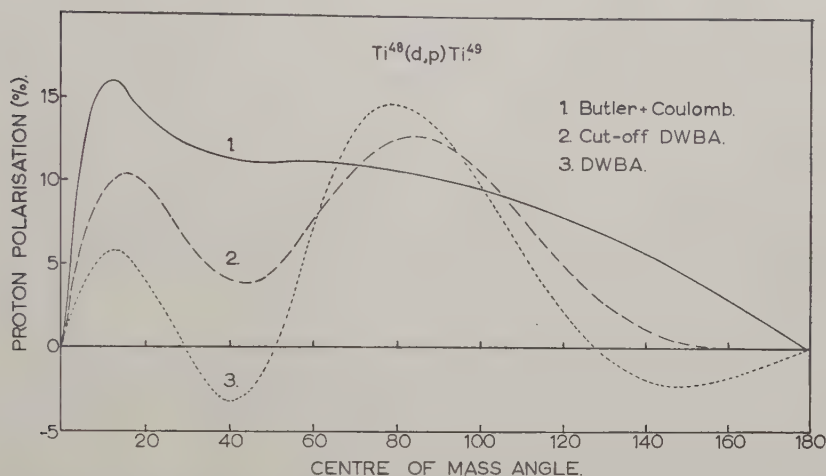


Calculated polarizations of protons from the reaction $^{48}$Ti(d, p)$^{49}$Ti for different approximations using the same parameters as Tobocman (1959). These curves may be compared with those in fig. 13 of his paper.

The following check calculations were made:

1. The nuclear and Coulomb distortions were set to zero, a suitable cut-off radius chosen and the resulting angular distribution found to agree with the corresponding Butler distribution to within 1%.

2. The incident energy was chosen so that $k_d = k_p'$, and the optical potential parameters adjusted so that the distortions of the deuteron and proton waves are identical. According to Refai's theorem (Satchler 1960) the polarization of the emitted proton should be zero; it was found that $|P| \leqslant 10^{-5}$ over the whole angular range.

3. The calculations of Tobocman (1959) were repeated using his parameters for the distorting potentials. The comparison is best made for the cut-off case when the lower limit of the radial integral (13) has a finite value, since our bound neutron function differs markedly from Tobocman's within the nuclear field. The results of calculations of the polarizations of protons from the (d, p) reactions on $^{10}$B, $^{44}$Ca and $^{48}$Ti are given in figs. 2–4,

and are in good overall agreement with the corresponding calculations of Tobocman. The differential cross-sections, being less sensitive to the details of the calculations, are in even better agreement. The small discrepancies between the two calculations may be due to (*a*) slightly different radial form factor for the nuclear potentials (Tobocman uses a uniform distribution inside the nucleus with a Saxon–Woods fall-off outside), (*b*) different bound state wave functions (Tobocman uses those corresponding to an harmonic oscillator well), and (*c*) different numerical approximations.

4. The tensor angles $\phi_0$ and $\phi_1$ in the gamma-ray correlation function were checked by making a plane-wave calculation with $l = 2$. The values of $\phi_0$ and $\phi_1$ agreed to within $1\%$ with the recoil angles calculated from the kinematics of the reaction.

## APPENDIX I

Explicit forms of the factor $W_l(q, k)$ occurring in the Butler formula for the stripping cross section are:

$$W_0(q, k) = [\{1 + kR\}j_0(qR) - qRj_1(qR)], \qquad \cdots \qquad (\text{I } 1)$$

$$W_1(q, k) = \left[ \sin(qR) + \frac{(kR)^2 j_1(qR)}{1 + kR} \right], \qquad \cdots \qquad (\text{I } 2)$$

$$W_2(q, k) = \left[ qRj_1(qR) + \frac{(kR)^2\{1 + kR\}j_2(qR)}{3 + 3kR + (kR)^2} \right], \qquad \cdots \qquad (\text{I } 3)$$

$$W_3(q, k) = \left[ qRj_2(qR) + \frac{(kR)^2\{3 + 3kR + (kR)^2\}j_3(qR)}{15 + 15kR + 6(kR)^2 + (kR)^3} \right] \cdots \quad (\text{I } 4)$$

## APPENDIX II

The following are the correct forms of expressions in the paper on the optical model analysis of nuclear scattering by Buck *et al.* (1960):

$$\sigma_T = \frac{2\pi}{k^2} \sum_{l=0}^{\infty} \{(l+1)(1 - \mathrm{Re}\, S_l^+) + l(1 - \mathrm{Re}\, S_l^-)\}, \qquad \cdots \quad (12)$$

$$S_1 = \frac{\gamma^3 - \gamma}{2\rho^2} - \frac{\gamma^2}{2\rho} \quad \text{etc.} \qquad \cdots \cdots \quad (19)$$

The fourth and sixth entries on the right-hand side of table 5 should read 6·724, 1 and 7·807, 0 respectively. The sign of the spin–orbit term in table 6 is the unphysical one.

# APPENDIX III

## CALCULATION OF THE NEUTRON BOUND STATE WAVE FUNCTION†

It is required to calculate the wave function $u_l(\rho)$ of a neutron in a given quantum state bound in a potential well of known shape and radius but unknown depth $V$. The radial wave equation it satisfies is

$$\frac{d^2 u_l}{d\rho^2} + \left[ \frac{V}{B} f(\rho) - \frac{l(l+1)}{\rho^2} - 1 \right] u_l = 0. \quad \cdots \quad \text{(III 1)}$$

where $\rho = kr$, $k^2 = 2M_n^* B/\hbar^2$, $B$ being the binding energy.

Let $\rho_E$ be the radius at which the nuclear field is negligible, and let the wave functions in the three radial regions be as follows: (1) $u_I(\rho)$ in the internal region $0 \leqslant \rho \leqslant \rho_M$; (2) $u_E(\rho)$ in the external region $\rho_M < \rho \leqslant \rho_E$; (3) and $u_F(\rho)$ in the far external region $\rho \geqslant \rho_E$.

In the far external region $f(\rho) \approx 0$ and the wave equation (III 1) has the analytical solution

$$u_F(\rho) = e^{-\rho} \left[ 1 + \frac{l(l+1)}{1! \, 2\rho} + \frac{l(l-1)(l+1)(l+2)}{2! \, (2\rho)^2} + \cdots \right]. \quad \text{(III 2)}$$

This gives the starting values for the inward integration of (III 1) from $\rho_E$ to $\rho_M$. Similarly the outward integration from 0 to $\rho_M$ makes use of the solution for small $\rho$

$$u_I(\rho) = \rho^{l+1}. \quad \cdots \quad \cdots \quad \cdots \quad \text{(III 3)}$$

The choice of $\rho_M$ is not critical, and it is convenient to take it as the position of the last zero of

$$\frac{V}{B} f(\rho) - \frac{l(l+1)}{\rho^2} - 1 \quad \cdots \quad \cdots \quad \text{(III 4)}$$

as $\rho$ increases from zero. This is where the character of the solution changes from oscillatory to monotonic.

For convenience, re-write (III 1) in the form

$$u'' + [Wf(\rho) - D - 1]u = 0, \quad W = V/B. \quad \cdots \quad \text{(III 5)}$$

Let $W_0$ be the first (guessed) approximation to $W$, so that

$$W = \lambda W_0. \quad \cdots \quad \cdots \quad \cdots \quad \text{(III 6)}$$

Then

$$u'' + (W_0 f(\rho) - D - 1)u = (1 - \lambda) W_0 f(\rho)u. \quad \cdots \quad \text{(III 7)}$$

If this is multiplied through by $u$ and integrated from 0 to $\infty$ it becomes

$$\lambda = 1 - \frac{\displaystyle\int_0^\infty u[d^2/d\rho^2 + W_0 f(\rho) - D - 1]u \, d\rho}{\displaystyle\int_0^\infty W_0 f(\rho) u^2 \, d\rho}. \quad \cdots \quad \text{(III 8)}$$

Using the wave function $u_0$ that satisfies the equation

$$u_0'' + [W_0 f(\rho) - D - 1]u_0 = 0 \quad \cdots \quad \cdots \quad \text{(III 9)}$$

in place of $u$ in (III 8), an approximate value $\lambda_1$ of $\lambda$ may be found.

---

† This method was suggested by Dr. L. M. Delves.

Since there is, in general, a mismatch at $\rho = \rho_M$, the integration range is split into the internal and external regions. It is necessary to normalize the interior and exterior solutions at the matching radius. The numerator vanishes except at $\rho_M$, and $W_0 f(\rho) = 0$ in the far external region, so that

$$\lambda_1 = 1 - \frac{\{[u_E u_E'] - [u_I u_I'][u_E/u_I]^2\}_{\rho = \rho_M}}{\left(\dfrac{u_E}{u_I}\right)^2_{\rho = \rho_M} \displaystyle\int_0^{\rho_M} u_I{}^2 \, W_0 f(\rho) \, d\rho + \int_{\rho_M}^{\rho_E} u_E{}'^2 \, W_0 f(\rho) \, d\rho}. \qquad \text{(III 10)}$$

All the quantities on the right of this equation are known from the integration of the wave equation. The next approximation to $W$ is then

$$W_1 = \lambda_1 W_0. \quad . \quad . \quad . \quad . \quad . \quad . \quad \text{(III 11)}$$

This new value of $W$ may be inserted in (III 9) to give $u_1$, and hence $\lambda_2$ by using these new functions in (III 10). This iterative procedure may be repeated until no further improvement is obtained. After n iterations,

$$W_n = \lambda_n \lambda_{n-1} \dots \lambda_1 W_0. \quad . \quad . \quad . \quad . \quad \text{(III 12)}$$

The well-depth is given by

$$V = B W_n. \quad . \quad . \quad . \quad . \quad . \quad . \quad \text{(III 13)}$$

The wave function is the solution of (III 1) with this value of $V$, and is obtained during the last iteration. It may be normalized so that

$$\int_0^\infty u^2 \, d\rho = 1 \quad . \quad . \quad . \quad . \quad . \quad . \quad \text{(III 14)}$$

by dividing it by $\beta$, where

$$\beta^2 = \left(\frac{u_E}{u_I}\right)^2_{\rho = \rho_M} \int_0^{\rho_M} u_I{}^2 \, d\rho + \int_{\rho_M}^{\rho_E} u_E{}^2 \, d\rho + \int_{\rho_E}^\infty u_F{}^2 \, d\rho. \qquad \text{(III 15)}$$

It is necessary to verify that the wave function has the correct number of nodes for the specified quantum state.

A reasonable first guess to $V$ is in the region of 40 Mev, but it is better to have a more accurate way of estimating it because if the value used is too inaccurate the iteration procedure will give a wave function with the wrong number of nodes. This may be done by solving the corresponding square well problem analytically.

The wave equation is

$$\frac{d^2u}{d\rho^2} + \left[\alpha^2 - \frac{l(l+1)}{\rho^2}\right] u = 0. \qquad . \quad . \quad . \quad \text{(III 16)}$$

For $\rho > \rho_0$, the radius of the square well, $\alpha^2 = -1$ and $u_E$ is given by (III 2). For $\rho < \rho_0$, the solution is

$$u_I \propto \rho j_L(\alpha\rho), \quad \alpha^2 = (V/B) - 1. \quad . \quad . \quad . \quad \text{(III 17)}$$

Now $u_E$ contains no nodes, and the $N$th node of $j_l(\alpha\rho)$ occurs approximately at

$$\alpha\rho = (N + \tfrac{1}{2}l)\pi. \quad . \quad . \quad . \quad . \quad . \quad . \quad \text{(III 18)}$$

Thus for $\rho_0$ such that

$$(N + 1 + \tfrac{1}{2}l)\pi > \alpha\rho_0 > (N + \tfrac{1}{2}l)\pi, \quad . \quad . \quad . \quad \text{(III 19)}$$

there are $N$ nodes in $j_l(\alpha\rho)$ from $\rho = 0$ to $\rho = \rho_0$.

If we take

$$\alpha\rho_0 = [N + \tfrac{1}{2}(l+1)]\pi, \qquad \text{. . . . . . (III 20)}$$

then

$$\frac{V}{B} \approx 1 + \frac{\{N + \tfrac{1}{2}(l+1)\}^2\pi^2}{\rho_0^2}. \qquad \text{. . . . (III 21)}$$

This expression may be used to estimate $V$ from $N$, $L$ and $B$. If this value of $V$ gives a wave function with an incorrect number of nodes $N'$, it is found empirically that a better guess is given by

$$\frac{V_1}{B} \approx \frac{\rho_0^2 + [N + \tfrac{1}{2}(l+1)]^2\pi^2}{\rho_0^2 + [N' + \tfrac{1}{2}(l+1)]^2\pi^2} \cdot \frac{V_0}{B}. \qquad \text{. . . . (III 22)}$$

## APPENDIX IV

The general formulae given in § 2 may be written more explicitly when the numerical value of $l$ is used. In this appendix the formulae for the observable quantities are summarized for the cases $l = 1$ and $l = 2$. There is no correlation for $l = 0$, and the formulae for $l > 2$ are similar to those given below, but rather more complicated. The $d_{kq}$ tensors for the gamma-ray correlation functions are calculated relative to axes with $z$ along $\mathbf{k}_d \times \mathbf{k}_p$ and $x$ along $\mathbf{k}_d$. They are expressed in terms of the $B_{l\lambda}$ calculated relative to the axes previously defined.

*Case* $l = 1$. Define $B_{10} = a + ib$, $2^{1/2} B_{11} = c + id$, and let

$$Z = \frac{2(bc - ad)}{a^2 + b^2 + c^2 + d^2}, \quad Z \leqslant 1. \qquad \text{. . . . . (IV 1)}$$

Then the differential cross section

$$\frac{d\sigma}{d\Omega} = C(a^2 + b^2 + c^2 + d^2) \qquad \text{. . . . (IV 2)}$$

where $C$ is a constant given by eqn. (9). The polarization

$$P = \frac{(\tfrac{1}{2}\theta_{3/2}^2 - \theta_{1/2}^2)Z}{3(\theta_{3/2}^2 + \theta_{1/2}^2)}. \qquad \text{. . . . (IV 3)}$$

The statistical tensors $d_{00} = 1$, $d_{20} = -\tfrac{1}{2}$.

The attenuation coefficient

$$\lambda = (1 - Z^2)^{1/2} = |d_{22}| \qquad \text{. . . . . . (IV 4)}$$

and the direction of the symmetry axis

$$\tan 2\alpha_{22} = \frac{-2(bd + ac)}{a^2 + b^2 - c^2 - d^2} = \tan 2\phi_0. \qquad \text{. . . (IV 5)}$$

*Case* $l = 2$. Define

$$
\begin{aligned}
B_{20} &= a + ib, & \alpha &= a^2 + b^2, & A &= ac + bd, \\
(2/3)^{1/2} B_{21} &= c + id, & \beta &= c^2 + d^2, & B &= ae + bf, \\
(2/3)^{1/2} B_{22} &= e + if, & \gamma &= e^2 + f^2, & C &= ce + df, \qquad \text{. . . . (IV 6)}
\end{aligned}
$$

and let

$$Z = \frac{3(bc + de - ad - cf)}{\alpha + 3(\beta + \gamma)}, \quad Z \leqslant 1. \qquad \text{. . . (IV 7)}$$

Then the differential cross section

$$\frac{d\sigma}{d\Omega} = D[\alpha + 3(\beta + \gamma)] \qquad \text{. . . . . (IV 8)}$$

where $D$ is a constant given by eqn. (9).    The polarization

$$P = \frac{(\frac{2}{3}\theta_{5/2}{}^2 - \theta_{3/2}{}^2)Z}{3(\theta_{5/2}{}^2 + \theta_{3/2}{}^2)}. \qquad \qquad \text{(IV 9)}$$

The statistical tensors: $d_{00} = 1$

$$d_{20} = \frac{3\gamma - 6\beta - \alpha + 6B}{2[\alpha + 3(\beta + \gamma)]}, \qquad \qquad \text{(IV 10)}$$

$$|d_{22}|^2 = \frac{3}{8} \cdot \frac{[(\alpha - 3\gamma + 2B)^2 + 4(3C + A)^2]}{[\alpha + 3(\beta + \gamma)]^2}, \qquad \text{(IV 11)}$$

$$|d_{44}|^2 = \frac{35}{128} \cdot \frac{[(\gamma - 4\beta + \alpha - 2B)^2 + 16(C - A)^2]}{[a + 3(\beta + \gamma)]^2}. \qquad \text{(IV 12)}$$

The off-diagonal tensor elements:

$$d_{40} = \tfrac{7}{12} + \tfrac{5}{12} d_{20}, \qquad \qquad \qquad \text{(IV 13)}$$

$$d_{42} = -(\tfrac{5}{12})^{1/2} d_{22} \qquad \qquad \qquad \text{(IV 14)}$$

The symmetry axes:

$$\alpha_{42} = \alpha_{22} + \tfrac{1}{2}\pi$$

$$\tan 2\alpha_{22} = \frac{-2(3C + A)}{\alpha - 3\gamma + 2B}, \qquad \qquad \text{(IV 15)}$$

$$\tan 4\alpha_{44} = \frac{4(C - A)}{\gamma - 4\beta + \alpha - 2B}. \qquad \qquad \text{(IV 16)}$$

*Note added in proof.*—The calculations summarized in this paper have been extended to the cases $l = 3$ and $l = 4$ by Dr. H. D. Scott of Liverpool University. He has also written the corresponding Mercury Autocode programmes by modifying the existing $l = 2$ programme. The programme for $l = 0$, 1 and 2 have been translated into Fortran for use on the IBM 7090 computer by Dr. B. Macefield of A.W.R.E., Aldermaston. The computing time for each calculation with these Fortran programmes is approximately $20(l + 1)$ seconds, which is about thirty times faster than the present programmes on the Ferranti Mercury.

## References

BUCK, B., 1960, Thesis, Oxford.
BUCK, B., MADDISON, R. N., and HODGSON, P. E., 1960, *Phil. Mag.*, **5,** 1181.
BUTLER, S. T., 1950, *Phys. Rev.*, **80,** 1095; 1951, *Proc. roy. Soc.* A, **208,** 559.
BUTLER, S. T., and HITTMAIR, O. H., 1957, *Nuclear Stripping Reactions* (Sydney, Australia: Horowitz Publications, Inc.).
DAITCH, P. B., and FRENCH, J. B., 1952, *Phys. Rev.*, **87,** 900.
FRIEDMAN, F. L., and TOBOCMAN, W., 1953, *Phys. Rev.*, **92,** 93.
HOROWITZ, J., and MESSIAH, A. M. L., 1953, *J. Phys. Radium*, **14,** 695, 731; 1954, *Ibid.*, **15,** 142.
HUBY, R., REFAI, M. Y., and SATCHLER, G. R., 1958–59, *Nucl. Phys.*, **9,** 94.
LUBITZ, C. R., 1957, Numerical Table of Butler–Born Approximation Stripping Cross-sections, University of Michigan Report (unpublished).
NEWNS, H. C., 1953, *Proc. phys. Soc., Lond.* A, **66,** 477.
NEWNS, H. C., and REFAI, M. Y., 1958, *Proc. phys. Soc., Lond.*, **71,** 627.
REFAI, M. Y., 1958, Thesis, Liverpool (unpublished).
SATCHLER, G. R., 1960, *Nucl. Phys.*, **18,** 110.
THOMAS, R. G., 1955, *Phys. Rev.*, **100,** 25.
TOBOCMAN, W., 1954, *Phys. Rev.*, **94,** 1655; 1959, *Ibid.*, **115,** 98.
TOBOCMAN, W., and KALOS, M. H., 1955, *Phys. Rev.*, **97,** 132.

# Direct Observation of Antiphase Boundaries in the AuCu₃ Superlattice

By R. M. Fisher

Department of Metallurgy, University of Cambridge

and M. J. Marcinkowski

Edgar C. Bain Laboratory for Fundamental Research, United States Steel Corporation, Research Center, Monroeville, Pennsylvania

## Abstract

Antiphase domains have been revealed for the first time in fully and partially ordered AuCu₃ by transmission electron microscopy of foils prepared by electro-thinning bulk samples. The domains are observed to form a network of rectangular blocks, the boundaries of which lie on cube planes. In addition, it is concluded that alloys annealed for long periods just below the critical ordering temperature consist of imperfectly ordered domains within which the order is homogeneous.

It has been shown both theoretically and experimentally that in order to observe the domain structure, the ordered crystal must be oriented for diffraction contrast by a strong superlattice reflection. All of the various types of domain boundary contrast seen in the electron micrographs can be explained by application of the dynamical theory developed by Whelan and Hirsch for the contrast of stacking faults when the appropriate phase angle and extinction distances for superlattice reflection are introduced. The agreement between theory and experiment is very good.

The extinction distances of the superlattice reflection involved in the domain boundary contrast are found to be about four times that of normal reflections causing stacking-fault contrast. The maximum deviation from the Bragg angle at which the domain boundaries can still be observed is only about one-fourth that for stacking faults. Another consequence of the present theory is that not all of the domain boundaries present can be observed for any one strong superlattice reflection, and this effect causes an apparent intricate maze pattern of antiphase domains in many of the micrographs.

## § 1. Introduction

Copper and gold form a complete series of solid solutions with one another at all compositions. However, alloys at or near the compositions AuCu₃ and AuCu will form an ordered arrangement of atoms when slowly cooled through the critical temperatures of 388 °c and 420 °c, respectively. X-ray superlattice lines for AuCu₃ were first observed by Bain (1923) and in 1925 Johansson and Linde made the first analysis of an ordered structure from its x-ray pattern for the AuCu alloy. Since then hundreds of papers, both experimental and theoretical, have been devoted to an understanding of such ordering phenomena and the resulting effects on physical and mechanical properties of the alloys.

However, all of the various techniques commonly used in light and electron metallography to distinguish the size and shape of non-homogeneous regions within an alloy have up to now failed to reveal the domains in an ordered lattice. Consequently, the extensive literature that has risen over the past thirty years concerning antiphase domains has been obtained from indirect measurements of physical properties or diffraction effects which are sensitive to their size and configuration.

Recently, several investigators have achieved notable advances in studies of domain geometry. By means of direct electron transmission microscopy of thin evaporated films, Ogawa *et al.* (1958) and Glossop and Pashley (1959) have been able to resolve the antiphase boundaries in AuCu (II). Ogawa *et al.* (1959) have also recently obtained direct evidence of antiphase boundaries in gold–copper–zinc alloys, while Kamiya *et al.* (1959) have similarly shown their presence in serpentine. An important feature of the AuCu (II) type structure is that the domains appear to be only about five unit cell lengths (based on the original face-centred cubic lattice) wide, in agreement with the earlier x-ray findings of Johansson and Linde (1936).

Although the results of these investigations are extremely interesting, certain features of the systems chosen and the techniques used limited their application to other cases. In the AuCu and Au–Cu–Zn alloys there is a change of crystal structure during ordering which leads to a large unit cell and results in a complex domain structure. Experimental difficulties of using evaporated films for electron microscopy are also rather large. The most important of these are the uncertainty as to the exact composition and also the relatively fine grain size of the film even when epitaxial growth techniques are used. An additional complication of this technique is that the films are highly oriented, usually with the cube faces of the disordered alloy parallel to the surface of the film. This preferred orientation of the film, together with the fact that any lattice expansion will be easiest along a direction normal to its surface, limits observation of the domain structure to a very narrow range of orientations. These features are discussed by Pashley and Presland (1958–9) in connection with their studies of the transformation of AuCu (I) to AuCu (II).

In view of these considerations the composition $AuCu_3$ was chosen for this investigation and it was decided to heat-treat it to develop the super-lattice while it was in the form of thin strips rolled down from a small ingot. These could be subsequently electro-thinned for microscopy so that the domain structure observed within such specimens should be representative of that in bulk material.

## 1.1. *Antiphase Domain Boundaries in the $AuCu_3$ Type Lattice*

Before discussing the results of this investigation, it will be helpful to review briefly some of the previous work and to point out some of the features of the $AuCu_3$ superlattice.

Of the two classic ordered structures, AuCu and AuCu$_3$, the latter is by far the simpler and most readily understood. It can be described as a simple face-centred cubic lattice in which the corner sites are occupied by gold atoms. Crystallographically, this structure is designated as an Ll$_2$ type lattice composed of four non-equivalent interpenetrating simple cubic lattices. The gold atoms may occur on any of the four non-equivalent sub-lattices during nucleation of small ordered regions in the disordered matrix, and as the ordering transformation proceeds these ordered domains continue to grow until they touch one another. In most cases the two ordered regions will be based on different sub-lattices so that a boundary will be formed at their juncture. Such a boundary is termed an antiphase boundary since the atoms change in phase or step at this point. The size of these domains depends on both the time and temperature of holding below the critical ordering temperature. Fewer nuclei are formed at higher temperatures and these grow more rapidly giving rise to larger antiphase domains. These domains grow until they make contact and the resulting antiphase boundaries form what has been termed a stable 'foam-structure' as further growth requires discontinuous movement of the boundary through distances comparable to the domain dimensions.

The degree of order within the alloy is conveniently expressed in terms of the long-range order parameter, $S$, defined as follows:

$$\left[\frac{A}{I}\right] = \frac{(1+3S)}{16} N$$

where [A/I] denotes the average number of A atoms on type I sites for a given $S$, and $N$ represents the total number of atoms within the crystal. For complete disorder $S = 0$, whereas for perfect order $S = 1$. The value of $S$ can be determined from x-ray methods as described in the following sections.

X-ray investigations by Wilchinsky (1944) and also by Keating and Warren (1951) on AuCu$_3$ indicated that the long-range order parameter, $S$, changes abruptly from 0 to 0·8 between specimens annealed just above and just below the critical ordering temperature. As the temperature of annealing is decreased still further towards room temperature and if sufficient time is allowed, $S$ becomes equal to one, indicating nearly perfect long-range order. In order to explain these results, Keating and Warren postulated that below the critical ordering temperature, $S$ increases because the order changes homogeneously within the specimen (within the antiphase domains) and not because of a change in the relative amounts of ordered and disordered phases.

Wilson (1949) and Griffoul and Guinier (1948) using x-ray diffraction, and Raether (1952) using electron diffraction, have all postulated that the antiphase domain boundaries in AuCu$_3$ lie on cube faces. On this basis it is of interest to consider in detail the manner in which such boundaries can be formed. Referring to fig. 1† which shows the unit cell of the AuCu$_3$

---

† Figures 2, 3, 5, 8, 9 and 10 are shown as plates.

superlattice, all of the gold atoms occupy type I sites whereas the type II, III and IV sites are occupied by copper atoms and will therefore be designated as a type I domain. If the gold atoms in an adjacent cell occur on sites other than type I, an antiphase boundary is formed between the two cells. There will, in general, be two unique ways of forming boundaries on cube planes. The first or type 1 boundary can be formed by a shear of the type $\frac{1}{2}a\langle 110 \rangle$ on any of the cube faces and is shown in table 1 for all six cube faces. Furthermore, any of the four possible shears on the $\pm (100)$ face displaces a type I site into a position formerly occupied by a type III site. This operation is equivalent to placing an A atom on a type III site in the domain adjacent to the one shown in fig. 1 bounded by the $\pm (100)$ planes. An important feature of the type 1 boundary is that it does not involve a net change in nearest-neighbour atom types across this boundary and is thus expected to be of very low energy.

Fig. 1
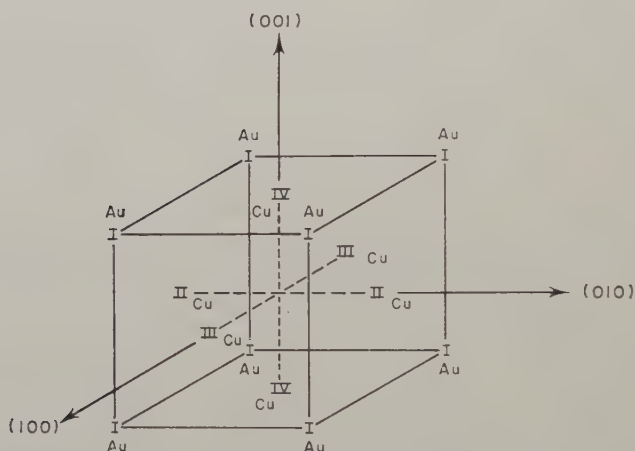


Analysis of domains in $AuCu_3$ type alloys in terms of four non-equivalent sub-lattices.

The second way of forming the domain boundaries on cube faces is as follows. First remove one of the cube planes that contains either equal numbers of gold and copper atoms or all copper atoms shown in fig. 1. Then bring the two atom planes bordering the vacant plane together by a shear of $\frac{1}{2}a\langle 110 \rangle$ in a direction of $45°$ to the cube plane. This operation involves an increase in the number of nearest-neighbour atom types across the boundary and is expected to be of somewhat higher energy than the type 1 boundary. The detailed analysis of all the possible displacements producing boundaries of this type is shown in table 2 along with their equivalent sub-lattice occupancy. It will be convenient to designate these as type 2 boundaries.

It can be seen therefore that the operation that characterizes an antiphase domain boundary in the AuCu$_3$ type superlattice is a shear of the type $\frac{1}{2}a\langle 110\rangle$.

Table 1.   Type 1 boundary

| Face | Shear displacement | Domain type | Equivalence in terms of sub-lattice occupancy in adjacent domain |
|---|---|---|---|
| $\pm(100)$ | $\pm\frac{1}{2}a\,[011]$ <br> $\pm\frac{1}{2}a\,[01\bar{1}]$ | III | Au on III |
| $\pm(010)$ | $\pm\frac{1}{2}a\,[\bar{1}01]$ <br> $\pm\frac{1}{2}a\,[101]$ | II | Au on II |
| $\pm(001)$ | $\pm\frac{1}{2}a\,[110]$ <br> $\pm\frac{1}{2}a\,[\bar{1}10]$ | IV | Au on IV |

Table 2.   Type 2 boundary

| Face | Shear displacement | Domain type | Equivalence in terms of sub-lattice occupancy in adjacent domain |
|---|---|---|---|
| $\mp(100)$ | $\frac{1}{2}a\,[\overset{\pm}{\bar{1}}01]$ <br> $\frac{1}{2}a\,[\overset{\pm}{\bar{1}}0\bar{1}]$ | II | Au on II |
| | $\frac{1}{2}a\,[\overset{\pm}{\bar{1}}\bar{1}0]$ <br> $\frac{1}{2}a\,[\overset{\pm}{\bar{1}}10]$ | IV | Au on IV |
| $\mp(010)$ | $\frac{1}{2}a\,[0\overset{\pm}{\bar{1}}1]$ <br> $\frac{1}{2}a\,[0\overset{\pm}{\bar{1}}\bar{1}]$ | III | Au on III |
| | $\frac{1}{2}a\,[1\overset{\pm}{\bar{1}}0]$ <br> $\frac{1}{2}a\,[\bar{1}\overset{\pm}{\bar{1}}0]$ | IV | Au on IV |
| $\mp(001)$ | $\frac{1}{2}a\,[\bar{1}0\overset{\pm}{\bar{1}}]$ <br> $\frac{1}{2}a\,[10\overset{\pm}{\bar{1}}]$ | II | Au on II |
| | $\frac{1}{2}a\,[01\overset{\pm}{\bar{1}}]$ <br> $\frac{1}{2}a\,[0\bar{1}\overset{\pm}{\bar{1}}]$ | III | Au on III |

Note that upper sign of index in first column must go with upper sign of index in second column and similarly with the lower sign.

## § 2. Experimental Procedure

Fifty grams of copper wire of 99·9% purity and an equal weight of gold sheet of 99·98% purity were melted under vacuum in a zirconia crucible. The resulting ingot was alternately annealed and rolled into strips about 0·0015 in. thick. Chemical analysis showed the strips to contain 24·4 at. % (50 wt. %) gold. In order to grow large grains, lengths of the strip were sealed in evacuated Vycor tubes, annealed for two hours at 900°C and air cooled. The resulting mean grain diameter was 0·1 mm and subsequent chemical analysis showed no detectable loss in either copper or gold due to vaporization. The sealed specimens were divided into three groups, heated to 500°C and held for 15 min. One group of specimens was water-quenched to maintain them in the disordered condition. A second group was then cooled to 380°C and annealed at this temperature for 75 hours. Finally, in order to produce a high degree of order in the remaining specimens, they were slowly cooled over a period of several hours from 500° to 400°C, and then from 400° to 181°C at a rate of 2·3°C/hr.

Thin foils suitable for transmission electron microscopy were prepared by electropolishing square sections 15 mm on an edge simultaneously from both sides until numerous holes appeared in the centre. The procedure used is a modification of that developed by Bollmann (1956) and has been described by Fisher and Szirmae (1959). Small pieces were cut from the edges of these holes and mounted for electron microscopy. Choice of a suitable electrolyte for polishing $AuCu_3$ proved to be a major difficulty. After many trials, the one found to be most successful consisted of 25 g of chromium trioxide, 133 ml of glacial acetic acid and 7 ml of distilled water. Stainless-steel cathodes were used, and the cell voltage, temperature of the electrolyte and polishing time were 25 v, 22°C and 45 min, respectively. Macroscopically and even microscopically a good polish was always obtained, but under the electron microscope many of the specimens exhibited a matt surface probably caused by a slight etching by the polishing solution. In this respect, the electrolyte appeared to be quite erratic and only a few of the many attempts at preparing foils were successful. However, the results on various specimens given the same heat treatment were in good agreement.

The electron microscopy and diffraction observations were made with a Siemens Elmiskop I operating at 100 kv. In forming the image, an objective aperture of 50 μ was used, so that no diffracted rays were allowed to contribute to the image. Selected area diffraction patterns were obtained using intermediate apertures of 50 and 20 μ which gave diffraction patterns of selected areas corresponding to 2 and 0·9 μ in diameter respectively.

## § 3. Discussion and Results

### 3.1. *Preliminary X-ray Examination of Ordered Specimens*

The two ordering anneals described previously were designed to produce two different ordered configurations. The anneal for 75 hours at 380°C

was made to produce an intermediate configuration of order consisting of very large domains ($\simeq 1000\,\text{Å}$) within which the long-range order, $S$, was less than one. According to the results of Keating and Warren (1951) $S$ in this case is about 0·8.

On the other hand, the treatment given to the group of specimens slowly cooled through the ordering temperature was designed to give a large domain size (although somewhat smaller than on the previous anneal) with an almost perfect degree of order within the domains. The effectiveness of this latter treatment was checked by examining one of the ordered specimens by conventional x-ray techniques to determine the intensity and shape of the superlattice reflections.

The degree of long-range order $S$ can be determined from the following expression proposed by Keating and Warren (1951):

$$S^2 = \left[\frac{p_\text{s}}{p_\text{f}}\right] \frac{[mF^2 \exp(-2\mu)(1+\cos^2 2\theta)/\sin^2\theta\cos\theta]_\text{f}}{[mF^2 \exp(-2\mu)(1+\cos^2 2\theta)/\sin^2\theta\cos\theta]_\text{s}} \quad . \quad . \quad (1)$$

where $[p_\text{s}/p_\text{f}]$ is the ratio of the intensity of the superlattice reflection to that of a fundamental reflection, $m$ is the multiplicity, $F$ is the structure factor, $\mu$ is the Debye temperature factor and is equal to $8\pi^2 \sin^2\theta\langle u^2\rangle_\text{av}/\lambda$. $\langle u^2\rangle_\text{av}$ is the mean square atomic displacement, $\lambda$ is the wavelength of the x-rays and $\theta$ is the Bragg angle of reflection. By this technique $S$ was found to be 1·1 as compared to 1·0 for perfect long-range order and consequently it is justifiable to assume that the slowly cooled samples possess essentially perfect long-range order.

From the relative breadth of the superlattice lines, the antiphase domain size can be estimated using the well-known Scherrer (1920) expression

$$t = \frac{0\cdot 9\,\lambda}{\beta \cos \theta} \qquad . \quad . \quad . \quad . \quad . \quad . \quad (2)$$

where $\beta$ is the angular broadening of the superlattice reflections after correction for the instrument broadening and $\theta$ is the Bragg angle. This expression can be used because, except for x-rays scattered by atoms just on each side of the boundary between two domains, the phase difference between x-rays scattered in different domains is random for most of the diffracted x-ray intensity. This simple 'particle size' line broadening method of determining domain size has been used previously by Sykes and Jones (1936) and others and found to agree well with the more precise analysis by Wilson (1943).

Although various ways of evaluating $\beta$ have been used, the most appropriate method appears to be that first proposed by Taylor (1941) where

$$\beta = [(B-b)\sqrt{(B^2-b^2)}]^{1/2}. \qquad . \quad . \quad . \quad . \quad (3)$$

$B$ is the angular width of the superlattice reflection at one-half maximum intensity, while $b$ is the width of a corresponding principal reflection at one-half maximum intensity. From eqns. (2) and (3), $t$ was found to be $495 \times 10^{-8}$ or about $500\,\text{Å}$, as is to be expected considering the relatively long ordering treatment given to the specimens during slow cooling.

### 3.2. *Direct Observation of Antiphase Domains by Electron Microscopy*

The electron micrograph in fig. 2 shows the antiphase domain con-figuration in a sample of $AuCu_3$ which was annealed 75 hours at $380°c$ to produce an intermediate state of order. In this micrograph the antiphase domain boundaries appear darker than the background except in the upper right corner where they are lighter. The boundaries may show various types of contrast depending on the local thickness and orientation of the foil, as will be discussed in detail in a following section. The narrow regions correspond to boundaries perpendicular to the foil whereas the broad areas correspond to boundaries nearly in the plane of the foil.

The boundaries may be seen to make up a network of square or rectangular blocks and in general they are arranged such that four domains meet at a corner. The average domain diameter was determined on several different areas including that shown in fig. 2 by making random lineal analysis traverses on these areas. This procedure gives a value of about 750 Å, for the average domain size.

Similarly, fig. 3 shows the antiphase domain structure of a specimen which was slowly cooled so that it would be fully ordered. The most striking feature of this structure is the apparent complex maze pattern formed by the domain boundaries. For example, the domain indicated by the letter A appears to wind through approximately one-eighth of the area shown in fig. 3. This complex maze pattern however is to a large extent an artefact, as will be explained below, and arises from the absence of contrast of some domain boundaries under certain conditions. A measurement of the average domain size of fig. 3 in a manner similar to that performed on fig. 2 gives a value of about 475 Å, which is in good agreement with the x-ray results on this same specimen. It appears therefore that the x-ray technique described above is suitable to obtain a good estimate of the domain dimensions. Another important feature of both figs. 2 and 3 is that these antiphase domains appear to be contiguous with one another; i.e. there is no indication of co-existing ordered and disordered regions. It therefore appears reasonable to conclude that the degree of order increases homogeneously within the domains in $AuCu_3$ as it is slowly cooled below the critical ordering temperature.

The crystallographic planes containing the domain boundaries can be identified by analysis of the electron diffraction pattern obtained from the area shown in fig. 2, which indicates that the [001] pole is normal to the plane of the foil. From the known angular rotation between the diffraction pattern and image due to the difference in current in the intermediate lens of the microscope when adjusted for diffraction or microscopy, the plane traces corresponding to (010) and (100) planes could be determined.

As shown in the lower left corner of fig. 2, the two prominent sets of boundaries lie very close to the (100) and (010) traces and are thus nearly perpendicular to the plane of the foil. The results of a similar analysis of the area shown in fig. 3 are shown by the plane traces as marked. Here

the foil was oriented so that its normal was a $[\bar{1}2\bar{1}]$ pole so that three sets of traces must be considered, but again it can be seen from this figure that two prominent sets of boundaries lie very close to (100) and (001) traces. These results are in agreement with the x-ray diffraction studies of Wilson (1949) and Griffoul and Guinier (1948) and also the electron diffraction analysis of Raether (1952) all of which suggest that the antiphase boundaries lie on {100} planes in $AuCu_3$.

The apparent width of the domain boundaries in fig. 3 is partly due to the fact that the micrograph shows their projections on to the plane of the foil. The (100) and (001) planes make angles of approximately 24° with the normal to the $(\bar{1}2\bar{1})$ whereas the $(0\bar{1}0)$ planes make angles of approximately 55°. These latter boundaries are rather infrequent since they lie more nearly in the plane of the foil and its thickness is comparable to the dimensions of the domains.

### 3.3. *Conditions for Producing Antiphase Boundary Contrast in AuCu₃*

The contrast of antiphase boundaries in electron micrographs of AuCu II has been attributed by Pashley and Presland (1958–9) to interference between the undeviated beam and satellites arising from secondary diffraction due to the periodic arrangement of the antiphase boundaries. Ogawa *et al.* have expressed this same view. This condition does not apply to $AuCu_3$, but a satisfactory explanation for the various types of contrast observed can be achieved by modifying the dynamical electron diffraction theory of Whelan and Hirsch (1957) for the contrast of stacking faults to apply to the case of an antiphase domain boundary†.

Whelan (1958) has recently reviewed in detail the mechanism of diffraction contrast in transmission electron micrographs, the essential features of which are illustrated in fig. 4. The transmitted and diffracted waves vary in intensity periodically with depth in the crystal as shown such that the incident wave is reflected completely at a depth $t_0/2$ where $t_0$ is the extinction distance. The actual value of $t_0$ depends on the wavelength of the electron beam and the interplanar spacing and structure factor of the Bragg reflection involved. The diffracted wave is normally blocked by the objective aperture and only the transmitted wave allowed to contribute to the image (bright field).

In foils with considerable thickness, or of material of high atomic number, multiple scattering and absorption modify the intensity variations so that they do not go completely to zero. These effects will not be considered in detail in this discussion.

The transmitted intensity through a perfect crystal for unit incident amplitude is given by the dynamical theory as

$$\xi = 1 - \frac{\sin^2\left[\pi(t/t_0)\sqrt{(1+x^2)}\right]}{1+x^2} \qquad \cdot \quad \cdot \quad \cdot \quad \cdot \quad \cdot \quad (4)$$

---

† It has been pointed out to us that Pashley and Presland suggest that the contrast of domain boundaries is effectively that of stacking faults.

where $t_0$ is as given above, $t$ is the thickness of the crystal and $x$ is a parameter related to the deviation of the incident beam from the exact Bragg angle for the reflection giving contrast. Thus, the depth periodicity of the maxima in transmitted intensity is given by

$$t' = \frac{t_0}{\sqrt{(1+x^2)}}, \qquad \qquad \cdots \quad \cdots \quad (5)$$

which corresponds to interference fringes normal to the thickness gradient in the crystal such as at the edge of wedge-shaped crystals or at grain boundaries, since in general there will not be a specific orientation relationship between the two grains.

Fig. 4
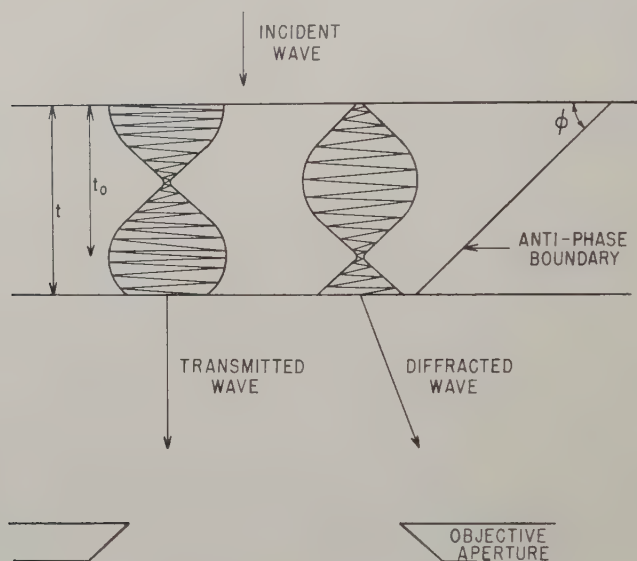


Schematic illustration of diffraction contrast in thin foils. Intensity of transmitted and diffracted waves vary periodically with thickness of perfect crystal. Electrons diffracted above and below antiphase boundary are out of phase by $\alpha = 2\pi\mathbf{g} \cdot \mathbf{R}$ where $\mathbf{g}$ and $\mathbf{R}$ are reciprocal lattice and displacement vectors respectively.

Whelan and Hirsch have considered the general case of a crystal containing a surface discontinuity and showed that the diffracted intensity function for a perfect crystal obtained from eqn. (4) will be modulated by a term of the form

$$\exp\left(-2\pi i\alpha\right) \qquad \cdots \quad \cdots \quad \cdots \quad (6)$$

where $\alpha$ is the phase difference between rays diffracted on either side of the boundary fault. The phase angle, $\alpha$, is given by

$$\alpha = 2\pi\mathbf{g} \cdot \mathbf{R} \qquad \cdots \quad \cdots \quad \cdots \quad (7)$$

where **g** is the reciprocal lattice vector of the diffracted wave *hkl* and **R** is the displacement vector between the two planes bounding the fault in the crystal.

As shown by Whelan and Hirsch for the case of stacking faults in f.c.c. metals and alloys, **R** is $\frac{1}{6}a\langle 112\rangle$ and $\alpha$ therefore is 0 or $\pm\frac{2}{3}\pi$, depending on the orientation of the crystal. No contrast effects are observed when the phase angle is 0 as the modulation term becomes equal to unity.

Now we have previously seen that an antiphase domain boundary in the AuCu₃ type lattices could be thought of in a similar manner; that is the displacement **R** of one part of the crystal with respect to the other is a shear of $\frac{1}{2}a\langle 110\rangle$. Thus, from eqn. (7) for the principal Bragg reflections, i.e. *hkl* unmixed, the phase angle is 0 or $\pm 2\pi$, which is equivalent to no discontinuity in the crystal and the boundaries are not visible. For superlattice reflections, however, the phase angle is 0 or $\pm\pi$ depending on the particular combination of **g** and **R**. Therefore, it is apparent that for domain boundaries to be observed, the crystal must be oriented for diffraction contrast by a strong superlattice reflection and of such a type and orientation that $\alpha$ is not equal to 0. This conclusion is verified by the micrographs in figs. 5 (*a*) and (*b*) showing strong extinction contours. The domains are visible within the superlattice 110 reflection extinction contour shown in fig. 5 (*a*); whereas, they are not in the principal 200 reflection extinction contour in fig. 5 (*b*).

Selected area diffraction analysis of other areas showing domain contrast verified that these also were oriented close to a strong superlattice reflection.

Dark-field observations wherein the image was obtained using the intensity diffracted into a 110 reflection, also supported the contrast criteria described above.

### 3.4. *Interpretation of the Apparent Maze Pattern Configuration of the Antiphase Domains*

In many of the micrographs, the domains appear to form a complex maze pattern as in figs. 3, 8 (*a*) and 10 rather than the expected foam-type structure composed of rectangular blocks shown in fig. 2. The explanation for this appearance is that, as mentioned previously, the phase angle, $\alpha$, may be equal to zero for certain combinations of domain boundary type and superlattice reflection so that such boundaries will not be visible.

Thus, since for domain boundary contrast $\alpha$ must be $= \pm\pi$ and since

$$\alpha = \pi\langle 110\rangle . (hkl)$$

it is possible to predict the contrast for various cases. The results of detailed analysis of the contrast for antiphase boundary types listed in tables 1 and 2 for certain combinations of *hkl* for superlattice reflections are listed in table 3. It is apparent from the table that one-third of the possible antiphase boundaries will not be visible for any particular

reflection. The manner in which this effect can cause the same domain structure to show three apparently different configurations is illustrated in figs. 6 (*a*) and (*b*). In these figures the arrangement of antiphase domains is identical in both cases and consists of a two-dimensional array of equal numbers of type I, II, III and IV domains distributed at random such

## Table 3

| Indices that are of same type (either both odd or both even) | Boundaries that show contrast | Boundaries that do not show contrast | Faces on which boundaries lie | Type of boundary |
|---|---|---|---|---|
| *h* and *k* | I–II (IV–III) | | (100) | 2 |
| | ,, ,, | | (010) | 1 |
| | | | (001) | 2 |
| | I–III (IV–II) | | (100) | 1 |
| | ,, ,, | | (010) | 2 |
| | ,, ,, | | (001) | 2 |
| | | I–IV (II–II) | (100) | 2 |
| | | ,, ,, | (010) | 2 |
| | | ,, ,, | (001) | 1 |
| *h* and *l* | I–III (IV–II) | | (100) | 1 |
| | ,, ,, | | (010) | 2 |
| | | | (001) | 2 |
| | I–IV (III–II) | | (100) | 2 |
| | ,, ,, | | (010) | 2 |
| | ,, ,, | | (001) | 1 |
| | | I–II (IV–III) | (100) | 2 |
| | | ,, ,, | (010) | 1 |
| | | ,, ,, | (001) | 2 |
| *k* and *l* | I–II (IV–III) | | (100) | 2 |
| | ,, ,, | | (010) | 1 |
| | | | (001) | 2 |
| | I–IV (III–II) | | (100) | 2 |
| | ,, ,, | | (010) | 2 |
| | ,, ,, | | (001) | 1 |
| | | I–III (IV–II) | (100) | 1 |
| | | ,, ,, | (010) | 2 |
| | | ,, ,, | (001) | 2 |

that no two neighbouring domains are identical. The third possibility with *k* and *l* both even or odd is not illustrated. This model is in agreement with what is actually to be expected and which was discussed previously. First, it will be noted that the heavy dark lines in this series of figures, which represent those antiphase boundaries that show contrast, form a maze pattern in surprisingly good agreement with the experimental observations (fig. 3). Secondly, it will be noted that the antiphase domain boundaries

that show contrast enclose a superdomain within which all of the boundaries that do not show contrast are identical. In fig. 6 (*a*), for example, two different types of superdomain are present, those within one consisting solely of type II–III boundaries while those within the

Fig. 6
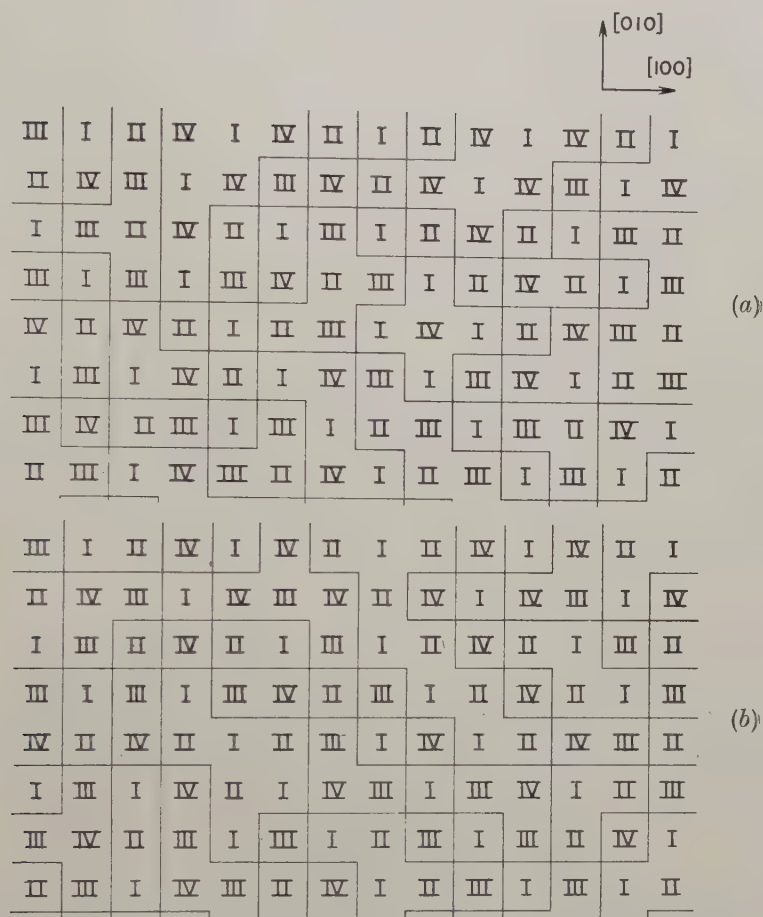


(*a*) Antiphase domain boundary contrast arising from *hkl* super-lattice reflection where both *h* and *k* are either even or odd. (*b*) Antiphase domain boundary contrast arising from *hkl* superlattice reflection where both *h* and *l* are either even or odd.

other are boundaries of the type I–IV; thus, the faces of any one superdomain are entirely bounded by superdomains of the other type. Similar conclusions hold for the domains showing contrast from the other two types of superlattice reflection, one of which is shown in fig. 6 (*b*).

The three permutations of the superlattice reflection *hkl* not only give rise to three vastly unique antiphase domain contrasts, but should also enable us to distinguish between type 1 and type 2 domain boundaries within the ordered lattice. To date, attempts to obtain contrast in a particular area with one superlattice reflection and then to tilt it for contrast with a different reflection were not successful. A precision two-goniometer stage in the microscope will be required for this type of experiment.

In the present investigation, we have interpreted the antiphase domain boundary contrast as originating from a single strongly diffracted super-lattice reflection. It is only for this special case that the dynamical theory of Whelan and Hirsch is strictly applicable. In most cases the present work showed that indeed only one strong superlattice reflection was present, as determined from the selected area diffraction patterns of the regions showing domain boundary contrast. However, in a few cases, there were several superlattice reflections or a superlattice reflection along with a principal reflection. For example, figs. 2 and 10 show a number of very faint domain boundaries which have a tendency to eliminate the maze patterns discussed in the previous section and thus give rise to the nearly complete antiphase domain boundary structure. These faintly appearing boundaries are thought to arise from very weak superlattice reflections possessing a different set of indices than that of the stronger reflections, and may arise from the small but finite divergence of the electron beam. Nevertheless, in general, the domain contrast observed was in good agreement with those expected for a single superlattice reflection.

### 3.5. *Extinction Distances in AuCu$_3$ Type Alloys*

In order to analyse theoretically the expected intensity profiles of the antiphase boundaries in AuCu$_3$ it is necessary to evaluate the extinction distances of both the principal and the superlattice reflections; the extinction distance $t_0$ for any particular reflection is given to a good approximation by Whelan and Hirsch (1957)

$$t_0 = \frac{\lambda E}{V_g} \qquad \qquad \cdots \cdots \cdots (8)$$

where $E$ is the accelerating voltage of the electron beam, $\lambda$ the wavelength and $V_g$ the lattice potential in volts along the crystal direction of interest.

Heidenreich (1949) has developed an expression to obtain $V_g$ using the Born approximation to obtain the atomic form factor for electrons from the tabulated x-ray atomic scattering factors. Recently, however, Ibers (1958) has computed electron scattering factors directly using Thomas–Fermi–Dirac potentials so that the approximation mentioned is not necessary. With this and other appropriate substitutions the value of $V_g$ is given by

$$V_g = \frac{600h^2}{\pi m e} \frac{d_g{}^2}{V} \frac{\sin^2\theta}{\lambda^2} \sum f_j \exp\left(-2\pi i \mathbf{g} \cdot \mathbf{r}_j\right) \qquad \cdots \cdots (9)$$

where $h$ is Plank's constant, $m$ the mass of the electron, $e$ electronic charge, $V$ volume of unit cell, $d_g$ interplanar spacing giving rise to Bragg reflection **g** at Bragg angle $\theta$, $f_j$ is the electron scattering factor for the $j$th atom located at $\mathbf{r}_j$ in the unit cell.

Table 4.   Extinction distances in ordered AuCu₃ for 100 kv electrons.
$\lambda = 0\cdot037$ Å

| Reflection | $t_0(S=0)$ Å | $t_0(S=1)$ Å | $t_0(S=0\cdot8)$ Å |
|:---:|:---:|:---:|:---:|
| 100† | ∞ | 860 | 1080 |
| 110† | ∞ | 1030 | 1290 |
| 111 | 229 | 229 | 229 |
| 200 | 263 | 263 | 263 |
| 210† | ∞ | 1460 | 1830 |

† Superlattice reflections.

In the case of the AuCu₃ structure, there are four atoms in the unit cell of volume $a_0{}^3$, as shown in fig. 1, and for perfect order the gold atoms are located at $(0, 0, 0)$ and the copper atoms at $(\frac{1}{2}, \frac{1}{2}, 0)$, $(\frac{1}{2}, 0, \frac{1}{2})$ and $(0, \frac{1}{2}, \frac{1}{2})$. If the order is not perfect, i.e. long-range order parameter less than 1, the occurrence of gold and copper atoms in the designated site is modified by a probability factor.   The summation term in eqn. (9) is, of course, the structure factor, $F$, and it can be shown that for an arbitrary degree of order $S$

$$F_F = f_{Au} + 3f_{Cu} \text{ for } hkl \text{ unmixed} \qquad . \quad . \quad . \quad (10\,a)$$

and

$$F_S = S[f_{Au} - f_{Cu}] \text{ for } hkl \text{ mixed} \qquad . \quad . \quad . \quad (10\,b)$$

where the subscripts F and S refer to the fundamental and superlattice structures, respectively.   $t_0$ can therefore be written as

$$t_0 = \frac{\pi\lambda^3 E a_0{}^3 m e}{600 h^2 d_g{}^2 \sin^2\theta}\left(\frac{1}{F}\right). \qquad . \qquad . \quad . \quad (11)$$

From eqns. (10) and (11) it can be seen that values of $t_0$ corresponding to superlattice reflections will be much greater than those corresponding to the fundamental reflections.   This difference will be greater the smaller the difference between $f_{Au}$ and $f_{Cu}$ and/or as $S \to 0$.   Table 4 lists some extinction distances computed for AuCu₃ for 100 kv electrons when $S$ is 0, 1 and 0·8.   It should be noted that $F_S$ for this alloy is much larger than that encountered in most superlattices, and the corresponding extinction distances much less.   The $t_0$ values for the principal reflections in the alloy lie between those of pure copper and pure gold, but much closer to that for copper.

**3.6.** *Application of the Detailed General Dynamical Theory of Electron Diffraction to the Case of Antiphase Domain Boundaries in $AuCu_3$ Type Alloys*

Whelan and Hirsch have developed the following equation for the wave function intensity of the transmitted electron beam based on the dynamical theory of diffraction

$$\xi = \left[ \cos \beta_1 + \frac{\sin^2 \alpha/2}{(1+x^2)} (\cos \beta_2 - \cos \beta_1) \right]^2$$
$$+ \left[ \frac{\sin \alpha/2 \cos \alpha/2}{(1+x^2)} (\cos \beta_2 - \cos \beta_1) - \frac{x}{\sqrt{(1+x^2)}} \sin \beta_1 \right]^2 \qquad (12)$$

where

$$\beta_1 = \frac{\pi t \sqrt{(1+x^2)}}{t_0} \qquad \qquad \cdot \quad \cdot \quad \cdot \quad \cdot \quad \cdot \quad (13\,a)$$

and

$$\beta_2 = \frac{2\pi Z \sqrt{[(1+x^2)]}}{t_0} \qquad \qquad \cdot \quad \cdot \quad \cdot \quad \cdot \quad (13\,b)$$

where $t$ is the thickness of the film and $Z$ is the distance measured from the centre of the film. For the antiphase domain boundaries in the $AuCu_3$ type crystals $\alpha = \pm \pi$ for the superlattice reflections and eqn. (10) simplifies to

$$\xi = A_1 + A_2 \cos \beta_2 + A_3 \cos^2 \beta_2 \qquad \cdot \quad \cdot \quad \cdot \quad \cdot \quad (14)$$

where

$$A_1 = \left[ 1 - \frac{1}{(1+x^2)} \right]^2 \cos^2 \beta_1 + \left[ \frac{x^2}{1+x^2} \right] \sin^2 \beta_1, \quad \cdot \quad \cdot \quad (15\,a)$$

$$A_2 = 2 \left[ \frac{1}{(1+x^2)} - \frac{1}{(1+x^2)^2} \right] \cos \beta_1, \qquad \qquad \cdot \quad \cdot \quad \cdot \quad (15\,b)$$

$$A_3 = \frac{1}{(1+x^2)^2}. \qquad \qquad \cdot \quad \cdot \quad \cdot \quad \cdot \quad \cdot \quad \cdot \quad (15\,c)$$

Both $A_1$ and $A_2$ are seen to be functions of $x$ and $\beta_1$ whereas $A_3$ is a function only of $x$. $\xi$ is periodic with the period $2\pi$ in both $\beta_1$ and $\beta_2$ and is shown plotted in fig. 7 as a function of $\beta_2$ for several values of $t$ and $x$. It is seen that, in general, the intensity function consists of alternate strong and weak maxima. Unlike the case for stacking faults in f.c.c. lattices, the intensity profiles in the present case are identical for positive and negative values of $x$ and are thus symmetrical about $x = 0$. The intensity on either side of the antiphase domain boundary (unfaulted material) is shown by arrows in fig. 7 and is merely that value of the transmitted intensity obtained by substituting $\alpha = 0$ in eqn. (12) and which leads to eqn. (4). The intensity profiles in fig. 7 have been plotted for a complete period of $2\pi$. However, that portion of the cycle which can actually be obtained for a given $t$ and $x$ is shown by a solid curve; whereas the remainder of the cycle is shown dotted. The angles shown in the lower left-hand corner of each block indicate how much of the intensity cycle can actually be observed for the given $x$ and $t$.

Fig. 7
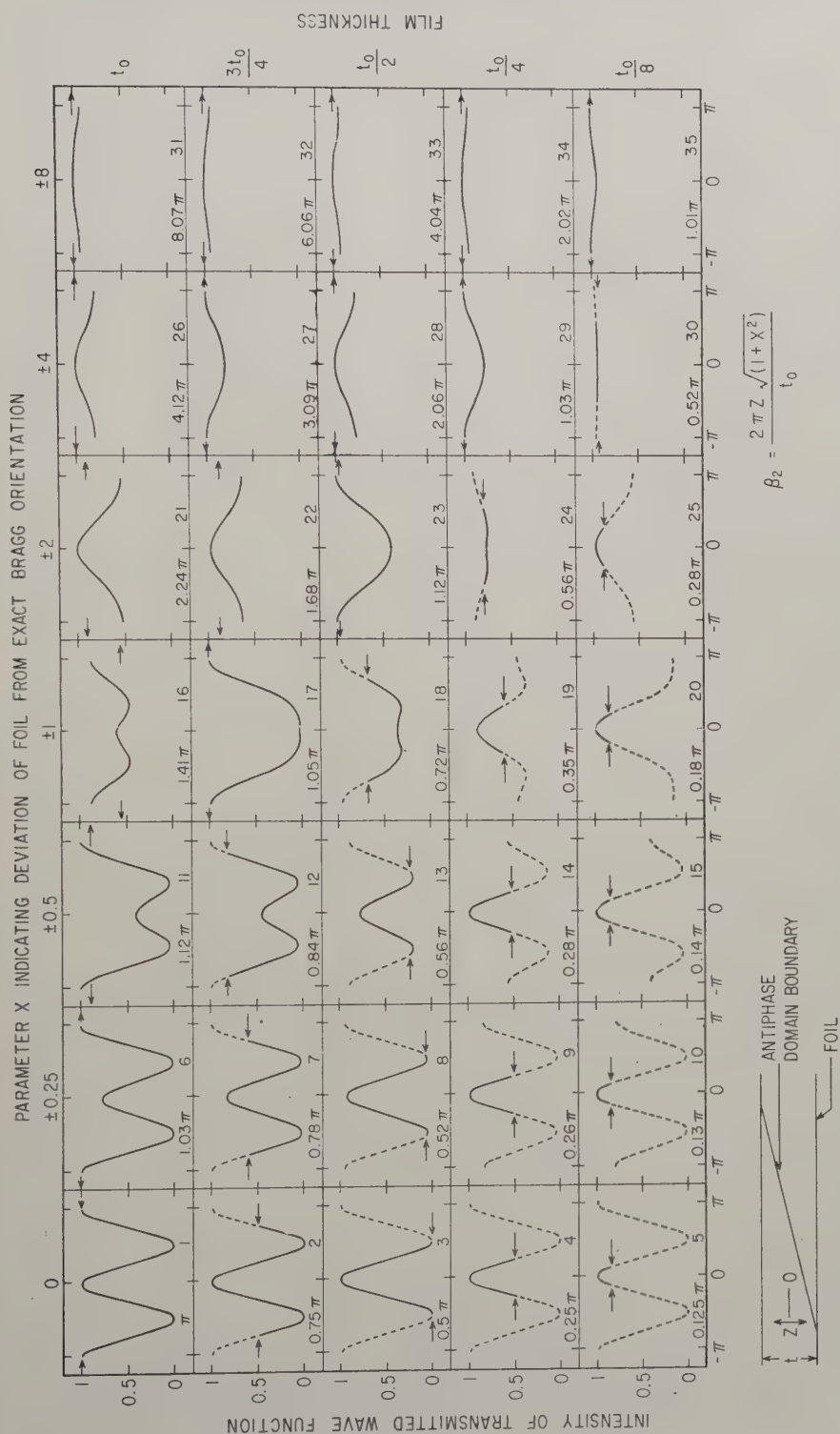
Intensity profiles of the domain boundary shown in the lower left as a function of foil thickness and orientation.

In the case where $x = 0$, $A_1$ and $A_2$ will be zero and the dark fringes will be equally spaced at a distance on the film surface given by

$$\Delta S = t' \cot \phi \qquad \cdots \cdots \cdots \quad (16)$$

where $t' = t_0/2$ and $\phi$ is the angle between the plane of the film and the plane on which the antiphase domain boundary lies. It is seen that $t_0$ in the case of the superlattice reflections is about four times that of the principal reflections. Therefore, the number of fringes associated with the boundary are expected to be small and even zero in many cases, which is in great contrast to the multiple fringes that are observed for stacking faults. Even in the case where $t = t_0$ ($\simeq 1000$ Å) and $x = 0$ only a single pair of dark fringes is to be expected, while for $t = t_0/2$ ($\simeq 500$ Å) no fringes will be observed. Instead, the boundary will appear as a solid white line. The majority of the boundaries in fig. 3 exhibit almost solely this type of contrast. On the other hand, the majority of boundaries in fig. 10 consist of a pair of dark fringes and is believed to represent the condition in which $t \simeq t_0$.

Consider now the manner in which the domain boundary contrast changes as $t$ varies and $x$ remains constant. This condition is often realized near the edge of the foil. In particular, fig. 8 ($a$) shows the manner in which the boundary contrast changes as the edge of the foil is approached (top of figure). In this case $x$ is thought to be about $0 \cdot 5$. Six unique types of domain boundary contrast are shown in this figure (the areas of which are labelled 1–6). The intensity profiles determined from eqn. (14) for $x = 0 \cdot 5$ and the various values of $t$ thought to correspond to these six regions are shown in fig. 8 ($b$) where the number in the lower right-hand corner of each block corresponds to the numbers of fig. 8 ($a$). In addition, the variation of the transmitted intensity within the domains as determined by eqn. (4) is shown in fig. 8 ($c$). This detailed comparison between the observed and the theoretical domain boundary profiles is found to be quite good.

Consideration will now be given to the variation of the intensity profiles with the deviation from the exact Bragg angle as defined by the parameter $x$. As $|x|$ increases, $A_3$ becomes negligible compared with $A_2$ and $\xi$ begins to approach a pure cosine function as shown in fig. 7. In addition, it will be noted that contrast reversals occur for certain $x$ values. In order to determine the values at which these reversals take place consider first that at $\beta_1 = n \pm \pi/2$, $A_2$ becomes zero and the boundary contrast is one of equally spaced fringes. On either side of this angle, i.e. $n$ and $n \pm \pi$, the contrast is reversed. Because of the large value of $t_0$, the reversals take place over relatively large values of $x$ as compared with stacking faults. In addition, as $t$ decreases, the frequency of reversals becomes even smaller for a given deviation from the exact Bragg angle. Also, as $|x|$ increases, the fringe spacing decreases according to eqn. (5).

Figure 9 ($a$) shows very vividly the way in which contrast reversals of the domain boundaries take place as the orientation of the foil changes. This apparently single contour however is believed to consist of two partially

overlapping superlattice extinction contours of the type 110 and $\bar{1}\bar{1}0$. Examination of a selected area diffraction pattern within the contour showed two equally intense reflections of this type and since both these superlattice reflections are only about 1·5° from one another, it is quite conceivable that they could overlap. Some of the various unique types of contrast are shown by numbers which correspond to the block numbers for the theoretical intensity profiles in fig. 7. It has been assumed here that $t \cong t_0/2$. At the centre of the two contours (area labelled as 3), $x = 0$. The lower contour goes through two contrast reversals while that above can be seen to go through a very faint third reversal at 28. In the region of overlap at 23, the domain boundary contrast is somewhat more complex. The corresponding variations of the background intensity with $x$ within the domains ($\alpha = 0$) for a single extinction contour is shown in fig. 9(b). Here again, the experimental results appear to be in good agreement with the predicted intensity variations. Extinction contours obtained from the 110 diffracted superlattice reflection (dark field) is also in agreement with the bright-field observations. The contrast as expected is reversed; however, these results are readily compared with the bright-field results by subtracting the numerical values of the transmitted intensity from one.

So far we have discussed the variation of the intensity profiles shown in fig. 7 with $x$, a parameter describing the variation of the film from the exact Bragg angle $\theta$. The deviation from the exact Bragg angle $\Delta\theta$ can be related to $x$ very nearly by the following expression

$$\Delta\theta \cong \frac{V_g x}{E \sin 2\theta} \qquad \cdots \cdots \cdots \quad (17)$$

where $E$ is the energy of the incident electrons and $V_g$ is given by eqn. (9). We now wish to find the value of $\Delta\theta$ at which the contrast of the antiphase domain boundaries will become negligible. Figure 7 indicates that this is approximately the case at about $|x| \geq 6$ and $t \leq t_0/8$. Table 5 shows typical values of $\Delta\theta$ for several superlattice reflections obtained by letting $x = 6$ in eqn. (17).

Table 5. Deviation from exact Bragg angle at which domain boundary contrast disappears for ordered AuCu₃ using 100 kv electrons

| $hkl$ | $\Delta\theta \ (S=1)$ | $\Delta\theta \ (S=0\cdot8)$ |
|:---:|:---:|:---:|
| 100 | 1° 35′ | 1° 16′ |
| 110 | 45′ | 40′ |
| 210 | 25′ | 20′ |

Thus, it is seen that the angle at which the domain boundary contrast can be observed is very critical and becomes more so with higher indices of reflection and/or as $S$ decreases. On the other hand, in the case of stacking faults $\Delta\theta$ is about 3° 30′.

The small value of $\Delta\theta$ for the superlattice reflections makes it somewhat difficult to examine microscopically the antiphase domain boundary contrast. This stems from the fact that thermal gradients produced by the electron beam are enough to give rise to sufficiently small changes of $\theta$ from the exact Bragg reflection to cause the contrast not only to vanish, but to continually pass through a series of reversals. This was particularly severe near the thinner portions of the film near the edges.

Because of the importance of $t_0$, for the superlattice reflection, in determining the nature of the antiphase domain boundary contrast, it is important to compare the numbers obtained theoretically with those found experimentally. Portions of fig. 3 for the fully ordered alloy and fig. 10 for the partially ordered alloy all show domain boundary contrast consisting of a double black fringe. In all cases, the normals to the foils are $[\bar{1}2\bar{1}]$ and the superlattice reflection giving rise to the boundary contrast is $10\bar{1}$. Since it is known that the domain boundaries in all these cases lie very nearly on 100 and 001 planes, then by eqn. (16) we can calculate $t_0$. In the case where $S=1$, the average value found for $t_0$ is about 900 Å, while for $S=0.8$ the average value for $t_0$ was measured to be about 1100 Å. These values are, as expected, much larger than those obtained by Whelan and Hirsch for stacking faults. They are however somewhat lower than the theoretical values shown in table 4. This latter discrepancy may arise from the fact that $\Delta\theta$ is not exactly zero, and/or secondly, in some cases the antiphase domain boundaries may not lie exactly on the cube planes. Nevertheless, the increased spacing of the fringes with decreasing order can be seen by comparing figs. 3 and 10.

## § 4. Summary and Conclusions

The present investigation has shown that transmission electron microscopy provides a very powerful means for examining directly the antiphase domain configurations present in ordered $AuCu_3$. Examination of both fully and partially ordered alloys shows that the antiphase domains often consist of a network of rectangular blocks, each face of which is surrounded by a domain of different type. In the partially ordered alloys, there is no indication of any two phase regions, and it is concluded therefrom that the degree of order within the domains is homogeneous but imperfect. Furthermore, the antiphase boundaries in both cases are found to lie essentially on cube planes. The present study also shows that the more indirect x-ray measurement of domain size gives good agreement with the direct measurements obtained from the thin foils.

It has also been found both theoretically and experimentally that in order for the antiphase boundaries to be revealed by electron transmission microscopy, the specimen must be oriented for a strong superlattice reflection. The antiphase boundary can be described in terms of a shear of adjacent portions of the crystal by $\frac{1}{2}a\langle 110\rangle$. This shear gives rise to a phase angle difference of 0 or $\pm\pi$ across the boundary for the superlattice

reflections. The detailed features of the domain boundary contrast can then be explained by introducing the appropriate phase angle and extinction distance into the dynamical theory of Whelan and Hirsch for the case of stacking faults. The experimental results are in good agreement with these theoretical predictions. The extinction distances for superlattice reflections are about four times that for principal reflections so that multiple fringes are not observed. The long extinction distance also gives rise to very critical angular settings for which domain boundaries will show contrast ($\simeq \pm 1°$ as compared to $\pm 4°$ for stacking faults).

Furthermore, one of the consequences of the present theory is that only two-thirds of all the antiphase boundaries will show contrast for any one particular strong superlattice reflection. This restriction usually causes the domains to form an apparent intricate maze pattern of superdomains, within which are contained the true smaller rectangular domains.

### References

Bain, E. C., 1923, *Chem. Met. Eng.*, **28**, 65.
Bollman, W., 1956, *Phys. Rev.*, **103**, 1588.
Fisher, R. M., and Szirmae, A., 1959, *Symposium on Electron Metallography* (American Society for Testing Materials), STP No. 262.
Glossop, A. B., and Pashley, D. W., 1959, *Proc. roy. Soc.* A, **250**, 132.
Griffoul, R., and Guinier, A., 1948, *Rev. Métall.*, **45**, 387.
Heidenreich, R. D., 1949, *J. appl. Phys.*, **20**, 993.
Ibers, J. A., 1958, *Acta cryst.*, **11**, 178.
Johansson, C. H., and Linde, J. O., 1925, *Ann. Phys., Lpz.*, **78**, 439; 1936, *Ibid.*, **21**, 1.
Kamiya, Y., Nonoyama, M., and Uyeda, R., 1959, *J. phys. Soc., Japan*, **14**, 1334.
Keating, D. T., and Warren, B. E., 1951, *J. appl. Phys.*, **22**, 286.
Ogawa, S., Watanabe, D., Watanabe, H., and Komoda, T., 1958, *Acta cryst.*, **11**, 872; 1959, *J. phys. Soc., Japan*, **14**, 936.
Pashley, D. W., and Presland, A. E. B., 1958–9, *J. Inst. Met.*, **87**, 419.
Raether, H., 1952, *Z. angew. Phys.*, **4**, 53.
Scherrer, P., 1920, *Zegmondy Kolloidchemie*, 3rd Edition, p. 387.
Sykes, C., and Jones, F. W., 1936, *Proc. roy. Soc.* A, **157**, 213.
Taylor, A., 1941, *Phil. Mag.*, **31**, 339.
Whelan, M. J., 1958–9, *J. Inst. Met.*, **87**, 392.
Whelan, M. J., and Hirsch, P. B., 1957, *Phil. Mag.*, **2**, 1121.
Wilchinsky, Z. W., 1944, *J. appl. Phys.*, **15**, 806.
Wilson, A. J. C., 1943, *Proc. roy. Soc.* A, **181**, 360; 1949, *X-ray Optics* (London: Methuen & Co. Ltd.).

# Some Remarks on the Boltzmann and Anti-Boltzmann Equations

By D. K. C. MacDonald

Division of Pure Physics, National Research Council, Ottawa, Canada

## Abstract

The derivation of the familiar Boltzmann equation from the mechanical equations of motion of an isolated system is a problem of long standing. Of particular interest is the question of how the transition from overall reversibility to irreversibility is dealt with, and recent papers by Adams (1960) and by Cohen and Berlin (1960) have drawn attention to the so-called anti-Boltzmann equation which appears somewhat paradoxical. Adams argues that the Boltzmann equation may only be used for prediction, and the anti-Boltzmann equation for retrodiction.

The present paper suggests that a generalized Boltzmann–Langevin equation helps to resolve any paradox, and it is shown that either the Boltzmann–Langevin *or* anti-Boltzmann–Langevin equation may be used for prediction or retrodiction. It remains true that the Boltzmann (–Langevin) equation is the natural choice for prediction when apparently irreversible behaviour is present.

## § 1. Introduction

The derivation of the familiar Boltzmann equation:

$$\frac{df}{dt} = -\frac{f-f_0}{\tau} \qquad \ldots \ldots \ldots \quad (1\,a)$$

for the distribution function, $f$, of a system from the mechanical equations of motion is a time-honoured problem. Recent papers by Adams (1960) and by Cohen and Berlin (1960) show that the question is still of great interest today. Both these papers discuss in particular the significance of the so-called 'anti-Boltzmann' equation (or 'anti-causal' Boltzmann equation), namely:

$$\frac{df}{dt} = \frac{f-f_0}{\tau}. \qquad \ldots \ldots \ldots \quad (1\,b)$$

Because of the fundamental reversibility of the mechanical equations of motion it would appear, to quote Adams (*loc. cit.*), that "the macroscopic motions which satisfy eqn. [1 $b$] are in some sense as common as those which satisfy [1 $a$]". On the other hand, if we consider the example discussed by Adams of the spontaneous electric current in a closed loop of wire with no applied e.m.f., then eqn. (1 $b$), when applicable, indicates that "the current builds up like $\exp(t/\tau)$", to quote Adams again, and at first sight this seems somewhat outrageous if regarded as a *prediction* on the same level as the prediction of eqn. (1 $a$) that in general the current

decays like $\exp(-t/\tau)$. I wish first to outline very briefly how these authors resolve for themselves the apparent paradox of the emergence of the anti-Boltzmann equation, but I neither wish nor feel competent to criticize the *detailed* derivations presented by these authors leading to eqns. (1 *a*) and (1 *b*). Thereafter I wish to suggest a rather obvious generalization of the Boltzmann equation (and of the 'anti-Boltzmann' equation) which appears to be of some value in resolving these apparent paradoxes.

Cohen and Berlin arrive at their results by consideration of correlation conditions in an assembly of particles either as $t \to -\infty$ or $t \to +\infty$. Very roughly speaking they find that the Boltzmann equation emerges if they apply a boundary condition to the problem such that the colliding molecules are essentially 'uncorrelated' in their behaviour for $t \to -\infty$†. On the other hand, they consider the situation where it might, on the face of it, be equally reasonable to assume that the molecular behaviour was 'uncorrelated' as $t \to +\infty$‡, but in this case they find from their analysis that the '*anti*-causal' Boltzmann equation makes its appearance.

Perhaps it might help to illustrate this situation in rudimentary fashion if we consider the elementary problem of an elastic collision between a molecule of a mass, $m$, and a so-called 'Rayleigh piston' of mass, $M$, free to move in only one dimension. If the velocities of the piston and colliding gas molecule in this dimension *before* the collision are $V_1$ and $v_1$ respectively, then after the collision we must of course satisfy the relations:

$$V_2 = V_1 \left( \frac{1-\mu}{1+\mu} \right) + v_1 \left( \frac{2\mu}{1+\mu} \right) \quad . \quad . \quad . \quad . \quad (2\,a)$$

and

$$v_2 = v_1 \left( \frac{\mu-1}{\mu+1} \right) + V_1 \left( \frac{2}{\mu+1} \right) \quad . \quad . \quad . \quad . \quad (2\,b)$$

where $\mu = m/M$. That is, if we consider a collision to occur between a piston and a molecule having arbitrary initial values of velocity $(V_1 ; v_1)$, then the velocities subsequent to the collisions $(V_2 ; v_2)$ are completely determined by, and involve, both the pre-collision velocities. Thus *in general*, with an assembly of gas molecules, if no correlation existed between the piston velocity and those of the gas molecules *before* the collision, we would be inclined to expect that some correlation would have been introduced by the collisions. So if we attempt to apply the proposed boundary condition that *after* the collision $(t \to +\infty)$ no correlation is to exist, this would suggest *in general* that some pre-arranged correlation

---

† To quote from Cohen and Berlin: "This boundary condition expresses somehow the fact that, 'long' before the molecules interacted, they must have been far apart and that therefore the pair distribution function can be written at that time as a product of two single particle distribution functions."

‡ To quote again from Cohen and Berlin: "One would be tempted to say that the formulation of a similar boundary condition in the *future* should be just as good because long after the molecules interacted they should also be far apart."

would have to exist *before* the collision†. Perhaps the 'temptation' to apply the uncorrelated boundary condition as $t \to +\infty$ arises because we are always inclined to suppose that collisions must automatically tend to destroy all correlation, while at least from the point of view of two colliding elements a collision (which after all is nothing other than interaction) may *introduce* some correlation.

On this basis we would therefore tend to reject lack of correlation *after* the collision as a suitable boundary condition for a general physical situation, and indeed this appears to be broadly the course adopted by Cohen and Berlin after their elegant and much more detailed discussion of the problem. That is to say, the 'anti-Boltzmann' equation is rejected as a solution of the statistical mechanical problem by Cohen and Berlin on the grounds that the necessary boundary conditions are unacceptable.

Adams however appears to resolve the problem in a somewhat different way, at least on the face of it. He argues that whenever we meet a significantly large fluctuation from equilibrium we must use the Boltzmann equation to *predict* the future course (i.e. the expected decay or regression) of the fluctuation, while the anti-Boltzmann equation is appropriate to describe *retrodictively* the past growth of the fluctuation to its present situation. Adams concludes particularly that: "one can never use [the anti-Boltzmann] equation for predicting the future experimental time variation of a non-equilibrium distribution function...... Even though we may *observe* that a fluctuation is carrying the system ever further from an equilibrium state, we must *expect* at each moment that the trend will immediately turn back toward equilibrium. The proper application of the anti-Boltzmann equation is for retrodiction during the progression of a fluctuation, just as that of the Boltzmann equation is for prediction during the regression of a fluctuation". In this sense Adams argues that the anti-Boltzmann equation makes its appearance equally often with the Boltzmann equation, and this appears equivalent to saying that, if a significant fluctuation is taking place, we are most likely to be around the maximum of the fluctuation (cf. e.g. Landau and Lifshitz 1938, p. 22), and that the time-dependence of the fluctuation must then look symmetrical on the average in either direction. One may perhaps feel a little uncomfortable about the fundamental significance of an equation (i.e. the 'anti-Boltzmann' equation in this case) which can never be used for prediction, but only for describing something that *has* happened, when one knows that it *has* happened. The resolutions of the reversibility–irreversibility paradox by Cohen and Berlin, and by Adams,

---

† We quote again from Cohen and Berlin: "Clearly, after a collision has taken place, a correlation between the particles is established which still exists when they are far apart. This is true whether the system is in equilibrium or not. That in equilibrium the large separation of the particles is a sufficient condition ..... is due to the fact that one can then neglect momentum correlations between the particles, the momenta always being distributed according to the Maxwell–Boltzmann distribution law."

are certainly most interesting but, on the face of it at least, seem to involve some difference of outlook in terms of prediction of the future course of events in a fluctuating system.

## § 2. A 'Generalized' Boltzmann Equation

We would like now to suggest a possible alternative approach to the problem. It seems to us that part, at least, of the difficulties arise because of the omission from the Boltzmann (and anti-Boltzmann) equation of a fluctuating term, the inclusion of which would then render the usual Boltzmann equation very similar to the so-called Langevin (1908) equation for Brownian movement. To be specific, we consider again the particular situation discussed by Adams, namely a closed loop of wire with no applied e.m.f. We consider therefore a distribution function:

$$f(v_x, v_y, v_z)$$

for the conduction electrons. For convenience we write:

$$\phi \equiv f - f_0,$$

where $f_0$ is the equilibrium value of the distribution function (i.e. yielding no current). Then we suggest that more appropriately the Boltzmann equation, at least as a first approximation, should be written:

$$\frac{d\phi}{dt} = -\frac{\phi}{\tau} + \frac{\partial f_0}{\partial v_x} A_1(t) + \frac{\partial f_0}{\partial v_y} A_2(t) + \frac{\partial f_0}{\partial v_x} A_3(t). \qquad . \quad . \quad (3)$$

We take our cue in proposing the form of the additional terms on the right-hand side of eqn. (3) from the form of the 'drift' or 'field' terms in the usual transport equation. Thus each $A_i(t)$ represents in effect a (rapidly varying) force term. More specifically we assume that:

$A_1(t)$, $A_2(t)$ and $A_3(t)$ are very rapidly varying functions of time, $t$, such that for $t > 0$:

(i)† : $$\overline{A_i(t) = 0} \qquad . \quad . \quad . \quad . \quad . \quad . \quad (4)$$

where the averaging indicated by the bar is over a sub-ensemble of systems such that:

$$\phi = \phi(0) \quad \text{at} \quad t = 0.$$

(ii) $\overline{A_i(t) A_i(t+s)} = 0$, unless $s$ is very small (and certainly *very* much smaller than $\tau$ of eqn. (1) and eqn. (3)); i.e.

$$\overline{A_i(t) A_i(t+s)} = \psi(s) \qquad . \quad . \quad . \quad . \quad . \quad (5)$$

where $\psi(s)$ is a function with a very sharp maximum around $s = 0$.

(iii) $\overline{A_i(t_1) A_j(t_2)} = 0$, (where $i \neq j$) for all $t_1$ and $t_2$.

---

† In stating their similar assumptions for the Langevin equation of Brownian movement, Uhlenbeck and Ornstein (1930), p. 824, open by saying: "Concerning [the fluctuating term] we will *naturally* make the following assumptions": and close by saying: "the justification, or eventually the criticism, of these assumptions must come from a more precise, kinetic, theory. *We will not go into that.*" The italics are ours.

Obviously the added terms in the Boltzmann equation represent in some degree the 'short-term' behaviour of the collision mechanisms, and it is presumably these terms which are assumed to vanish when some form of 'time-smoothing' is carried out in approaching the Boltzmann equation from mechanics. We suggest strongly however that when one is confronted with questions of time-reversal or, what appears to be perhaps equivalent, with questions of time-correlation in Boltzmann equation problems†, one should *not* omit these terms. This situation is familiar in the employment of the Langevin equation for the analysis of Brownian movement where products of the rapidly varying terms do indeed contribute to the correlation function for current, etc.

Solving eqn. (3) formally and without any suggestion of rigour, we have :

$$\phi(t) = \phi(0) \exp(-t/\tau) + \exp(-t/\tau) \frac{\partial f_0}{\partial v_x} \int_0^t \exp(u/\tau) A_1(u) \, du + \ldots$$

$$+ \text{corresponding terms in } A_2 \text{ and } A_3. \qquad \ldots \quad (6)$$

It follows immediately using eqn. (4) that if $t > 0$ :

$$\overline{\phi(t)} = \phi(0) \exp(-t/\tau). \qquad \ldots \quad (7\,a)$$

Furthermore, if we now consider a system which is in a statistically stationary condition, then :

$$\langle \phi(0) \rangle = 0,$$

where the average indicated by $\langle \ \rangle$ is over an equilibrium ensemble. Hence of course from eqn. (7 a) :

$$\langle \phi(t) \rangle = 0. \qquad \ldots \quad (7\,b)$$

So far our conclusions agree with what we might deduce from the 'naked' Boltzmann equation.

However, let us consider the *autocorrelation* function of $\phi$. Thus :

$$\overline{\phi(t)\phi(t+s)} = \phi^2(0) \exp[-(2t+s)/\tau] + \exp[-(2t+s)/\tau]$$
$$\times \left(\frac{\partial f_0}{\partial v_x}\right)^2 \int_0^t \int_0^{t+s} \overline{A_1(u) A_1(w)} \exp[(u+w)/\tau] \, du \, dw \ldots, \qquad (8)$$

with corresponding terms in $A_2$ and $A_3$. For convenience let us restrict our attention specifically to the model discussed by Adams, and consider only the electric current density is the $x$ direction, namely :

$$J_x(t) = e \int\int\int_{-\infty}^{+\infty} v_x \phi(t) \, dv_x \, dv_y \, dv_z. \qquad \ldots \quad (9)$$

It then follows that :

$$\overline{J_x(t) J_x(t+s)} = J_x^2(0) \exp[-(2t+s)/\tau]$$
$$+ \langle J_x^2 \rangle \exp(-s/\tau)[1 - \exp(-2t/\tau)] \qquad . \quad (10\,a)$$

or $$\quad \overline{J_x^2(t)} = J_x^2(0) \exp(-2t/\tau) + \langle J_x^2 \rangle [1 - \exp(-2t/\tau)]. \qquad . \quad (10\,b)$$

† It will be remembered that Onsager (1931), after his initial semi-qualitative discussion of the significance of time-reversibility in irreversible processes, specifically introduces his requirement of microscopic reversibility in terms of a stationary requirement on a correlation function.

If we wish to identify the overall closed system as being not only in statistically stationary equilibrium, but also in *thermodynamic* equilibrium at a temperature $T$, then we could now write:

$$\langle J_x^2 \rangle = kT/LA^2 \qquad . \quad . \quad . \quad . \quad . \quad (11)$$

where $A$ is the cross-sectional area of the 'passive' metal ring envisaged by Adams, and $L$ is the self-inductance of the ring. However, this does not appear strictly necessary for our present purposes so long as we assume that *some* statistically stationary state (characterized by $\langle J_x^2 \rangle$) is in general reached ultimately by the ring if left for long enough to its own devices.

Let us now consider how we would interpret the predictions of our 'generalized' Boltzmann equation. Consider first a metal ring which initially $(t=0)$ has a current density $J_x(0)$ which is '*small*', i.e. roughly speaking within the region of the *typical* fluctuations( i.e.

$$|J_x(0)| \sim (1/A)\sqrt{(kT/L)},$$

cf. eqn. (11)). If then we consider a (sufficiently large) sub-ensemble of such systems we can make a number of (very reliable) predictions about the future behaviour of such a sub-ensemble. If we restrict ourselves to considering the *average* current density, $\overline{J_x}(t)$, of this sub-ensemble, then we have:

$$\frac{d\overline{J_x}}{dt} = -\frac{\overline{J_x}}{\tau}, \qquad . \quad . \quad . \quad . \quad . \quad . \quad (12)$$

which of course is directly analogous to saying that the bare Boltzmann equation predicts:

$$\frac{d\phi}{dt} = -\frac{\phi}{\tau}. \qquad . \quad . \quad . \quad . \quad . \quad (13)$$

However, the generalized Boltzmann–Langevin equation tells us something further of significance about the behaviour of the mean square current, $\overline{J_x^2}(t)$. If we consider a (sufficiently large) sub-ensemble of systems with $J_x(0) = 0$ (and hence $J_x^2(0)=0$), then eqn. (12) predicts that $\overline{J_x}$ remains zero, but eqn. (10 b) which may be rewritten alternatively:

$$\frac{d\overline{J_x^2}}{dt} + \frac{2}{\tau}\overline{J_x^2} = \frac{2}{\tau}\langle J_x^2 \rangle, \qquad . \quad . \quad . \quad (14)$$

predicts an essentially stable 'build-up' again of the mean square current over the sub-ensemble to the normal value for statistical equilibrium.

Now let us consider instead a sub-ensemble of systems having $J_x(0)$ relatively '*large*' (i.e. in effect $|J_x(0)| \gg \langle J_x^2 \rangle^{1/2}$), then eqn. (3) implies in effect that until $J_x(t)$ begins to approach the typical equilibrium level as determined by the typical 'fluctuations', the expected behaviour of the

sub-ensemble will almost certainly be adequately governed by the simple, or 'naked', Boltzmann equation. In other words, we may say that the equations:

$$\overline{J_x(t)} = J_x(0) \exp(-t/\tau)$$

and

$$\overline{J_x{}^2(t)} \approx J_x{}^2(0) \exp(-2t/\tau)$$

(so long as $|J_x(t)| \gg \langle J_x{}^2 \rangle^{1/2}$, cf. eqn. (10 $b$)) predict almost certainly a decay law for the members of the sub-ensemble which would be given simply by the normal Boltzmann equation as applied to individual members of the system.

### § 3. RETRODICTION FROM THE BOLTZMANN–LANGEVIN EQUATION

So far we have restricted ourselves to discussing the *predictive* behaviour of what we call the Boltzmann–Langevin equation: i.e. the behaviour for $t > 0$. We discuss and compare in an appendix the general statistical analysis of both Boltzmann–Langevin and 'anti-Boltzmann–Langevin' equations, but here we would simply point out that if we assume, as we have done, that the fluctuational term ($A_i(t)$ in eqn. (3)) is *uncorrelated* with $\phi(0)$ for $t > 0$ (eqn. (4)), it follows that we *must* assume a correlation for $t < 0$ (i.e. if the fluctuational term *antedates* $\phi(t)$). Writing the Langevin equation for $J_x(t)$ as:

$$\dot{J}_x(t) + J_x(t)/\tau = I_1(t) \qquad \cdots \cdots \cdots (15)$$

where $I_1(t)$ is the rapidly fluctuating term, we need only note here that if:

$$\overline{I_1(t)} \approx 0 \quad \text{for} \quad t > 0, \qquad \cdots \cdots \cdots (16a)$$

cf. eqn. (4), then essentially we are required to assume:

$$\overline{I_1(t)} = \frac{2J_x(0)}{\tau} \exp(t/\tau) \quad \text{for} \quad t < 0, \qquad \cdots \cdots (16b)$$

cf. eqn. (A 8 $a$) in the Appendix. The formal solution of eqn. (15) is:

$$J_x(t) = J_x(0) \exp(-t/\tau) + \exp(-t/\tau) \int_0^t \exp(u/\tau) I_1(u) \, du, \qquad (17)$$

and using eqns. (16 $a$) and (16 $b$) we then have:

$$\overline{J_x(t)} = J_x(0) \exp(-t/\tau) \quad \text{for} \quad t > 0 \qquad \cdots \cdots (18a)$$

and

$$\overline{J_x(t)} = J_x(0) \exp(t/\tau) \quad \text{for} \quad t < 0. \qquad \cdots \cdots (18b)$$

Consequently if the important fluctuational term is not omitted it follows that the Boltzmann–Langevin equation can be used for both prediction *and* retrodiction of the behaviour of a sub-ensemble, and we also show in the Appendix that the same is true for the 'anti-Boltzmann–Langevin' equation when the fluctuational term is properly taken into account.

On the other hand, of course, the generalized Boltzmann equation does not permit one to make any reliable *predictions* about when, or how

a system will (very rarely) build up *towards* a large value, say $J_x(t)$, from an initial value $J_x(0)$ lying within the normal level of fluctuations. Equation (6) simply says in effect that this *may* happen (rarely) if the appropriate 'fluctuation' integral on the right-hand side of eqn. (6) fortuitously attains a large value.

## § 4. Conclusion

It remains to be seen of course whether the suggested generalization of the Boltzmann equation is of any further real value, but it would be of interest to know whether eqn. (3) would arise *naturally* as a closer approximation to the solution in the derivation of the Boltzmann equation from a starting point such as Liouville's theorem. It appears to us in any case that when problems of time reversibility, or questions of correlation in time, arise in connection with the Boltzmann equation the rapidly varying terms should *not* be omitted.

## Acknowledgments

## APPENDIX

### The Boltzmann–Langevin Equation

Let $y(t)$ be some macroscopic observable of the statistically stationary ensemble. Then quite generally we have:

$$\frac{dy}{dt} = f(t), \quad \text{say}, \qquad \cdots \qquad (A\,1)$$

where this equation in overall statistical equilibrium must be reversible in form, i.e. I would say that the statistical properties of this equation must not be altered by replacing $t$ by $-t$. We are to believe that under certain circumstances eqn. (A 1) can lead to either a Boltzmann or 'anti-Boltzmann' equation. More generally therefore I suggest that we consider a Boltzmann–Langevin equation:

$$\frac{dy}{dt} = -\frac{y}{\tau} + I_1(t) \qquad \cdots \qquad (A\,2)$$

or an anti-Boltzmann–Langevin equation:

$$\frac{dy}{dt} = +\frac{y}{\tau} + I_2(t). \qquad \cdots \qquad (A\,3)$$

Now multiply (A 2) and (A 3) by $y$ and average over an ensemble in statistical equilibrium, so that the left-hand side:

$$(=\tfrac{1}{2}\langle dy^2/dt\rangle)$$

must vanish. We see that the Boltzmann–Langevin equation demands in general:

$$\langle I_1(t)y(t)\rangle = \langle y^2\rangle/\tau, \qquad \cdots \cdots \quad (A\,4)$$

while the anti-Boltzmann–Langevin equation demands:

$$\langle I_2(t)y(t)\rangle = -\langle y^2\rangle/\tau. \qquad \cdots \cdots \quad (A\,5)$$

Thus the Boltzmann–Langevin equation demands a direct correlation between the macroscopic observable, $y$, and the essentially 'microscopic' (extremely rapidly varying) $I_1(t)$. In contrast the anti-Boltzmann–Langevin equation requires an *anti*-correlation of these quantities, which might be regarded as a very improbable situation in general. We might therefore regard eqn. (A 5) as suggestive grounds for 'rejecting' the anti-Boltzmann–Langevin equation, perhaps analogous to Cohen and Berlin's rejection of the anti-Boltzmann equation.

We would also suggest that the transition from eqn. (A 1) to (A 2) or (A 3) indicates rather clearly why time-smoothing, which surely involves the 'washing out' of $I_1(t)$ or $I_2(t)$, means that an essential feature of the overall reversibility has been lost. If instead we *retain* the form of eqn. (A 2), for example, then there are limited situations (i.e. when $I_1(t)$ may be temporarily neglected in comparison with $y/\tau$) when the behaviour will *seem* irreversible, but of course on other occasions then $I_1(t)$ is the dominant term, so restoring overall reversibility.

If, following eqn. (4) in the text, we write:

$$\overline{I_1(t)} \approx 0 \quad \text{for} \quad t>0 \qquad \cdots \cdots \quad (A\,6)$$

(we recall that the bar means an average over a sub-ensemble with $y=y(0)$ at $t=0$), then this suffices to yield directly from eqn. (A 2) the auto-correlation function:

$$\langle y(t)y(t+s)\rangle \equiv \psi(s) = \langle y^2\rangle \exp(-|s|/\tau), \qquad \cdots \quad (A\,7)$$

which we may note is finite and integrable. (These simple requirements are necessary if we are to have finite fluctuations and a steady statistical state at all.) It then however follows *without further ado* that:

$$\langle y(t)I_1(t+s)\rangle = (2\langle y^2\rangle/\tau)\exp(s/\tau) \quad \text{for} \quad s<0. \qquad \cdots \quad (A\,8)$$

I am not aware if this *asymmetry* of cross-correlation between $y(t)$ and $I_1(t)$, exemplified by eqns. (A 6) and (A 8), has been discussed by other authors but it appears an important and *necessary* consequence of the transition from eqn. (A 1) to eqn. (A 2) (or (A 3)); it is in this way that the *overall* time-reversibility of eqns. (A 2) and (A 3) is retained while irreversibility appears when (and if!) $I_1(t)$ or $I_2(t)$ can be neglected.

More particularly if we restrict ourselves to a sub-ensemble (with $y = y(0)$ at $t = 0$) then it appears that eqns. (A 4) and (A 8) must read:

$$\overline{I_1(0)} = y(0)/\tau \qquad \cdots \cdots \quad \text{(A 4 a)}$$

and

$$\overline{I_1(t)} = (2y(0)/\tau) \exp(t/\tau) \quad \text{for} \quad t < 0, \qquad \cdots \quad \text{(A 8 a)}$$

and the latter is just the equation we have used in the text (eqn. (16 $b$), writing: $J_x = y$) to demonstrate that the Boltzmann–Langevin equation can be used equally validly for prediction *and* retrodiction of a sub-ensemble, *if* the statistics of the fluctuational term are taken into account.

## The Anti-Boltzmann–Langevin Equation

If the anti-Boltzmann–Langevin equation (eqn. (A 3)) is to describe the same statistical ensemble then the auto-correlation function (eqn. (A 7)) must be the same, and this now *requires* that we assume:

$$\overline{I_2(t)} \approx 0 \quad \text{for} \quad t < 0, \qquad \cdots \cdots \quad \text{(A 9)}$$

(where the bar has the same significance as for eqn. (A 6)), and it also follows that we must assume:

$$\langle y(t)I_2(t+s) \rangle = -(2\langle y^2 \rangle/\tau) \exp(-s/\tau) \quad \text{for} \quad s > 0; \qquad \text{(A 10)}$$

and again if we restrict ourselves to a sub-ensemble with $y = y(0)$ at $t = 0$, it appears we must replace eqn. (A 10) by

$$\overline{I_2(t)} = -(2y(0)/\tau) \exp(-t/\tau) \quad \text{for} \quad t > 0. \qquad \text{(A 10 a)}$$

The formal solution of the anti-Boltzmann–Langevin equation is

$$y(t) = y(0) \exp(t/\tau) + \exp(t/\tau) \int_0^t \exp(-u/\tau) I_2(u)\,du. \qquad \text{(A 11)}$$

For $t < 0$ we have immediately, using eqn. (A 9):

$$\overline{y(t)} = y(0) \exp(t/\tau),$$

agreeing directly with eqn. (18 $b$) for the Boltzmann–Langevin equation, both under conditions of *retrodiction*. And, using eqn. (A 10 $a$), we have for $t > 0$:

$$\overline{y(t)} = y(0) \exp(-t/\tau),$$

agreeing with eqn. (18 $a$) for the Boltzmann–Langevin equation, both under conditions of *prediction*.

Thus if we are prepared to make the appropriate correlation conditions (and in particular eqns. (A 4) and (A 5)), *either* the Boltzmann (–Langevin) *or* anti-Boltzmann (–Langevin) equation will suffice equally well for *either* prediction *or* retrodiction. On the other hand of course we may be inclined to adhere to the Boltzmann (–Langevin) equation as providing a much more probable description of the statistical situation.

Moreover, if we regard prediction generally as the normal business of physics then it would seem obvious that the Boltzmann (–Langevin) equation is the natural choice to make. Put in other words, if we are concerned solely with prediction then we can justifiably use the Boltzmann equation (i.e. *without* the fluctuational term) whenever (apparently) irreversible behaviour is expected.

## References

ADAMS, E. R., 1960, *Phys. Rev.*, **120**, 675.
COHEN, E. G. D., and BERLIN, T. H., 1960, *Physica*, **26**, 717.
LANDAU, L. D., and LIFSHITZ, E. M., 1938, *Statistical Physics* (Oxford: Clarendon Press).
LANGEVIN, P., 1908, *C. R. Acad. Sci., Paris*, **146**, 530.
ONSAGER, L., 1931, *Phys. Rev.*, **37**, 405.
UHLENBECK, G. E., and ORNSTEIN, L. S., 1930, *Phys. Rev.*, **36**, 823.

# CORRESPONDENCE

## Direct Observation of Dislocations due to Epitaxy

By P. Delavignette, J. Tournier and S. Amelinckx

Solid State Physics Department, Centre d'Etude de l'Energie Nucléaire,
MOL, Belgium

Several years ago Frank and Van der Merwe (1949 a, b, 1950) studied theoretically the conditions under which epitaxial growth gives rise to dislocations at the interface. However, to the best of our knowledge, no evidence for the occurrence of this type of dislocation seems to be available so far.

The epitaxial dislocations are generated in order to relieve the stress set up as a consequence of the misfit The fit between substrate and overgrowth is perfect only within small islands separated by dislocations. The density of dislocations will evidently be smaller the better the fit. For very small misfits one can therefore hope to observe the individual epitaxial dislocations directly in transmission electron microscopy.

In the course of a study of dislocation ribbons in layer structures (Amelinckx and Delavignette, to be published) such direct evidence was obtained. The figure† shows a transmission electron micrograph of a thin crystal of chromium bromide. On this platelet as a substrate small elongated crystals of an unknown nature were observed. The elongation has three possible directions differing by 60°, with respect to the substrate. These small crystals were deposited on the platelets of chromium bromide during their growth from the vapour. No identification was possible since the electron diffraction pattern apparently coincides with the one of the substrate. The elongated habit of the crystals suggested strongly that they are not chromium bromide, since this has hexagonal symmetry. It was found that these small crystals invariably contained dislocation arrays of the kind shown in the figure, and which extended only over the area of the crystal. They produce a contrast which is markedly different from the contrast at normal dislocations in the substrate foil.

This of course may be due to their proximity to the surface, but it is suggested that this is due to their different nature. It should be noted that the lines are *not* moiré fringes.

As far as thickness can be judged from absorption contrast, it was noticed that in the very thin crystals the density of dislocations was generally smaller than in the thicker ones, in which often crossed grids of dislocations were found (figure, A). In crystals of comparable thickness

---

† Shown as a plate.

the distance between dislocations was roughly the same. These observations are in agreement with the picture for the nucleation of oriented overgrowth given by Frank and Van der Merwe. The first layers of the overgrowth would deform elastically and essentially fit perfectly on the substrate. On thickening larger stresses would be set up and dislocations would be introduced.

## REFERENCES

AMELINCKX, S., and DELAVIGNETTE, P., 1961, *J. appl. Phys.* (in the press).
FRANK, F. C., and VAN DER MERWE, J. H., 1949 a, *Proc. roy. Soc.* A, **198,** 205, 216; 1949 b, *Ibid.*, **200,** 125; 1950, *Ibid.*, **201,** 261.

# REVIEWS OF BOOKS

*Modern University Physics.* By J. A. Richards, F. W. Sears, M. R. Wehr and M. W. Zemansky. (Addison-Wesley Publishing Company Inc., 1960.) [Pp. xvi + 993.] Price £2 13s. 0d.

This volume is a collation of two older textbooks, *University Physics* by Sears and Zemansky, and *Physics of the Atom* by Wehr and Richards. The two sources are perfectly distinguishable still, and it seems a curious idea ever to have combined them. The first two-thirds of the book provides an account of the traditional A-level physics syllabus in this country. The treatment is straightforward and clear, in the manner of the best American text-books, with plenty of illustrative examples and diagrams; it is far from sophisticated, however, and the title will seem a misnomer to most British readers. For example, the notion of a differential equation is never invoked though some elementary calculus is used in places. One gets as far as polarized light, but many topics of importance are left neglected by the way (viscous flow for example, or the specific heats of gases—two topics chosen quite at random) and none of the fundamental concepts introduced is discussed at all critically.

These criticisms are perhaps not too serious for a text-book that is clearly meant for readers starting physics essentially from scratch, but in the light of them it is strange to find the last third of the book dealing with the Lorentz transformations of relativity. The ground covered here stretches from the photoelectric effect to mesons and strange particles, and then pages of isotope tables are added at the end for good measure. The writing is again commendably clear, though the treatment is inevitably more superficial and descriptive than in the first part.

The whole book implies a gallant effort to teach students in one year the elements of physics. Perhaps it is just what is needed by the future technologists and administrators of our nuclear age, but the present reviewer retains an old-fashioned bias in favour of teaching less material more thoroughly.

T. E. F.

*Plasmas and Controlled Fusion.* By David J. Rose and Melville Clark, Jr. (Massachusetts Institute of Technology and Wiley, 1961.) [Pp. 493.] Price £4 6s. 0d.

In the last few years many books concerned with plasma physics and the problems of controlled fusion have been published. In most cases the reader gains a strong impression that the authors have been commissioned by some publishing house anxious to supply the insatiable demands of scientific libraries. It is therefore a great pleasure to welcome a book in this specialist field whose sole aim is to inform and teach the reader. Whilst written primarily as a graduate level text-book, the contents cover such a wide field that it will strongly appeal to all those engaged in the subject no matter how experienced they may be. The clarity of the exposition suggests that the authors have a deep appreciation of the principles of plasma physics which is all the more unexpected as both are engineers.

It is not surprising that many aspects of plasma physics should be omitted or treated briefly. However, it is to be regretted that the authors did not find space in the 500 pages of this book to define a plasma or to refer to astrophysical applications of the subject.

This book is strongly recommended to all those either engaged in plasma physics studies or who are approaching the subject for the first time.

P. C. T.

*Variational Principles in Dynamics and Quantum Theory.* Second edition. By W. YOURGRAU and S. MANDELSTAM. (Pitman, 1960.) [Pp. 179.] Price £1 12s. 6d.

NATURE seems fond of stationary principles. It is her métier to minimize. This book gives a thorough account of the variational principles of mathematical physics with much entertaining material on their historical and philosophical contents. The principal new feature of the second edition is a chapter giving a simple account of approaches to quantum mechanics formulated by Feynman and Schwinger.                                                                        J. C. P.

*The Principles of Nuclear Magnetism.* By A. ABRAGAM. (Oxford: University Press, 1961.) [Pp. 599.] Price £4 4s. 0d.

THIS book is an outstanding contribution to contemporary scientific writing. In it, the underlying theory of nuclear magnetism is set out clearly, attractively and in detail. It is a book which will appeal to all who work in this field, to physicists and to chemists alike. The book is, of course, largely a treatise on nuclear resonance, but the author has indicated by the title that the basic theory for the behaviour of a system of nuclear magnetic dipoles extends beyond any one particular experimental technique. He always bears in mind that the real interest in nuclear magnetism arises from the general physical and chemical information which can be derived about the nuclei themselves or the substances in which they are found.

The size of the book may lead the prospective reader to suspect that it should be regarded as a reference work rather than a text-book which can be read from cover to cover. In fact the book is ideal for both purposes. It is written in a style and the argument is developed in a sequence which makes it exciting and enjoyable reading throughout. It can indeed be read as a complete text and Dr. Abragam has taken great care to sketch in the less familiar aspects of the basic theory so that the reader will have sufficient confidence to follow his subsequent detailed mathematical arguments. This is not to imply that the reader will find the book easy or trivial. The theoretical treatment makes no concessions to superficial and uncritical thinking. It is however a stimulating and worth-while course to follow and Dr. Abragam is continually encouraging the student both by giving useful physical interpretations and by illuminating examples of the simplifications which arise for limiting cases of the theory.

The book is concerned principally with the properties of nuclei in non-conducting solids and liquids. It begins with a survey of the basic and most simple underlying theory and then, after a brief survey of the principles of some of the important experimental techniques, it treats in detail the line width of the nuclear resonance absorption arising from dipolar interactions, the concept of spin temperature, the electron–nucleus interaction, quadruple effects, relaxation phenomena, nuclear polarization and diffusion effects. There is a final chapter on the use of strong radio-frequency fields. For my own part, I found this last chapter rather less satisfying than the rest of the book and I was left with a slight feeling of anti-climax. This is however a personal reaction and may arise because I was somewhat disappointed in not finding a definite section of the book devoted to the properties of nuclei in metals (both paramagnetic and ferromagnetic) and the applications of the Mössbauer effect. These aspects of nuclear magnetism are indeed discussed in the book but they are treated rather briefly and arise as particular examples of electron–nuclear interactions and dynamic polarization in solids. There are a large number of very useful illustrative graphs and diagrams, but no tables of general nuclear data. Dr. Abragam has fully justified this general decision in the Preface but experimentalists particularly will wish that he could make one or two exceptions to

this rule. For example, the inclusion of a short table of general physical constants and a table of nuclear spins, moments and isotopic abundances for the elements, would make the book so much more convenient for those of us who often need to carry out a first order numerical calculation in order to see whether the theory is likely to account for our experimental results. Such information is of course available elsewhere, but it is particularly convenient if the reader has simply to turn to the end of the book which he is studying and there find listed the basic data from which he can make his preliminary calculations.

This book should be recommended to every serious student of magnetic resonance phenomena, whether his chosen field be concerned principally with nuclear or with electronic spins. It will certainly be regarded as an essential text-book for theoreticians. Experimentalists will also value it greatly for the assistance it provides in clarifying their ideas and for interpreting their experimental results. We are all greatly indebted to Dr. Abragam for writing this outstanding book. D. M. S.

*Elements of Modern Physics.* By PAUL L. COPELAND and WILLIAM E. BENNETT. (New York: Oxford University Press, 1961.) [Pp. 507.] Price £3 8s. 0d.

THE purpose of this text is indicated by its subtitle ' A Course in Those Aspects of Modern Physics That Underlie Important Engineering Developments '. The first part of the book treats the rise of atomic physics, including among other topics kinetic theory, the Bohr theory of atoms, Einstein's and Debye's theories of specific heat, crystal structure and reflection of x-rays, and relativistic motion of electrons. The second part deals with electrons in atoms, molecules and solids mostly based on the ideas of de Broglie waves but with some elementary use of the Schroedinger equation. It includes the free electron theory of metals, the idea of energy band structure in solids, and 46 pages on semi-conductor physics. The third part covers radioactivity, nuclear reactions, a chapter on nuclear structure and stability, and one on fission and atomic energy. The book presupposes that the student has covered courses in classical physics and calculus, and where possible within the scope of a course designed for one semester, a mathematical treatment is given, e.g. a Boltzmann gas impinging on a potential barrier. Mostly however the detailed results of calculations are just stated with a good discussion of their underlying physical principles and uses. V. H.

*Dispersion Relations and the Abstract Approach to Field Theory.* International Science Review Series, Vol. 1. Edited by LEWIS KLEIN. (New York: Gordon and Breach, Inc., 1961.) [Pp. 273.] Price $4.95.

IN recent years elementary particle physicists have been busy exploring the complex plane. Scattering amplitudes have been discovered to possess powerful analytic properties with the result that an S-matrix approach to the strong interaction problem has yielded non-trivial useful results. This book is a compendium of some of the important papers on this topic. It is particularly rich and complete on the more austerely abstract side of the subject, dealing with axiomatic field theory, the Wightman programme and the proof of dispersion relations. However, it also includes Mandelstam's celebrated conjecture on the properties of the elastic scattering amplitude and one short paper on the analytic properties of perturbation theory.

While this reviewer is unable to agree with the editor's opinion that such collections of original papers provide a means of learning a subject which is often superior to reading a coherent exposition it is nevertheless of some value to find so many of the major papers bound together. J. C. P.

*Classical Electricity and Magnetism.* By E. S. Shire. (Cambridge: University Press, 1960.) [Pp. 396.] Price £2 5s. 0d.

This work is intended to be a text-book for a second stage of the study of electricity and magnetism and as such it has great merits. It is almost entirely concerned with the macroscopic aspects of the subject, hence the epithet ' classical ' in the title. The author has chosen the historical approach, but the treatment is much more modern and original than the approach suggests. The historical perspective is, wherever possible, stressed, but on the other hand the relation with new developments finds its proper place. Typical for this are chapters on circuit theory, electrical measurements and applied electricity, including a discussion on particle accelerators. The difficult concept of energy and its relation to the Helmholtz free energy is introduced at an early stage and further developed in the later stages. The treatment is everywhere lucid and consistent.

The author takes the view that a physicist should be able to move with ease from one system of units to another. In order to facilitate this he has introduced a symbol $\delta$ in many formulae, which has to be chosen according to the system of the units the reader prefers to use. The advantage of this is perhaps smaller than appears at first because the choice of units will in practice usually not be made by the intended reader, but by whoever lectures to him on the subject. In view of the general level of the book it is somewhat surprising that symbols such as div and curl only appear in footnotes, while in the text itself the corresponding differential expressions are explicitly written out. This is however only a minor criticism compared with the many admirable qualities of the book. Many exercises are given at the end of each chapter, partly taken from Cambridge University examination questions.                      D. B.

*Gases at High Densities and Temperatures.* By Yu N. Ryabinin. (Pergamon Press, 1961.) [Pp. 52.] Price 25s.

This book describes experimental research on the properties of gases at high densities and temperatures carried out by the author and his colleagues in Russia. The research was centred on an apparatus in which gases under test can be compressed rapidly by a piston. The piston is accelerated by a second, driver, gas. Pressures up to 10 000 kg/cm² were obtained, and typical temperatures were 9000°K in argon and 3000°K in air and nitrogen. It is assumed in the work that the compression process is isentropic, although there is some evidence in one experiment that at least weak shock waves were present. Studies were made of light emission, electrical conductivity and thermodynamic state of the gases. The author believes that the results on electrical conductivity indicate a lowering of the effective ionization potential at high densities. There are not sufficient results for a very positive conclusion.

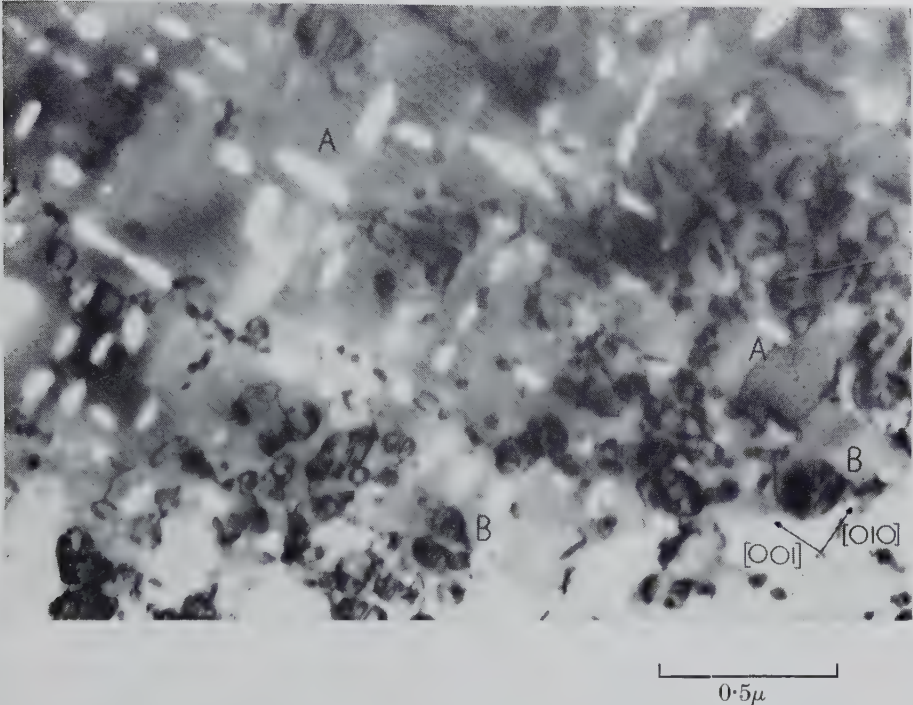The book is to be welcomed as making an addition to experimental knowledge in a field where experiment is rare.                      M. D. C.
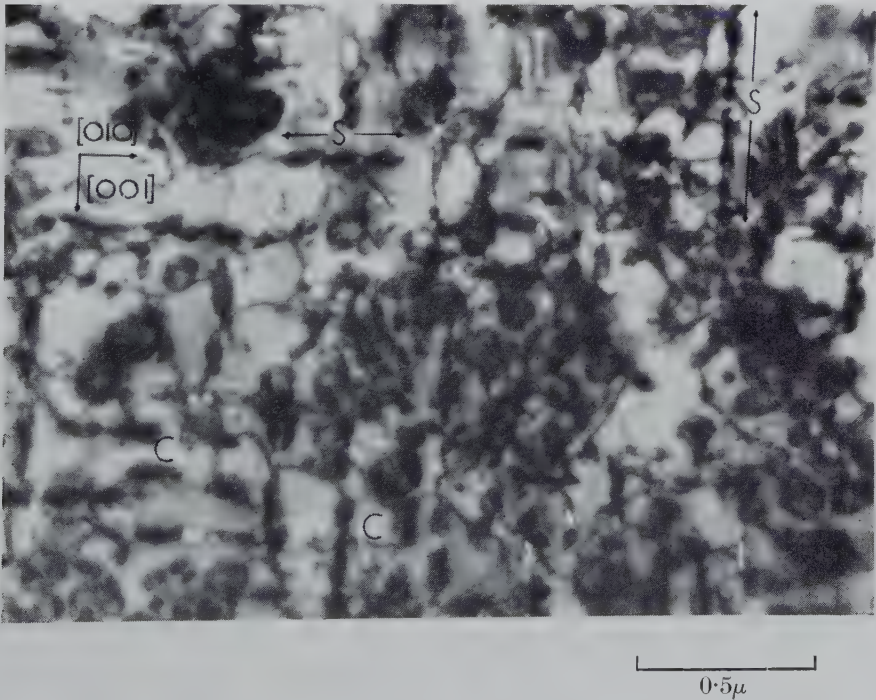
Fig. 1



An area in a gold 1·5% cobalt specimen showing elongated holes A and contrast effects B.   Plane of the foil is (100).   Magnification × 47 000.

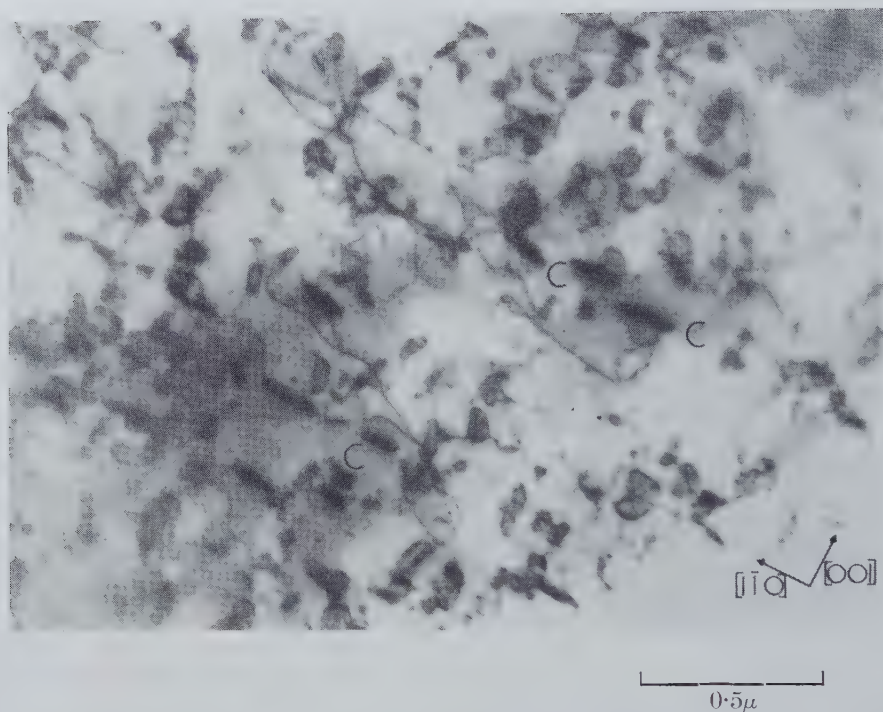Fig. 2



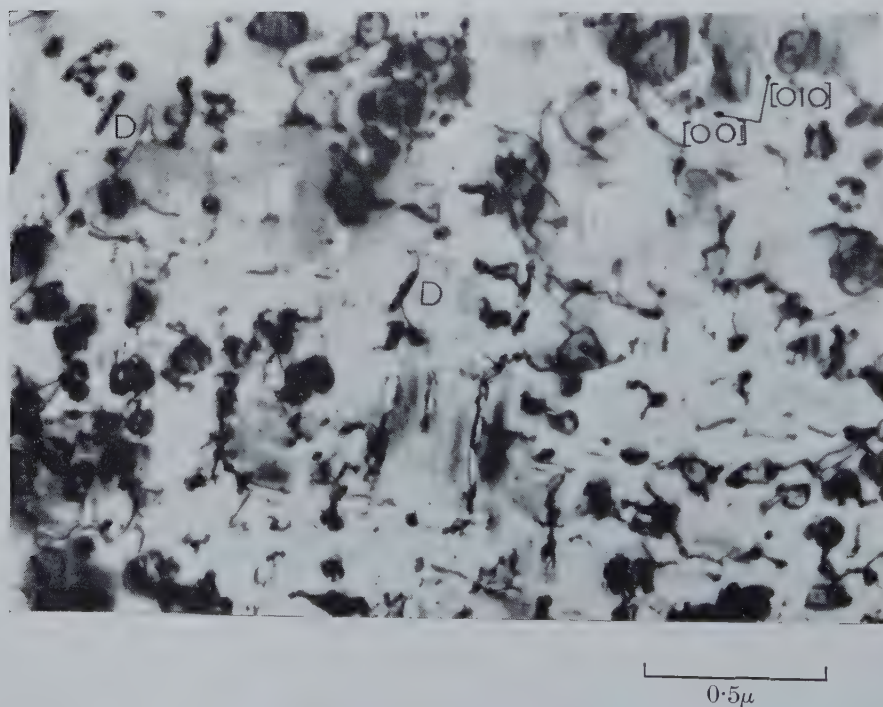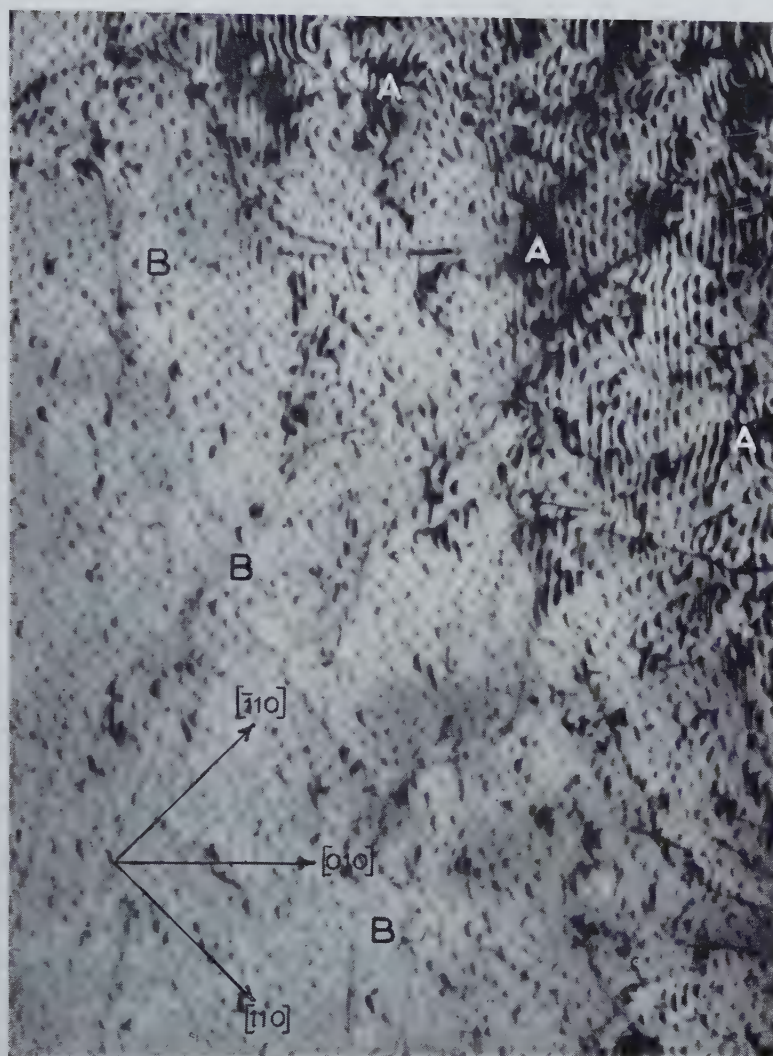Rows of particles, S, seen in a (100) area of a gold 1·5% cobalt specimen. Magnification × 47 000.

Fig. 3



An area of a gold 1·5% cobalt specimen in a (110) orientation.    Note the streaks
C  parallel to [1$\bar{1}$0].   Magnification  ×47 000.

Fig. 4



An area of a gold 1·5% cobalt specimen showing possible rod-like precipitates D.
Magnification  ×47 000.

J. W. MATTHEWS

Phil. Mag. Ser. 8, Vol. 6, Pl. 152.

Fig. 1



Electron micrograph of PbSe on PbS. The area labelled A contains moiré
fringes of type (1) in the table. Both sets of misfit dislocations are visible
in the area labelled B. Magnification × 140 000.

J. W. MATTHEWS

Phil. Mag. Ser. 8, Vol. 6, Pl. 153.
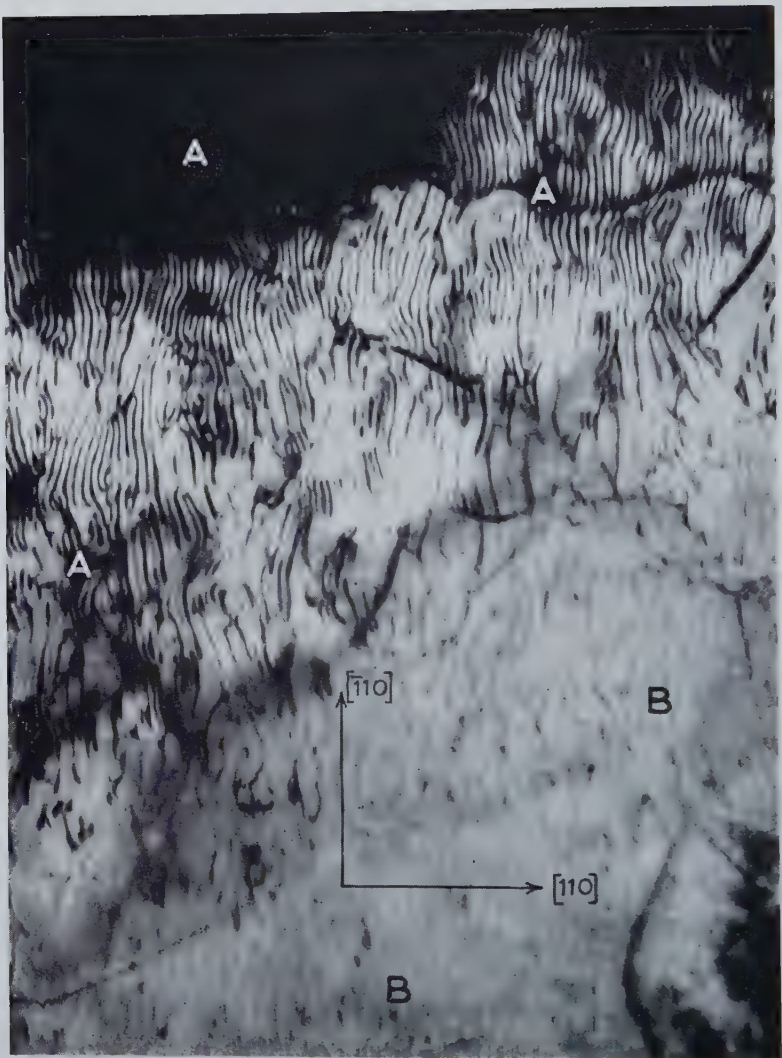
Fig. 2



Electron micrograph of PbSe on PbS. The area labelled A contains moiré
fringes of type (2) in the table. One set of misfit dislocations is visible
in the area labelled B. Magnification ×140 000.

R. M. J. COTTERILL

Phil. Mag. Ser. 8, Vol. 6, Pl. 154.

Fig. 2



Typical area used in the determination of $C_T$ and $L_{r.m.s.}$  The foil thickness is found from the apparent width of the slip traces and the direction of the foil normal (close to [110]).  (Mag. $\times 42\,000$.)

Fig. 4



(a)
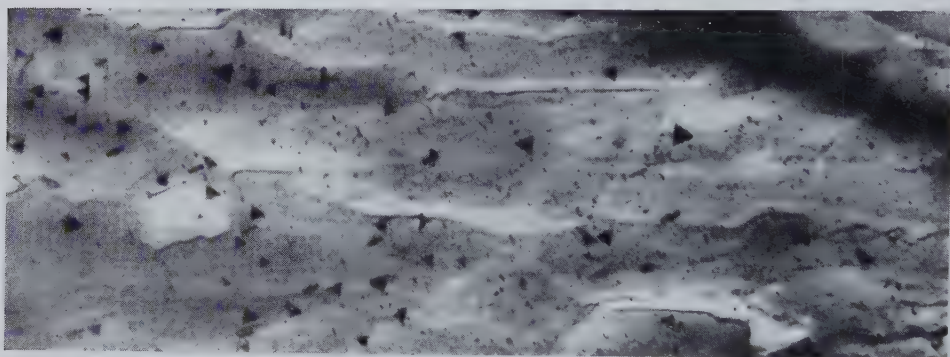


(b)



(c)

Specimens quenched from different temperatures, $T_q$, and fully annealed at
100°C. (a) $T_q = 750°$c. (b) $T_q = 800°$c. (c) $T_q = 1000°$c. (Mag. ×42 000.)

Fig. 6



(a)
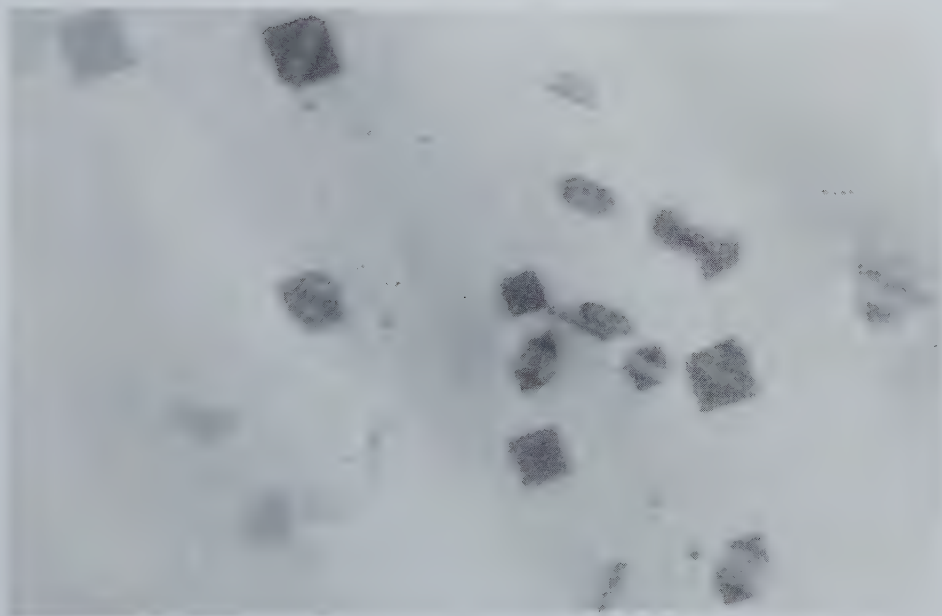


(b)

Specimen quenched from 930°c.   (a) Annealed less than 60 sec  at  15°c.
(b) Annealed for one hour at 100°c.   (Mag.  × 170 000.)

Fig. 2



x 28
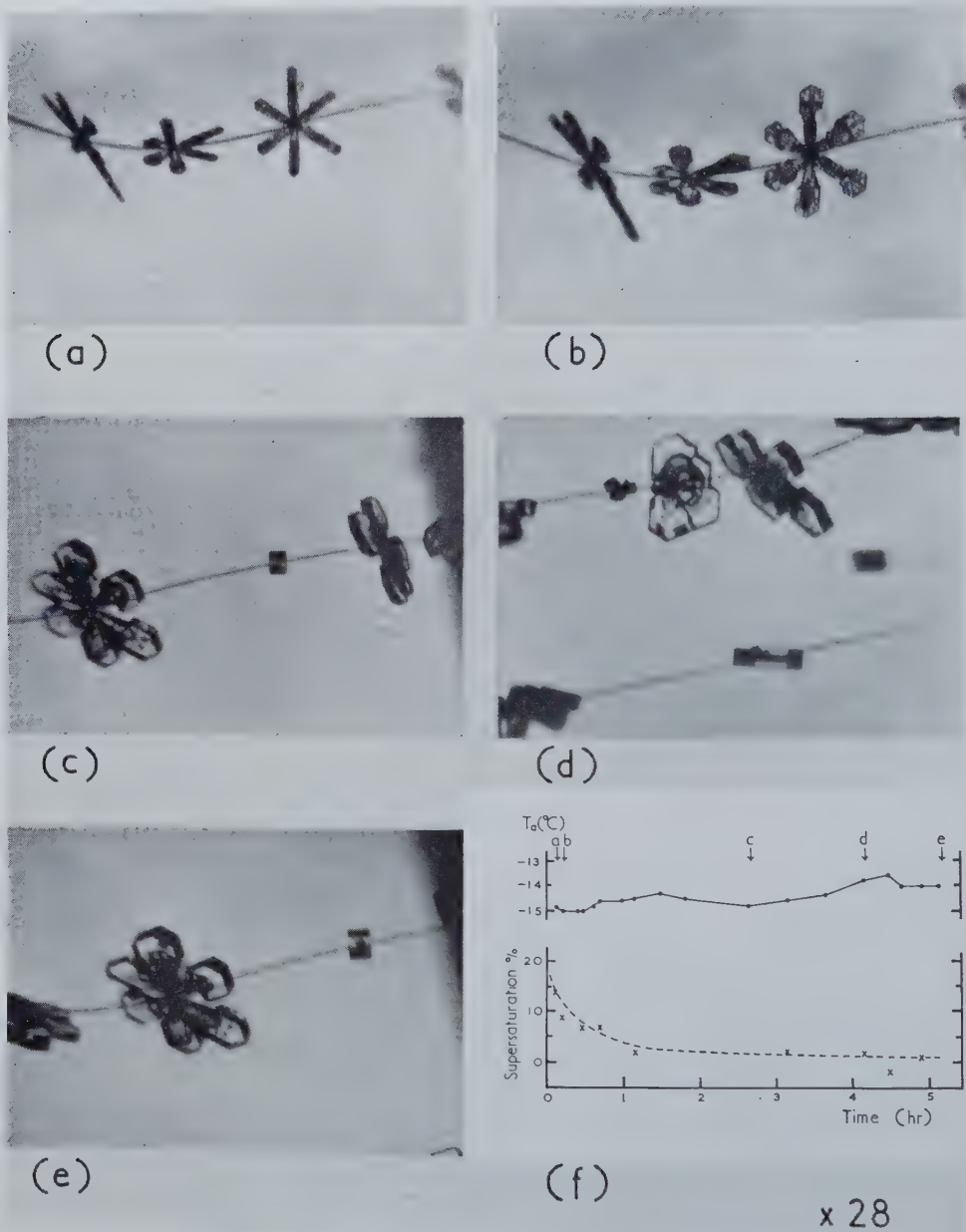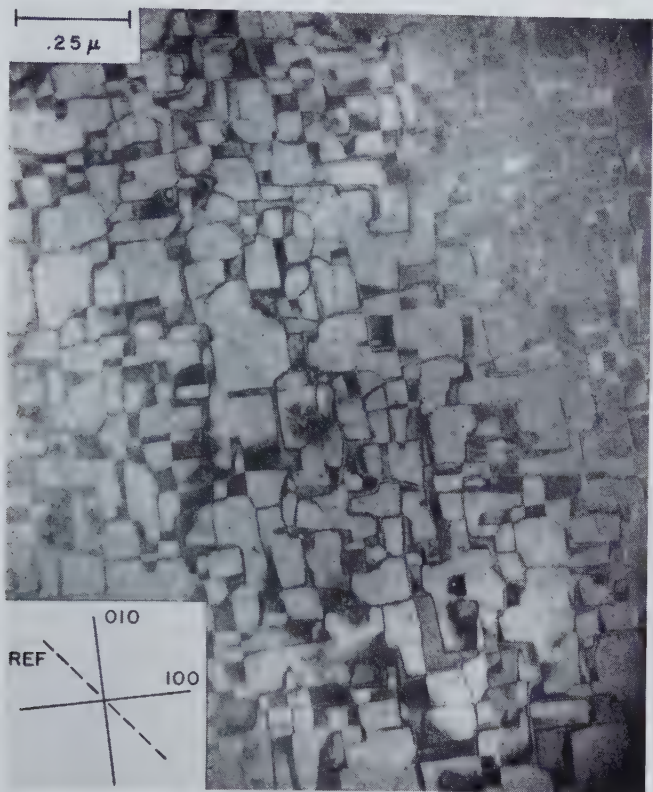
Fig. 2

Antiphase domain boundaries in partially ordered AuCu₃.
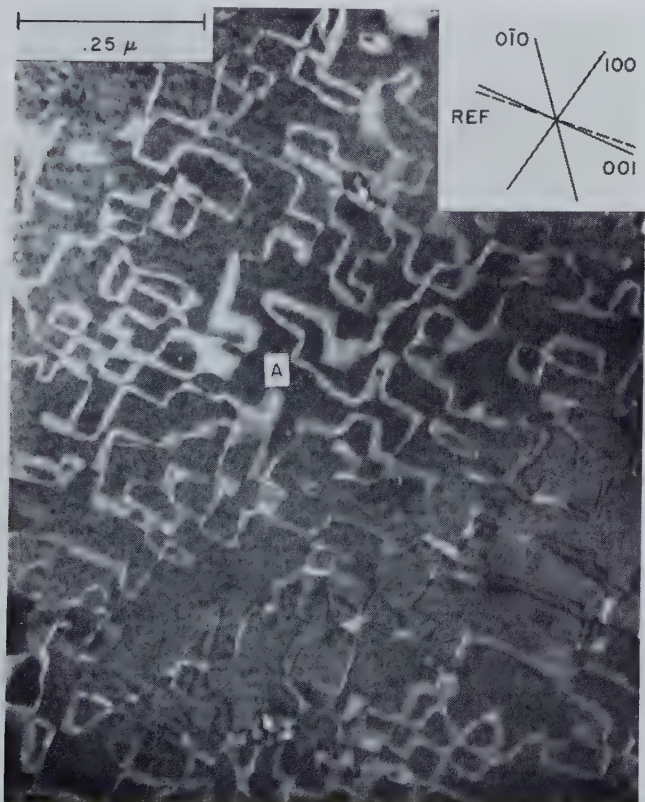


Fig. 3

Antiphase domain boundaries in fully ordered AuCu₃.   Normal to figure is
[121]

Fig. 5



(a)



(b)

(a) Extinction contour in partially ordered AuCu$_3$ arising from 110 superlattice reflection and therefore showing domain boundary contrast. (b) E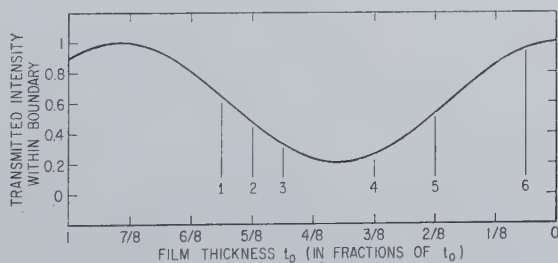xtinction contour in partially ordered AuCu$_3$ arising from 200 principal reflection and therefore showing no domain boundary contrast.
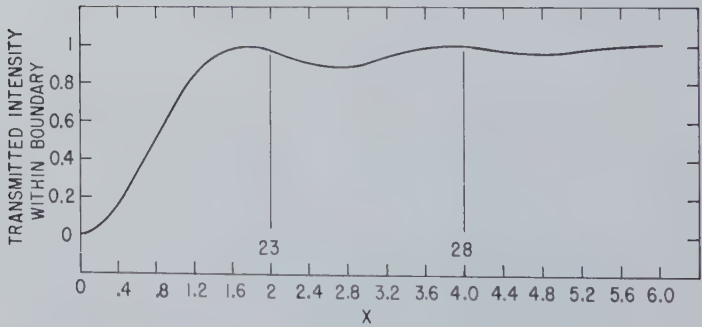
Fig. 8
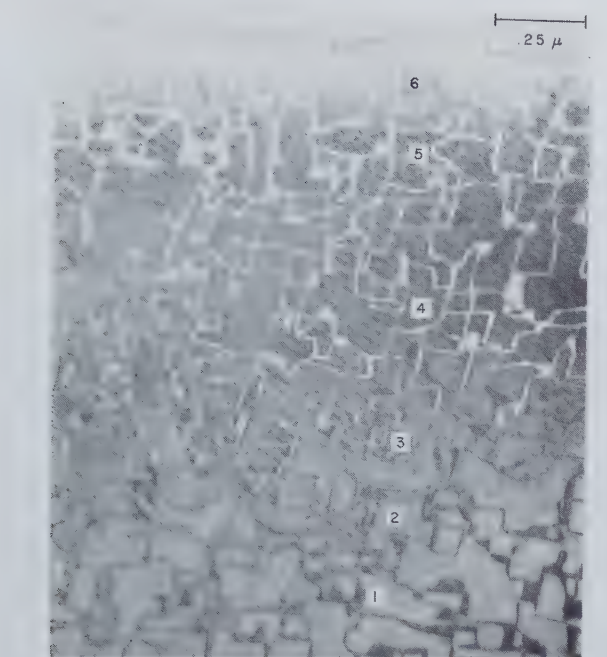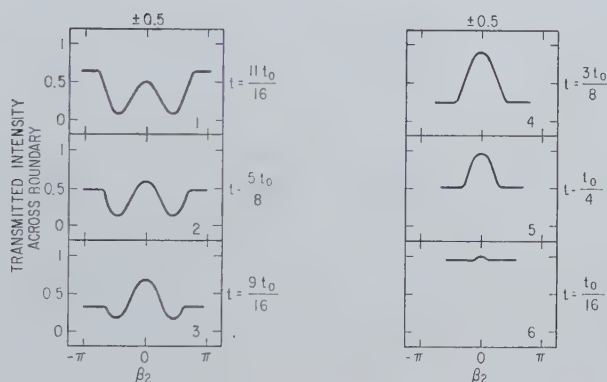


(a) Change in contrast of antiphase domain boundaries in partially ordered AuCu₃ near edge of foil. (b) Intensity profiles of domain boundaries corresponding to areas numbered in (a). (c) Variation of transmitted intensity within domain boundary as a function of foil thickness. Numbers under curve correspond to those shown in (a) and (b); x assumed to be ±0·5.

Fig. 9



(a)



(b)

(a) Pair of partially overlapping 110 and $\bar{1}$10 superlattice extinction contours in partially ordered AuCu$_3$. Domain boundaries show contrast changes due to variations in $x$. (b) Variation of transmitted intensity within domain boundary as a function of deviation of foil from exact Bragg angle. Numbers under curve correspond to those shown in fig. 9 (a) and fig. 7; $t$ assumed to be $t_0/2$.

Fig. 10
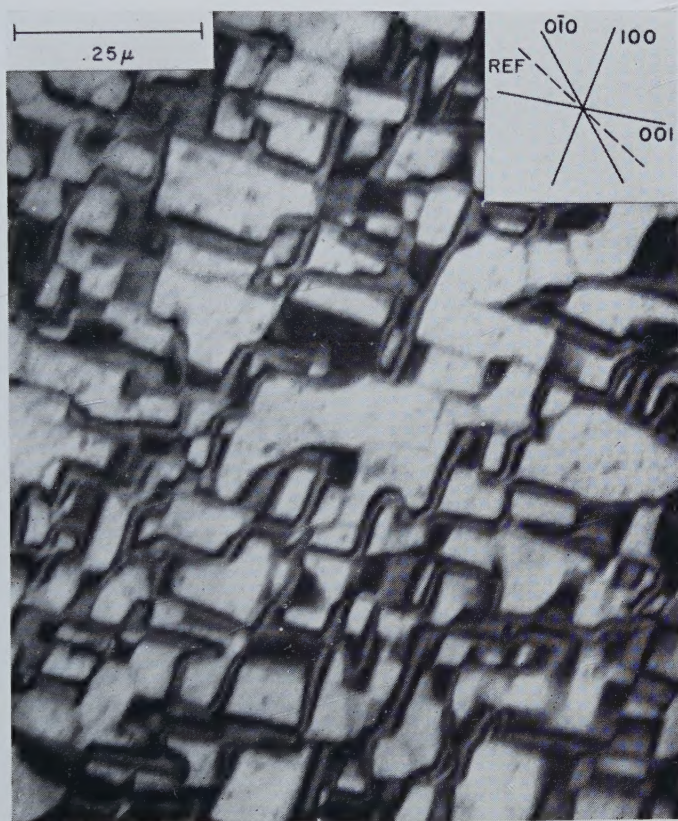


Antiphase domain boundaries in partially ordered AuCu$_3$ showing fringe contrast.
Normal to figure is [$\bar{1}2\bar{1}$].

Oriented overgrowth on chromium bromide platelets. Notice the networks of interfacial (epitaxial) dislocations.